DEPARTMENT OF PHYSICS, UNIVERSITY OF JYVÄSKYLÄ
RESEARCH REPORT No. 9/1998

IN-BEAM SPECTROSCOPY OF NEUTRON MIDSHELL Cd AND Sn NUCLEI UTILIZING CHANNEL SELECTION

BY
ANSSI SAVELIUS

Academic Dissertation
for the Degree of
Doctor of Philosophy

Jyväskylä, Finland
December 1998

URN:ISBN:978-951-39-9736-6
ISBN 978-951-39-9736-6 (PDF)
ISSN 0075-465X

Jyväskylän yliopisto, 2023

ISBN 951-39-0369-9
ISSN 0075-465X

DEPARTMENT OF PHYSICS, UNIVERSITY OF JYVÄSKYLÄ
RESEARCH REPORT No. 9/1998

IN-BEAM SPECTROSCOPY OF NEUTRON MIDSHELL Cd AND Sn NUCLEI UTILIZING CHANNEL SELECTION

BY
ANSSI SAVELIUS

Academic Dissertation
for the Degree of
Doctor of Philosophy

To be presented, by permission of the
Faculty of Mathematics and Natural Sciences
of the University of Jyväskylä,
for public examination in Auditorium FYS-1 of the
University of Jyväskylä on December 11, 1998,
at 12 o'clock noon

Jyväskylä, Finland
December 1998

Preface

It is my pleasure to express my gratitude to my supervisors Prof. Rauno Julin and Dr. Sakari Juutinen for their encouragement and invaluable guidance during the course of this work.

I gratefully acknowledge the staff of the Department of Physics for the inspiring and innovative atmosphere. Special thanks to the technical staff for their help and patience during the construction of the facilities and instrumentation carried out in the Accelerator Laboratory. Thanks go also to Dr. Pauli Heikkinen and the respective cyclotron operator team providing nights and days excellent ion beams for the experiments.

The γ-spectroscopy group has been great team to work with and to spend good times together. I am very grateful of the support of the all group members. The performed experiments have been very difficult and demanding, requiring the whole team to take part. Special thanks to Dr. Pete Jones, who innumerable times helped me to solve computer and data sorting problems.

The financial support from the University of Jyväskylä, the Graduate School of Particle and Nuclear Physics, the Academy of Finland and Ellen ja Artturi Nyyssösen säätiö are gratefully acknowledged.

Finally, I wish to thank my friends in Jyväskylä and elsewhere for numerous shared moments spend together, my family for their support and encouragement during the studies, and Kirsi for her patience and understanding.

Jyväskylä, December 1998

Anssi Savelius

Abstract

This thesis deals with the experimental methods and instrumentation employed in in-beam γ-ray spectroscopy. Before the experiments, the laboratory facilities were established including construction of the new beam line to the γ-cave and development of ancillary devices. Various Ge-detector arrays were installed and modified applicable for in-beam experiments utilizing weak reaction channels. A new charged particle detector array was constructed in conjunction with the DORIS Ge-detector array. Gamma-ray studies of binary products from ^{84}Kr + ^{116}Cd collisions have been carried out. New yrast states in ^{114}Cd and ^{116}Cd as well as an intruder band on top of the second excited 0^+ state in ^{116}Cd have been identified. These new data essentially add to the unique systematics of low-lying collective states in even-even Cd isotopes confirming the distinct behaviour of the intruder states. Excited states up to $I \approx 20$ in ^{115}Sn and ^{116}Sn, populated via the (^{18}O,αxn) reactions, have been studied using the DORIS Ge-detector array in conjunction with charged particle detectors. In both nuclei, spherical as well as regular, deformed level structures were found. The spherical states are interpreted to arise from pure neutron configurations, while the deformed, intruder bands obviously involve proton 2p-2h excitations across the $Z = 50$ shell gap.

Contents

1. Introduction 1

2. Production of neutron-midshell Z ≈ 50 nuclei 3

2.1 Compound-nucleus reactions 3

2.2 Binary Reactions 6

2.3 Experimental aspects 10

    2.3.1 Thin target and Doppler effects 10

    2.3.2 Thick or backed target 12

3. Experimental facility 15

3.1 Construction of the beam line 15

3.2 Gamma-ray detector arrays 18

    3.2.1 Compton-suppressed Ge detectors 18

    3.2.2 Designing of the γ-ray detector set-up 19

    3.2.3 TESSA3 array 21

    3.2.4 DORIS array 24

3.3 PIN-diode array for charged particle detection 26

    3.3.1 Charged particle detection with PIN diodes 26

    3.3.2 Design of the PIN-diode array 29

3.4 Electronics 35

    3.4.1 TESSA3 electronics 35

    3.4.2 DORIS electronics 40

3.5 Liquid nitrogen filling system 40

3.6 Data analysis 42

4. Band structures in ^{114}Cd and ^{116}Cd from heavy-ion collisions 45

4.1 Introduction 45
4.2 Experimental methods 46
4.3 Level scheme of ^{114}Cd and ^{116}Cd 50
4.4 Level systematics for even-mass Cd isotopes 53

5. Coexisting structures in ^{115}Sn and ^{116}Sn 57

5.1 Introduction 57
5.2 Experimental methods 58
5.3 Experimental results 59
    5.3.1 The level scheme of ^{116}Sn 59
    5.3.2 The level scheme of ^{115}Sn 65
5.4 Discussion 75
    5.4.1 Properties of the observed bands 75
        Configuration assignments and alignments 75
        Comparison with neighbouring nuclei 83
        Quenching of the intruder-to-yrast $4^+ \rightarrow 2^+$ transition 85
    5.4.2 Spherical states in ^{115}Sn and ^{116}Sn 88
        The Microscopic quasiparticle-phonon model calculations for ^{115}Sn . 88

6. Summary 93
References 95

Chapter 1

Introduction

The first beams for nuclear physics experiments from the accelerator facility at the Department of Physics of the University of Jyväskylä (JYFL) were delivered in 1993. Soon after these commissioning runs, a large variety of light and heavy-ion beams from the JYFL ECR-ion source were developed. Today the JYFL-K130 cyclotron with the ECR-ion source has turned out to be one of the best accelerator facilities in the world especially for nuclear spectroscopic studies.

The work presented in this thesis is an essential part of the efforts to initiate a large-scale in-beam gamma-ray spectroscopy project at JYFL. For this purpose new beam lines and experimental stations were constructed in 1994. One of the important initiatives was the transfer of γ-ray spectrometer facilities from the Daresbury Laboratory and the University of Liverpool to JYFL. These facilities comprised of the TESSA3 γ-ray array with 12 Compton suppressed Ge-detectors and a BGO-inner ball as well as associated electronics and data acquisition system. A new liquid-nitrogen filling system for the Ge detectors had to be constructed.

The primary aim of the present work was to utilize the available 12 Compton-suppressed Ge detectors in relatively simple experimental set-ups for in-beam γ-ray experiments where very weak reaction channels are used to populate the nucleus of interest. The studies were focused on neutron midshell Cd and Sn nuclei which cannot be populated via conventional heavy-ion fusion evaporation reactions involving neutron emission. In these midshell nuclei, excitations involving proton-intruder configurations are expected to reach their lowest energy.

The idea of employing binary reactions induced by heavy ions in a thick target was used to populate intermediate-spin states in stable ^{114}Cd and ^{116}Cd nuclei. A beam of ^{84}Kr was used to bombard a ^{116}Cd target and γ-rays from the binary products stopped in the thick target were detected with the TESSA3-array.

Descriptions of collective low-lying states of even-mass Cd nuclei near the neutron midshell have been based on the idea of mixing of deformed proton-intruder states and vibrational phonon states [He95]. The role of proton intruder configurations in the development of collectivity in the even-mass Cd nuclei is still an intriguing question [Jul94]. In the present work, the results obtained from the binary reactions for the midshell nucleus ^{114}Cd and the ^{116}Cd isotope shed new light on the role of the intruder structures and the $h^2_{11/2}$ neutrons in the development of collectivity in these nuclei.

Several earlier studies of collective structures up to high spin in Sn nuclei with N<64 have been performed [LaF95,Ga95,Se97,Ha88,Sch91]. Comprehensive studies of low-spin states in the midshell ^{116}Sn nucleus have been carried out [Ka79]. Due to the lack of available projectile-target pairs, there is no easy access to ^{116}Sn via conventional heavy-ion reactions. Therefore it is difficult to probe its high-spin states. In this work relatively high-spin states in ^{116}Sn and also in ^{115}Sn were identified by utilizing weak fusion channels involving α-particle and neutron evaporation. For resolving these weak reaction channels an array of PIN diodes was designed and constructed for the charged particle detection. For a more efficient detection of γ-rays, the close-geometry DORIS array consisting of 12 TESSA type Compton suppressed Ge-detectors was constructed. These new data reveal level schemes with irregular sequences of spherical states coexisting with band structures based on deformed intruder structures.

Although this work is monographic, part of the material has been reported in *JYFL Annual Reports 1993-96* and published in *Phys. Lett.* ***B 386*** *(1996)80-84* and in *Nucl. Phys.* ***A 637****(1998) 491-519*. A publication of similar studies of ^{111}Cd and ^{112}Cd isotopes is under preparation.

Chapter 2

Production of neutron-midshell $Z \approx 50$ nuclei

2.1 Compound-nucleus reactions

In probing the structure of medium-heavy and heavy nuclei, compound-nucleus reactions are most widely used, especially when nuclear spectroscopic methods are employed. In these reactions a wide range of nuclei on the neutron deficient side of the valley of stability can be populated. In heavy-ion induced compound-nucleus reactions (fusion evaporation reactions) product nuclei with a large amount of angular momentum and high excitation energy are produced. These fusion products are strongly focused to the forward direction enabling Doppler corrections in the γ-ray detection and consequently, a good energy resolution even for the γ-rays emitted from short-living high-spin states.

In the reactions leading to heavy nuclei ($Z>70$), fission is the dominant reaction channel. Recently it has been shown that recoil gating and recoil decay tagging (RDT) can be used to resolve γ-rays emitted by the heavy fusion products from those emitted in fission [Pa95, Hel96]. The heavy neutron-deficient fusion products are often α- or proton emitters rendering it possible to tag the γ-ray transitions of interest. Fusion residues are selected from fission fragments using a recoil separator such as the RITU gas filled recoil separator at JYFL [Le95].

Moving towards the very neutron deficient and light regime of the nuclide chart the probability of the charged-particle evaporation increases and starts to compete with otherwise dominating xn-channels. Several open charged-particle channels and xn-channels share the total cross-section, so that the conventional in-beam spectroscopic methods become inadequate. For the identification of neutron deficient and medium heavy nuclei with A = 40 - 100 produced in fusion evaporation reactions, efficient and high granularity charged-particle multidetector systems have been developed. These kind of particle detector arrays have been employed in conjunction with most of the in-beam Ge-detector arrays such as the Microball array [Sa96] with GAMMASPHERE and the Silicon Ball array [Kur92] with NORDBALL.

In the present work the ^{115}Sn and ^{116}Sn nuclei lying in the middle of the valley of stability were studied via compound nucleus reactions. Due to the lack of available projectile-target pairs these nuclei are difficult to produce in such reactions. Neutron evaporation strongly dominates leading to the neutron deficient residues. Only very weak charged particle evaporation channels offer access to more neutron-rich nuclei.

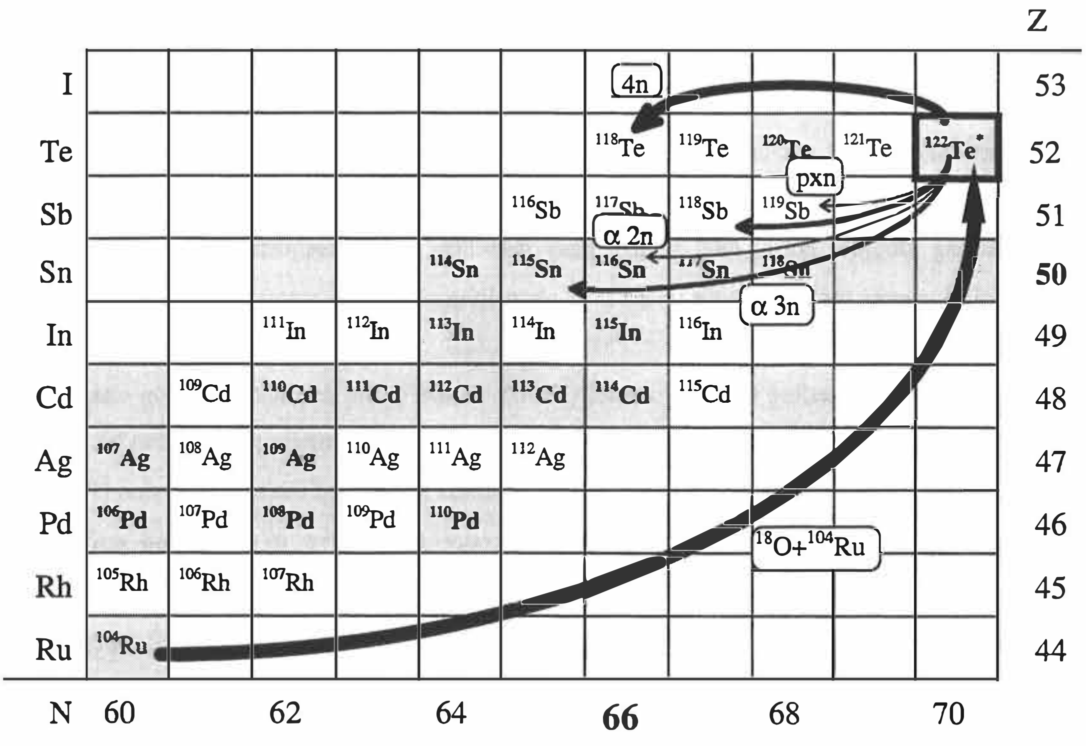

Figure 1. Main reaction channels in the ^{18}O + ^{104}Ru bombardment at $E(^{18}O)$= 65 MeV. The widths of the arrows are related to the reaction cross sections. The 4n evaporation channel leading to ^{118}Te is clearly the strongest, while the charged particle evaporation channels are less than about 10% of the total cross-section. Shaded boxes denote stable nuclei.

However, in contrast to the reactions leading to the very neutron-deficient medium-heavy nuclei only a few charged-particle channels are open in these reactions. This enables the use of a relatively simple and inexpensive experimental set-up for charged particle-detection as described in section 3.3. The reaction channels relevant to the study of the ^{115}Sn and ^{116}Sn nuclei in the present work are illustrated Fig. 1.

For inducing a compound-nucleus reaction the incident projectile energy must overcome the Coulomb barrier V_c , which can be calculated for the projectile - target nucleus pair with Z_1 and Z_2, respectively, by the expression,

$$V_c = \frac{1.44 \cdot Z_1 Z_2}{R_{\mathrm{int}}} \; MeVfm \qquad (1)$$

where R_{int} is the radius of the interaction defined as

$$R_{\mathrm{int}} = 1.16(A_1^{1/3} + A_2^{1/3} + 2)fm \qquad (2)$$

In the present work the ^{18}O + ^{104}Ru reactions were used to produce the ^{115}Sn and ^{116}Sn nuclei. These are the only compound-nucleus reactions leading to these residues which involve a relatively heavy projectile. For these reactions the Coulomb barrier $V_c = 47$ MeV. Based on the CASCADE calculations [Pü77], the beam energy of $E_{\mathrm{lab}}(^{18}\mathrm{O}) = 63$ MeV was obtained to optimize the production of the ^{116}Sn nucleus via the α2n-channel. However, in the present experiment the main goal was to maximise the angular momentum in the ^{116}Sn nucleus, which is achieved by increasing the beam energy by few MeV, resulting to the final beam energy of $E_{\mathrm{lab}}(^{18}\mathrm{O}) = 65$ MeV. As a consequence most of the cross-section in the αxn channels lead to the more neutron deficient ^{115}Sn nucleus, but leaving also sufficient yield for ^{116}Sn. The $(^{18}\mathrm{O},\alpha 3n)^{115}$Sn reaction represented about 5% and the

$(^{18}O,\alpha 2n)^{116}Sn$ reactions 1% of the yield for the most strongly populated nucleus ^{118}Te produced via the 4n channel.

The maximum angular momentum transferred to the system can be estimated by a semi-empirical formula

$$I_{\max} = 0.219 R_{\rm int}\left[\mu(E_{CM} - V_c\right]^{1/2} \qquad (3)$$

where μ is the reduced mass for the projectile and the target pair and V_c is the Coulomb barrier. This formula gives a maximum angular momentum of $27\hbar$ for the compound system ^{122}Te in the present experiment. The alpha and neutron evaporations both remove 2-$3\hbar$ of the angular momentum and so the calculated maximum spin of evaporation residue is close to the experimentally observed value of about $20\hbar$.

2.2 Binary reactions

The neutron-midshell ^{114}Cd and ^{116}Cd nuclei studied in the present work cannot be reached via the conventional compound-nucleus reactions, but can be produced via binary reactions. These reactions with heavy ion beams have been introduced as a tool in γ-ray spectroscopy to populate relatively high-spin states in neutron-rich nuclei near the β-stability line [Br90,Ju96]. Scattering of the binary-reaction products into a wide range of angles makes the correction of the Doppler effects difficult in in-beam γ-ray detection. To restore the γ-ray energy resolution position-sensitive particle detectors are needed to determine the scattering angles of the binary products. A different approach introduced by R. Broda et al. [Br90] and used in this work is to forgo particle detection and use a thick or backed target. Thus γ-rays emitted from low to intermediate spin states of stopped reaction products are observed without the Doppler effect.

The binary reactions include Coulomb excitation, relatively cold few-nucleon transfer reactions as well as deep-inelastic reactions with a massive exchange of nucleons. The Coulomb excitation has frequently been used as a spectroscopic tool, while the other types of binary reactions have been regarded as too weak for γ-ray spectroscopic purposes. They also suffer from the fact that the coincident γ-rays may originate from either one of the reaction partners. However, as it has been shown by Broda et al., despite the large background from other reaction channels the desired nucleus can be identified by $\gamma\gamma$ coincidence techniques from a good energy resolution and high statistics data set obtained with an array of Compton-suppressed Ge-detectors. In the present work the thick-target method was applied to study binary products from ^{84}Kr + ^{116}Cd collisions (Section 4). The favoured reaction process is dependent on the impact parameter b (Fig. 2), the energy of the projectile and the choice of the projectile-target pair. In collisions with an impact parameter $b > b_{gr}$ the nuclear interaction is negligible resulting in Rutherford scattering or Coulomb excitation. The grazing parameter b_{gr} is defined as the impact parameter of the trajectory leading to the grazing collisions where a considerable nuclear interaction between the projectile and the target can take place.

Deep-inelastic collisions can take place when the projectile trajectory has an impact parameter b smaller than the grazing impact parameter b_{gr} (Fig. 2). During the deep-inelastic collision the reaction partners penetrate the Coulomb barrier and under the influence of the attractive nuclear force nucleons are transferred between the target and projectile nuclei, which leads to excitations of the reaction partners. In heavy-ion collisions deep-inelastic processes with the projectile energies of 10-15% above the Coulomb barrier have proven to yield good spectroscopic results.

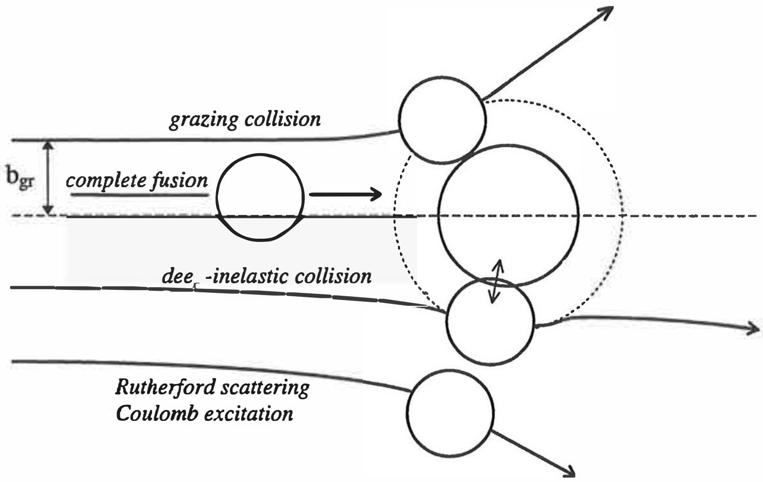

Figure 2. Deep-inelastic reactions involve substantial exchange of mass and charge resulting in target-like and projectile-like fragments. Deep-inelastic reactions can take place when the impact parameter $b \leq b_{gr}$. In Rutherford scattering no nuclear mass or charge is transferred.

The angular distribution of the deep-inelastic reaction products is forward-tending, indicating also that the reaction interaction time (10^{-21} to 10^{-22}s) is shorter than the nuclear-rotational period. The interaction time is long enough to transfer several nucleons between the target and the projectile nucleus and bring the reaction products to highly excited states. The angular momentum transferred to the reaction products in deep-inelastic reactions depends on the masses of the colliding nuclei and can reach value of about $30\hbar$ in very heavy nuclei (i.e. ref. [Co97]).

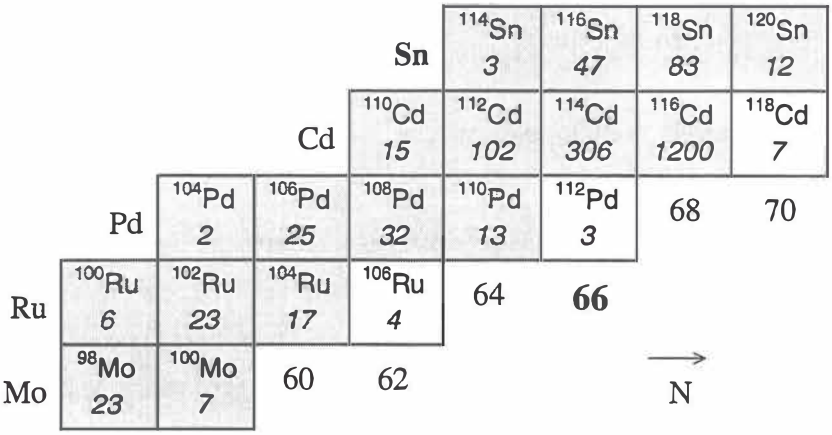

Figure 3. Production yields in arbitrary units for even-mass target-like products in ^{84}Kr + ^{116}Cd collisions. The yields are extracted from the coincidence data by setting the gate on $2^+ \rightarrow 0^+$ transitions. Shaded boxes denote stable nuclei.

The binary-reaction products have a tendency to equilibrate the average N/Z-ratio to that of the N/Z-ratio of the compound system. Therefore nuclei with N/Z ratio of the compound system are produced with appreciable intensity. The main production yield is concentrated in the target and projectile vicinity. In case of the ^{84}Kr + ^{116}Cd system transfer of neutrons from target to projectile and protons in both directions seems to occur as seen in Fig. 3. It should be noted that the excited binary reaction products undergo light particle evaporation, which can be shown by means of a γ-ray cross coincidence analysis [Br90]. In Fig. 3 the target nucleon is the most strongly populated reaction product due to the Coulomb excitation. The yield analysis for the odd nuclei is practically impossible due to the complex level schemes. Therefore only the even-even nuclei are presented in Fig. 3.

2.3 Experimental aspects

2.3.1 Thin target and Doppler effects

In in-beam γ-ray experiments Ge detectors view directly the target position, where the nuclear reaction takes place between the target and the projectile nuclei. In the fusion evaporation reactions the projectile energy is chosen to optimise the yield of the selected reaction channel. The projectile looses energy in the target material and therefore thin targets are used to minimize the production of nuclei via other channels or reaction mechanisms. By using a thin target the angular spread of the recoils is also minimized. On the other hand, in an in-beam γ-ray experiment the target should be thick enough to obtain a sufficient reaction rate. In practice, targets of 0.2 - 0.7 mg/cm^2 thickness are used in these experiments. The reaction rate in a thin target experiment can be increased by stacking several thin targets together so that they are separated by about 0.5mm from each other. In the present work v/c=1.3% for the Sn recoils from the ^{18}O + ^{104}Ru reactions, denoting that after about 0.1ps the recoils have left the thin target and most of the γ-rays of interest are emitted from the recoils flying in the vacuum. The recoils flying out from the target are strongly focused to the beam direction enabling the detection of narrow γ-ray lines also from the short lived states. Beams of relatively heavy ions are required to attain these conditions in fusion evaporation reactions.

Due to the Doppler effect the observed γ-ray energy can be denoted as

$$E_\gamma \approx E_o\left(1+\frac{v}{c}\cos\theta\right) \tag{4}$$

where v is the recoil velocity and θ is the γ-ray detection angle with respect to the scattered recoil i.e. in fusion evaporation reactions the detection angle with respect to the beam direction. When θ is known, the Doppler correction for obtaining the unshifted transition energy E_0 can be easily made. Due to the opening angle $\Delta\theta$ of the γ-ray detector, see Fig. 4, Doppler broadening of the photo peak in the γ-ray spectrum for a constant recoil velocity is observed as

$$\Delta E_\gamma = E_0 \frac{v}{c} \sin\theta \cdot \Delta\theta \tag{5}$$

For example, in the present work for the Ge-detector crystal with ∅ = 52mm at 15 cm from the target the opening angle $\Delta\theta = 16°$. Therefore for the γ-rays emitted from the Sn recoils with v/c=1.3 % and detected at $\theta = 37°$, the Doppler broadening $\Delta E = 2.2$ keV for $E_\gamma \approx 1$ MeV.

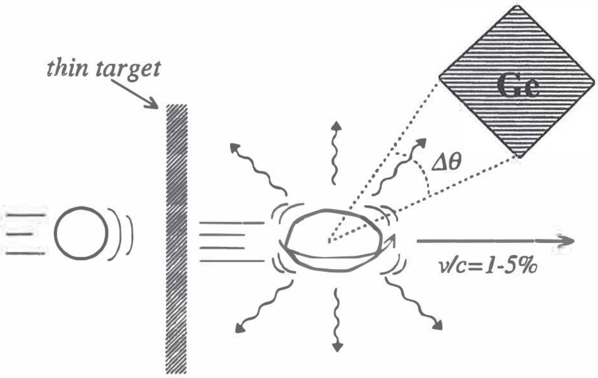

Figure 4. In a thin target experiment the fusion products fly in the direction of the beam whilst emitting γ-rays.

In binary-reaction experiments with thin targets the reaction products have a relatively wide angular distribution. To obtain a good γ-ray energy resolution in thin target experiments the reaction products must be detected with a position sensitive detector system to get θ for the Doppler corrections. In order to reach high detection efficiency rather complicated systems are needed.

2.3.2 Thick or backed target

The typical stopping time for reaction residues from heavy ion reactions in the target material is of the order of 1ps. The γ-decay from the excited states of the product nuclei having cumulative lifetimes longer than 1ps, takes place in the nuclei stopped in a thick target or target backing and no Doppler effects are observed. For example, in the present study of the Sn-isotopes produced via the ^{18}O + ^{104}Ru reactions in a backed target, sharp γ-ray lines from yrast states up to I ≈ 18$\hbar$ where observed without Doppler shift. Mainly due to increasing transition energies, the level lifetimes above this spin value become so short that the γ-rays are emitted from decelerating recoils and therefore severe Doppler broadening is observed.

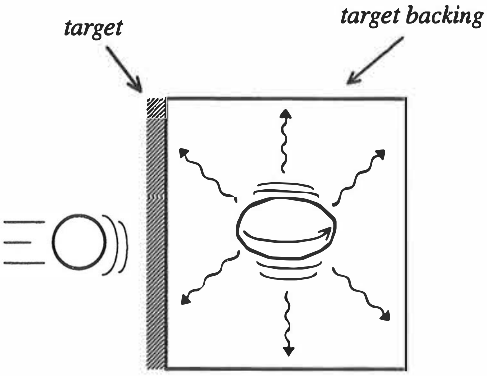

Figure 5. In the backed or thick target experiments the reaction products are stopped in ~1ps and therefore the γ-rays emitted from the states having cumulative lifetime longer than 1ps are emitted from nuclei in rest and detected without Doppler effects.

In a backed target the target material is evaporated on a backing thick enough to stop the recoils (Fig. 5). The atomic number of the backing material should be higher than that of the target, such that it has a higher Coulomb barrier and thus avoiding nuclear reactions in the backing. Gold is an often used backing material since it has a relatively high atomic number, it is easy to evaporate and it is a physically strong material.

When γ-rays from binary products are observed the beam energy is only about 10 - 15% above the Coulomb barrier. Therefore a thick target instead of a backed one can be used. Namely, the beam quickly looses its energy and below the Coulomb barrier no significant background from the other nuclear reaction yields.

Chapter 3

Experimental facility

3.1 Construction of the beam line

The new JYFL accelerator laboratory and the heavy ion K130 cyclotron with the large variety of ion beams has turned out to be outstanding facility for nuclear structure studies. The early aim of this work was to commence in-beam γ-ray spectroscopic projects at JYFL. The project started from the construction of the beam lines and ancillary equipment in the existing caves of the target hall. The construction work began from the main beam line and followed to the in-beam γ-ray spectroscopy cave and continued further to the other experimental areas. The construction work included the mounting and aligning of the ion-optical elements, diagnostics and beam tubes. Also the vacuum pumps and gauges were installed.

From the main beam line the ion beam is bent by the 90° double focusing dipole magnet to the beam line leading to the γ-cave (Fig. 6). To attain focusing effects in the horizontal and in the vertical direction the edges of the dipole are tilted to an angle of 27°. Due to the dispersive nature of the dipole magnet the energy distribution of the ion beam results in a spread in the beam focus after the dipole magnet. The dipole magnets at JYFL have a bending radius of 1.25m and the focusing distance of 2.6 m and therefore the value of dispersion $\frac{\Delta x}{\Delta p/p} = 4.26\, {}^{cm}\!/_{\%}$.

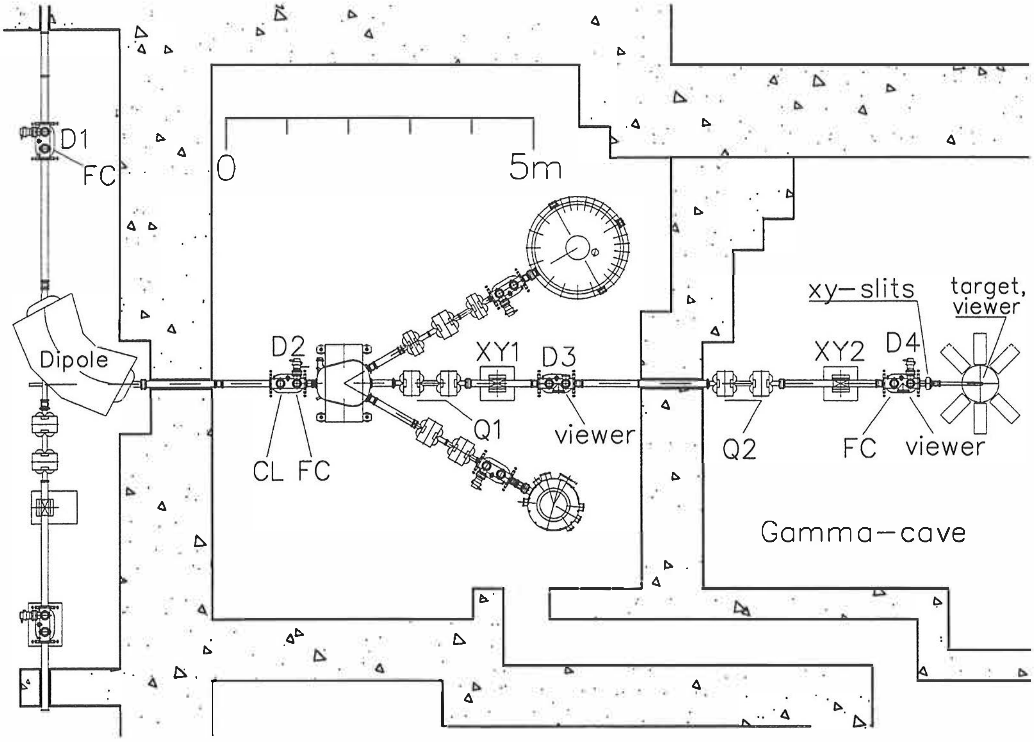

Figure 6. The experimental area of the in-beam γ-spectroscopy cave at the JYFL accelerator laboratory. Abbreviations for the beam line components D1..4, FC, CL, XY1..2, Q1..2 denote diagnostic box, Faraday cup, hole-collimator, XY-steering magnet, quadrupole magnet, respectively.

In the present work i.e. an ^{18}O beam of 65 MeV was employed. The energy resolution of the beam after the extraction from the cyclotron is typically $\Delta E/E \approx 0.5\%$. This energy spread gives rise to a maximum of ~11 mm broadening of the beam focus after the dipole magnet. By using, for example, Ø=5mm hole collimators the energy resolution can be improved by factor of 2. This energy accuracy is sufficient for in-beam spectroscopic purposes. Properties of the ion beam are monitored by the diagnostic boxes (D1-D4) which include beam current measurement by the faraday cups (FC), the hole collimators (CL) and beam viewing by the scintillation plates (viewer). To facilitate the tuning of the dipole magnet, the diagnostic boxes (D1,D2) are positioned to the image point and to the focal point of the analysing magnet.

To preserve the ion beam emittance, two quadrupole magnet sets (Q1,Q2) are mounted after the collimator and before the target position. Usually the first quadrupole magnet of the set is horizontally focusing and the second one vertically focusing element. In practice it is difficult to maintain the beam on the optical axis and therefore the XY-magnets (XY1,XY2) mounted after the quadrupole magnets are needed. The XY2-magnet is especially needed when the ion beam is steered through the target frame, typically of the size of 8×11 mm in the present work. The focus of the ion beam can be viewed by scintillation plates located in the diagnostic boxes D3, D4 and in the target position. The emittance of the ion beam can be improved by cutting it after the dipole magnet (D2) with the hole collimator and just before the target with the XY-slits. If only very low-intensity beam from the cyclotron is available, as for the ^{84}Kr beam used in the present work in the binary reaction experiment, the use of collimators has to be avoided resulting in a large beam spot at the target. In an easy case, like the ^{18}O beam used in the Sn work, the available beam intensity was so high that the collimation could be used and the beam spot at the target position was small, typically about 4mm in diameter. The XY-slits are used to avoid the possible beam halo hitting the aluminium target frame. However the background radiation produced in the slits can cause disturbingly high counting rates in the Ge detectors and in the BGO shields, especially when light ion beams are used. Usually the power supplies of the JYFL beam-line magnets are very stable such that no change in the quality of the beam spot is observed even in experiments of one week. The emittance of the cyclotron beam is much larger than for example that of an electrostatic accelerator. Therefore, a viewer plate (scintillator) in the target position must be used for obtaining a good beam spot. In the construction of the target chamber the design had to include a window for viewing this plate.

3.2 Gamma-ray detector arrays

3.2.1 Compton-suppressed Ge detectors

In the present work TESSA-type [No85] Compton-suppressed Ge detectors, shown in Fig. 7, were used in γ-ray detection. A closed end coaxial n-type Ge crystal ($\varnothing$ = 52 mm, d = 57 mm) with a thin outer dead layer is the main component of these detectors. The n-type Ge detectors are more resistant to the radiation damage induced by the fast neutrons than are the p-type Ge detectors. Moreover, neutron damaged n-type crystals can be successfully annealed in the home laboratory. The photo-peak efficiency of the TESSA-type Ge detector for 1.3 MeV γ-rays is about 25% in comparison with a 76 mm × 76 mm NaI(Tl) scintillation detector at a distance of 25 cm from the source. An energy resolution of these detectors for 1.3 MeV γ-rays was typically 2.0 - 2.8 keV in the measurement conditions.

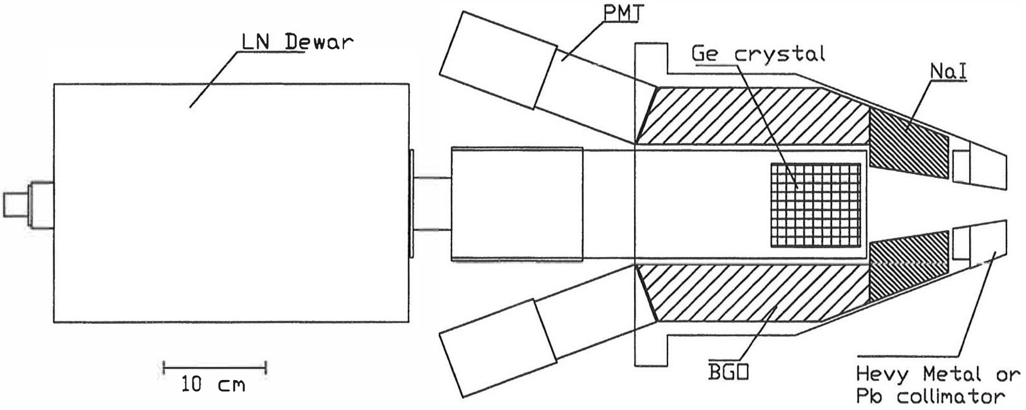

Figure 7. A schematic picture of the Compton suppressed Ge detector used in TESSA3 and DORIS arrays in the present work.

The anti-Compton shield surrounding the Ge crystal of the TESSA-detector unit is one of the first shields utilizing the new high efficiency BGO scintillator material (Fig. 7). It consists of eight optically separated BGO crystals each of them viewed by a photomultiplier tube. In the front part of the shield a NaI(Tl) scintillator crystal optically connected to the BGO crystals is used. The NaI(Tl) material with light output of ten times higher than that of BGO is used to catch the low energy (<300 keV) γ quanta backscattered from the Ge crystal. Heavy metal or lead collimators shaped for each detector geometry were used to prevent γ-rays from the target directly hitting the shield crystals. Typically a peak-to-total ratio (P/T) of 0.45 for the 1.3 MeV γ-rays was obtained for each TESSA units. This is an improvement of a factor of three for a P/T=0.15 for the 25% Ge detector without any shield.

3.2.2 Designing of the γ-ray detector set-up

For probing the structures of nuclear excited states, decay properties of these states are studied. In γ-ray spectroscopic studies, γ-ray cascades depopulating the excited states are observed by employing a γ-ray detector array in coincidence measurements and thereby constructing the energy-level scheme. The photo-peak coincidence efficiency of the array is $(\varepsilon_{tot})^n$, where ε_{tot} is the total photo-peak efficiency of the array and n is the γ-ray coincidence fold. Therefore the γ-ray detector array should be as efficient as possible. On the other hand, high energy resolution and spectrum quality should be maintained. In this work the nuclei studied were populated at intermediate spin states and de-excited by γ-ray cascades with a multiplicity of the order of ten. This relatively low multiplicity gives a possibility to achieve a good sensitivity by a moderate granularity array of twelve Ge detectors. The photo-peak efficiency of the array can be increased by mounting the Ge detectors close to the target.

The detector distance is limited by coincidence summing, where two or more γ-rays from the same cascade hit the same crystal (Fig. 8). To minimize the coincidence summing the Ge detector solid angle must be decreased by moving the detectors further away from target or by increasing the granularity. The probability of the coincidence summing in the case of double coincidence is given simply by

$$P \approx \Omega \cdot M \tag{6}$$

where Ω is the solid angle of the Ge-detector and M is the multiplicity. In the case of the TESSA-Ge detector with ∅=52 mm at the distance of 15 cm and for multiplicity M=10 the coincidence summing is $P = 0.75\% \times 10 = 7.5\%$. As described in section 2.3 the minimum distance of the γ-array detector from the target in the thin-target experiments is also limited by the Doppler broadening effects.

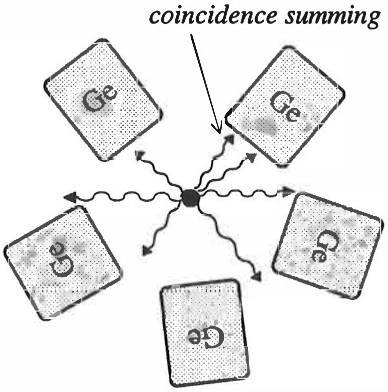

Figure 8. Close packing of the γ-ray detectors gives rise to coincidence summing.

3.2.3 TESSA3 array

The Total Energy Suppression Shield Array (TESSA3) [No86] was designed by Liverpool University and Daresbury Laboratory in England for studies of γ-ray cascades depopulating high-spin nuclear states (Fig. 9). In the present set-up the TESSA3 array consists of 12 TESSA-type Compton suppressed Ge detectors and a BGO-inner ball. The compact construction of the shields and BGO-inner ball combined with the Ge detectors having small liquid nitrogen dewars allows for an efficient and compact geometry. The TESSA3 array was used in the discovery of the superdeformation in ^{152}Dy [Tw86]. In this work the TESSA3 array was used to detect γ-rays from binary-reaction products in ^{84}Kr + ^{116}Cd collisions where the BGO multiplicity filter is a powerful tool for the selection of high spin γ-ray cascades out of low multiplicity cascades emitted from various binary products. The measured absolute photopeak efficiency for 1.33 MeV γ-rays of the TESSA3 array is about 0.3 % for twelve 25% Ge detectors. The detector angles with respect to the beam axis in polar angles are 35°, 90° and 145°.

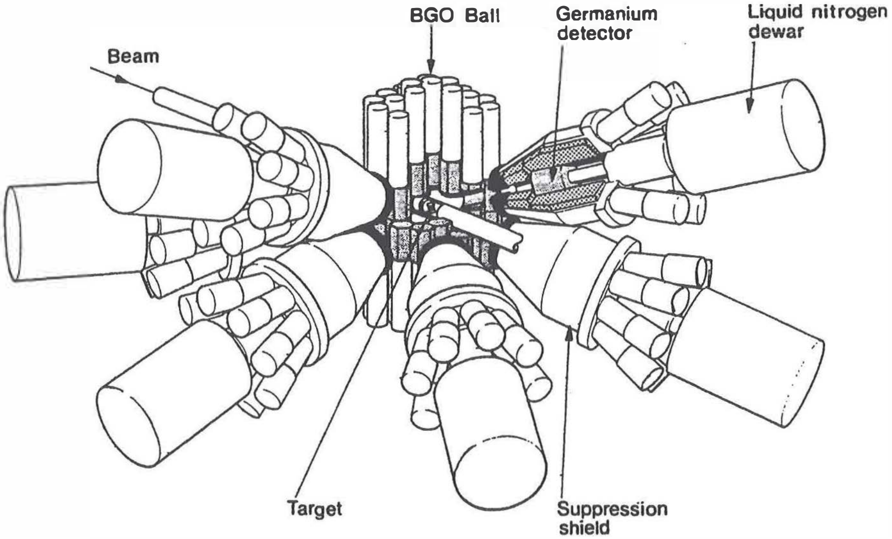

Figure 9. The TESSA3 array with the BGO-inner ball and Compton suppressed Ge-detectors.

The BGO-inner ball of TESSA3 is used to measure γ-ray multiplicity and sum energy. The individual BGO detectors have a hexaconical shape and they form a honeycomb geometry of three rings with 62 detectors, some of them paired to form a system of 50 individual detectors. When detecting γ-ray cascades from heavy-ion fusion products the sum-energy-multiplicity information can be used to select cascades from different evaporation channels. The BGO ball covers effectively the whole space between the target and the Ge-detectors leaving just an opening for the beam tube and Ge-detectors to view the target. The sum-energy is obtained by summing the energy signals and multiplicity by counting the number of crystals fired at the same time. In the present study of nuclei produced via binary reactions, the BGO-inner ball was used to discriminate between γ-rays from different types of binary reactions (Fig. 10). In the fold spectrum for the target isotope ^{116}Cd the strong peak at low multiplicity is due Coulomb excitation and the higher multiplicity tail of the spectrum due to transfer reactions. The more neutron deficient ^{112,114}Cd isotopes are produced by two and four neutron transfer and the average γ-ray fold is larger than in the target nucleus. Coulomb excitation is still present due to the target impurities.

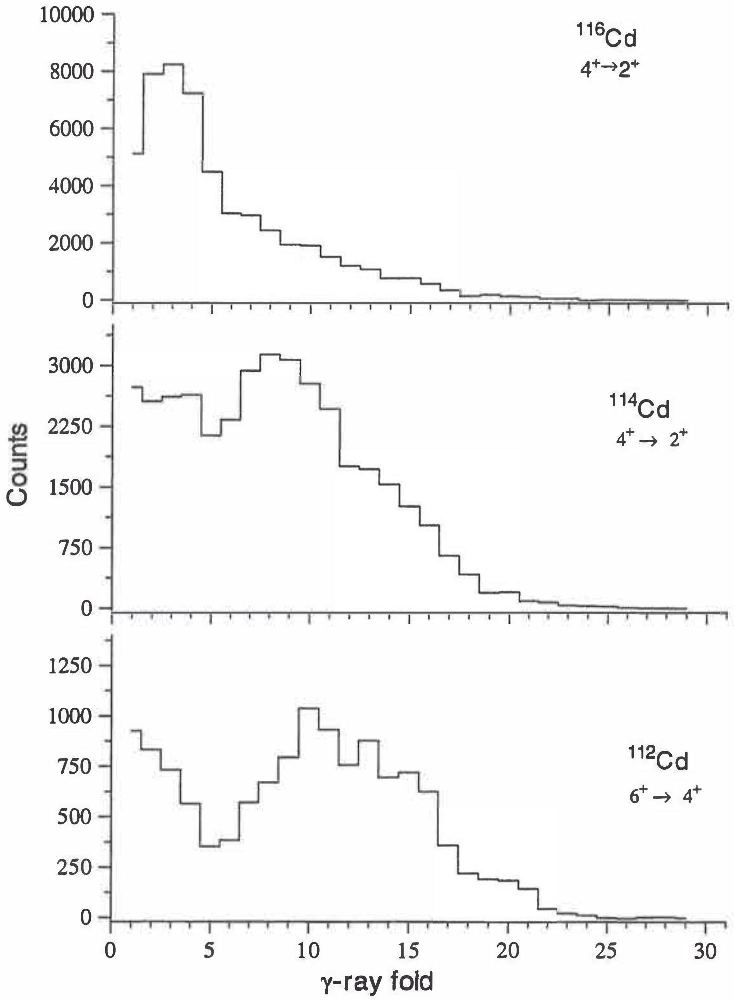

Figure 10. Gamma-ray fold distribution observed with TESSA3 BGO-inner ball from the bombardment of a ^{116}Cd target with 370 MeV ^{84}Kr ions. The distributions are obtained by gating with γ-rays from the $4^+ \rightarrow 2^+$ transitions in ^{116}Cd and ^{114}Cd and the $6^+ \rightarrow 4^+$ transitions in ^{112}Cd, detected by the Ge detectors.

3.2.4 DORIS array

In the TESSA3 frame the BGO-inner ball limits the Ge-detector-target distance to 23 cm. The multiplicity information from the BGO-inner ball is not that important when a charged particle detector system is used for channel selection. The use of a small charged particle detector array without the BGO-inner ball allows the Ge detectors to be brought closer to the target. In the present work a compact array, DORIS, was constructed using the TESSA-type Compton-suppressed Ge detectors (Fig. 11).

The dodecahedron geometry consisting of twelve pentagons, used in the DORIS (modified MiniNordball frame) array set-up, is the most compact geometry for twelve Compton suppressed Ge detectors. In the array the minimum distance from the Ge crystals to the target is 15 cm. As discussed in section 3.2.2, in the present studies the moderate multiplicity (~10) ensures that the coincidence summing is on a reasonable level. Also the Doppler broadening of the γ-lines from low velocity Sn recoils in the thin-target ^{18}O + ^{104}Ru experiment was not too serious (Section 2.3.1). The limiting factor to bring the Ge detectors even closer to the target are the size of the beam tube and the collimators covering the anti-Compton shield scintillators. New lead collimators were constructed for the DORIS array set-up. The collimator holes were made smaller and the extreme angle pieces were machined to a special shape to give space for the beam tube. Regardless of the new design of the collimators the three most forward and backward detectors had to be moved to 16.5 cm. The inner diameter of the beam tube is 34 mm, which is practically the minimum for the target and beam viewer construction inside the tube. The beam that goes through the target was dumped on a tantalum plate about half a meter downstream from the target (Fig. 11) to ensure that the Ge detectors count rate due to reactions in the beam dump was low enough. The absolute photopeak efficiency of 0.8% for the DORIS array was measured for the 1.33 MeV γ-rays, which is about 2.5 times the TESSA efficiency. The DORIS array detectors are mounted to four rings in polar angles at 37°, 78°, 102°, 143°, which enables extraction of the angular distribution ratios to resolve the multipolarity of the photons.

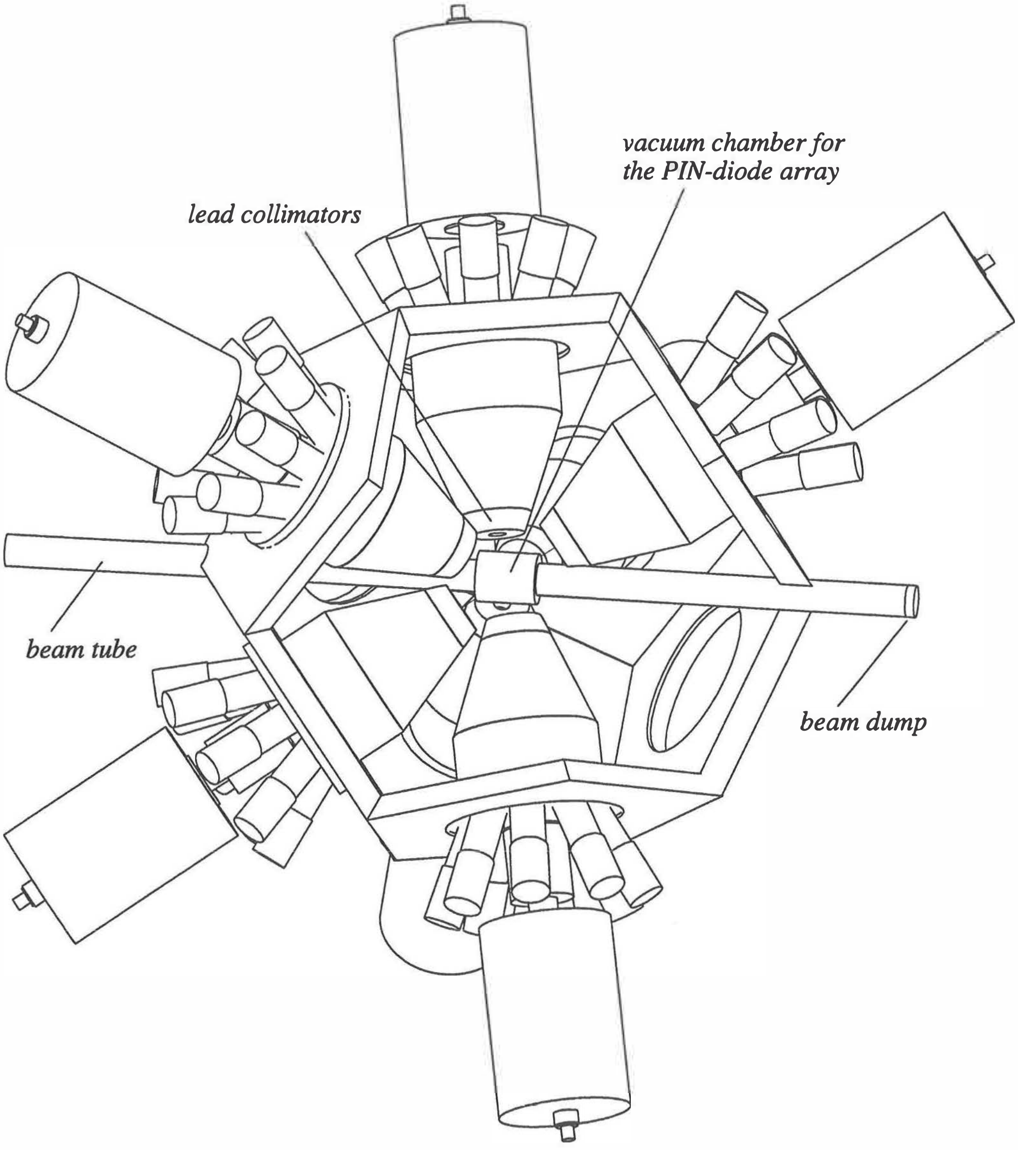

Figure 11. The DORIS array with Compton suppressed Ge detectors. The PIN-diode array and target is mounted to the centre of the array.

3.3 PIN-diode array for charged particle detection

In the present work the ^{115}Sn and ^{116}Sn nuclei were studied by utilizing weak (αxn) channels of ^{18}O + ^{104}Ru reactions. The detection of charged particles is needed to assign γ-rays to a weak reaction channel as well as to clean the γ-ray spectrum from undesired reaction channels as discussed in section 2.1. An array of 12 Si PIN-diode detectors was constructed to be used in conjunction with the DORIS array. In this case the compound nucleus (^{122}Te) lies close to the β-stability line leading to a low multiplicity evaporation of protons and α-particles rendering it possible to use a low granularity PIN-diode array. However, some kind of particle identification is needed to achieve a selection between proton and α-particle evaporation channels. The design and construction of the PIN-diode array is discussed in the sections below.

3.3.1 Charged particle detection with PIN diodes

Silicon is in many ways an ideal material for light charged particle detection. It has high density and therefore very high intrinsic detection efficiency, practically all implanted charged particles are detected. An advantage is also that Si-detectors can be operated at room temperature and still a high energy resolution is obtained in charged-particle detection. In Si-detectors the effective detection volume is created by applying a reversed bias voltage over the pn-junction. The most popular silicon detector for charged particles has been the surface barrier detector, where the pn-junction is formed between a gold layer and the silicon crystal. A disadvantage of a surface barrier detector is the relatively large frame construction, making it difficult to construct close-geometry arrays. The development of industrial semiconductor lithography has enabled the beneficial mass production of so called PIN diodes with a large detection area, see Fig. 12. PIN diodes, originally used to replace the photomultipliers in the detection of light from scintillation crystals, are now applied to charged particle detection. An advantage of the PIN diodes is the low-price and the small frame construction, which makes it possible to design close packed charged particle detector arrays. The signal read-out from the PIN diodes can be arranged simply with thin wires to feed-through pins of the vacuum chamber. The preamplifiers can be located relatively far away from the limited space of the spectrometer centre without affecting seriously the energy resolution.

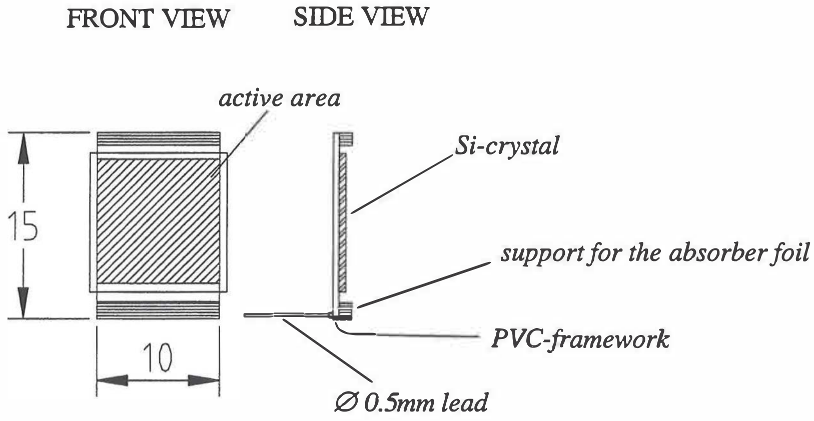

Figure 12. The Si-PIN diode detector used in the array of the present work.

In the PIN diodes used, the p- and n-junction materials are formed on the front and reverse side of the bulk high resistivity intrinsic silicon. This increases the depletion volume, the active region of the detector for incident radiation. The detector is normally biased so that the range of the charged particle of interest is shorter than the sensitive depletion thickness of the detector. In the PIN diodes this thickness is limited to 500 μm which is the range of about 8 MeV protons and 30 MeV α-particles. In the present experiments the mean energy for the evaporated α-particles and protons was 15 MeV and 8 MeV, respectively. Before reaching the detector, α-particles and protons had to penetrate tantalum absorbers (described later) losing their energy by ~5 MeV and ~1 MeV, respectively. Originally about 300μm thick PIN diodes were employed in the present work. The main problem when using the PIN diodes as charged-particle detectors in high counting rate in-beam experiments is the radiation damage of the p-n junction. This can be seen as an increasing leakage current and deterioration of the energy resolution. In this work the energy resolution does not play an important role in the detection of the evaporated charged particles. However, when the leakage current increases, the effective bias voltage over the detector decreases and the active depletion region becomes thinner. Therefore in spite of increasing the bias voltage, the detector starts to act as a ΔE detector as was the case in the present work in the proton detection. A typical energy resolution of an unused PIN diode in the present work was FWHM $\approx$ 20 keV for 5.5 MeV α-particles.

3.3.2 Design of the PIN-diode array

An array of 12 standard, low price 10×10 mm PIN diodes (Fig. 12) for the detection of evaporated α-particles and protons was constructed in the present work. To avoid absorption and especially scattering of γ-rays before entering the Ge crystals, PVC-plastic as a material for the detector framework and aluminium for the vacuum chamber were used as shown in Fig. 13.

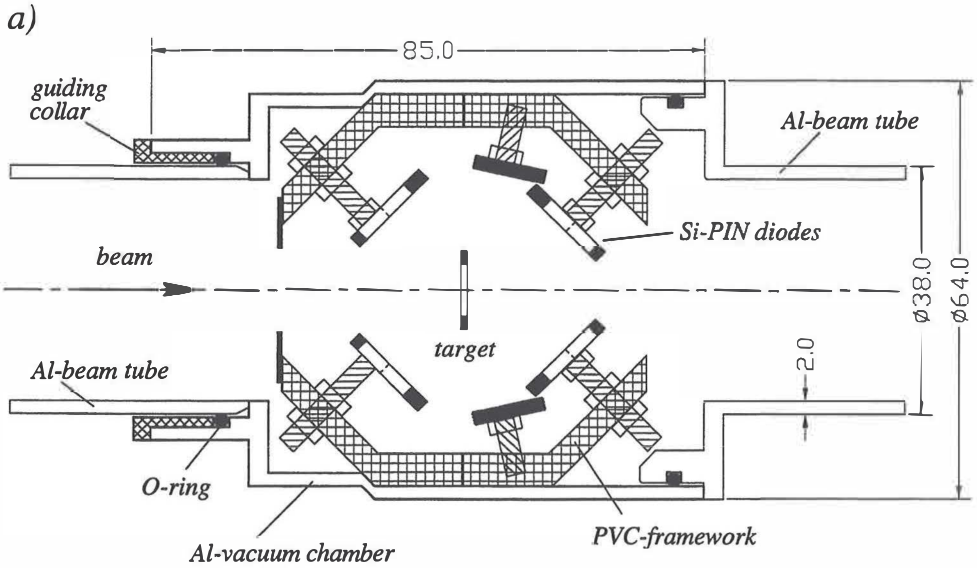

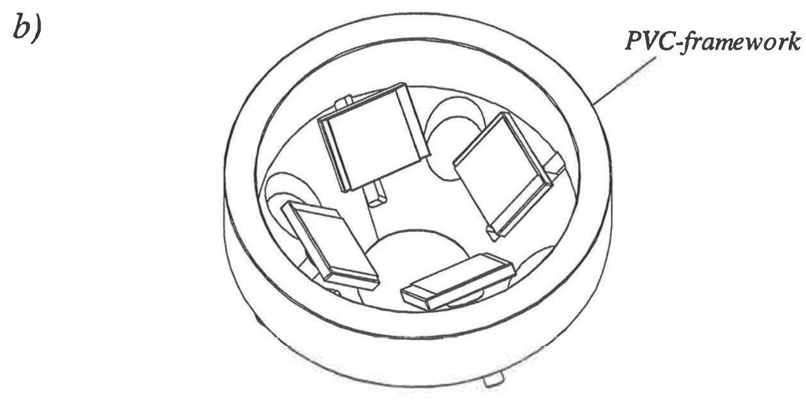

Figure 13. *a) Cross-section of the PIN-diode array and the vacuum chamber*
b) Backward hemisphere of the PIN-diode array.

The set-up consists of three rings of 4 PIN diodes at detection angles of 45°, 75° and 135° with respect to the beam. A coverage of about 30% of 4π solid angle was obtained with this geometry.

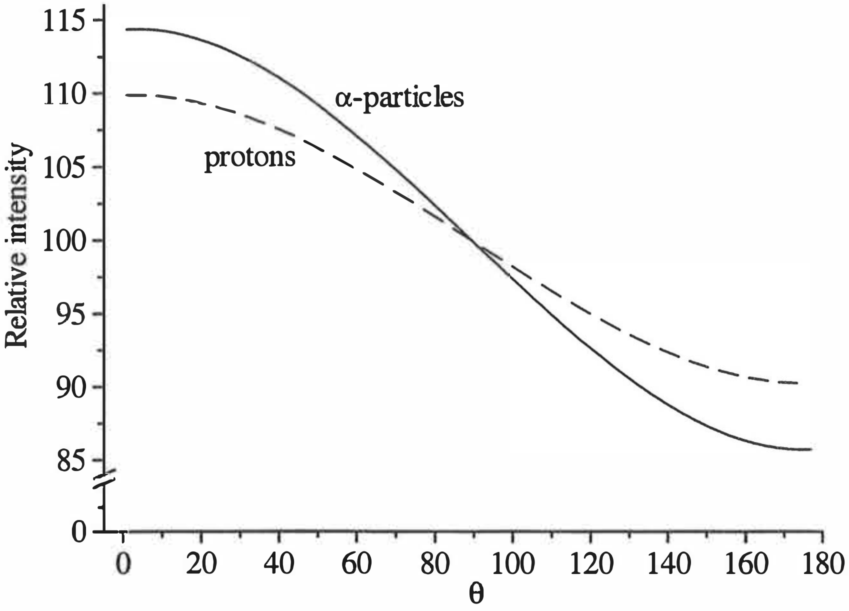

Figure 14. Emission angle of charged particles with respect to the beam axis in the ^{104}*Ru(*^{18}*O,αpxn) reactions at E(*^{18}*O) = 65 MeV.*

A result from a simple calculation for the angular distribution of the α-particles and protons from the ^{122}Te compound formed in the fusion of ^{18}O and ^{104}Ru, assuming an isotropic evaporation of charged particles, is shown in Fig. 14. Due to the velocity of the compound nucleus in the laboratory frame their angular distribution becomes somewhat forward peaked. Differences between the intensities observed at θ = 45° and θ = 135° is of the order of 10%. The anisotropy in the α-particle evaporation is obviously slightly higher than in the proton evaporation. In the present set-up it was possible to use two forward angle rings of 4 PIN-detectors; so that there was still enough space for the beam and no shadowing effect due to the target frame (Fig. 13).

Low energy δ-electrons and elastically scattered beam particles from the target material cause major problems in in-beam charged-particle detection. In the present work tantalum absorbers were mounted on the front of the PIN-diode faces to stop δ-electrons and scattered ^{18}O ions. The thickness of the absorber should be optimised so that the beam like particles are stopped and the evaporated charged particles are allowed to penetrate into the PIN detector. The thickness of the absorbers were chosen on the basis of the ion ranges in tantalum. Range-curves for α-particles, protons and ^{18}O-ions in tantalum are shown in Fig. 15. The energy of the ^{18}O-ions varies as a function of the scattering angle, shown in Fig. 16. Therefore different absorber thicknesses were used for the forward angle (20 μm or 33.2 mg/cm^2) and backward angle (15 μm or 25 mg/cm^2) detectors. Major part of the α-particles evaporated from the compound nucleus have energies between 10 and 20 MeV and the protons around 5 to 10 MeV.

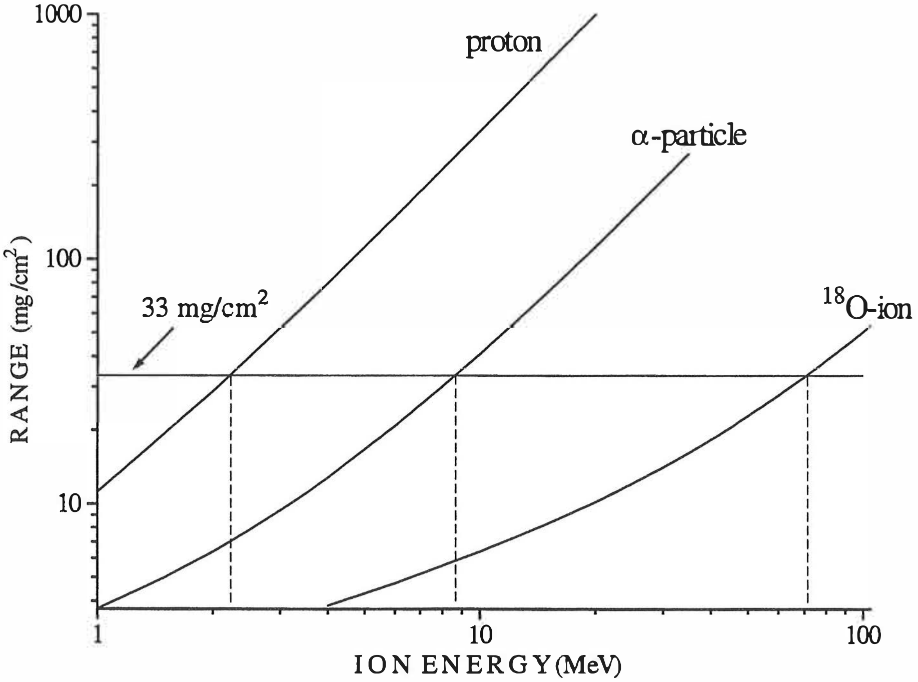

Figure 15. Ranges of protons, α *-particles and* ^{18}O *ions in tantalum. The dashed line refer to the maximum energies of the ions stopped in a* $33 mg/cm^2$ *thick tantalum absorber.*

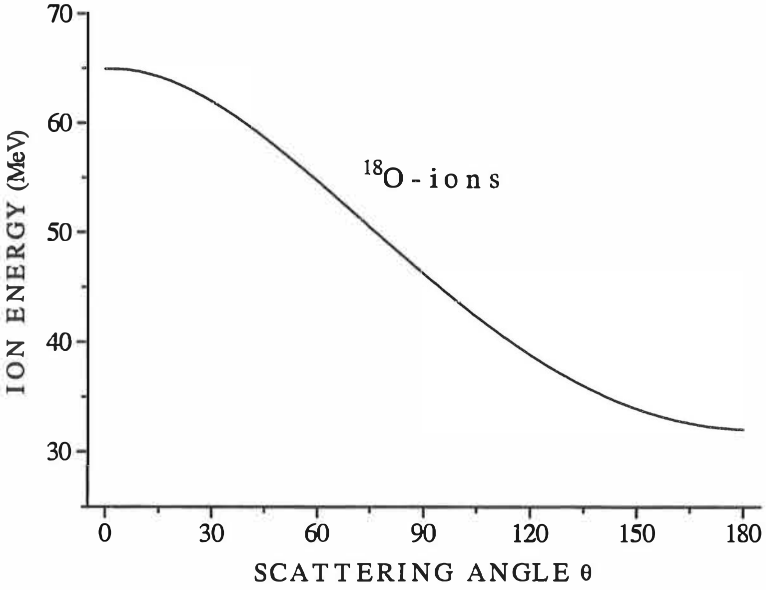

Figure 16. Energy of the ^{18}O *ions elastically scattered from the target. The primary energy of the* ^{18}O *beam is 65 MeV.*

Typical charged-particle spectra observed by the PIN diodes from the ^{18}O + ^{104}Ru reactions at 65 MeV are shown in Fig. 17. In the detectors placed at forward angles, the proton peak situated at lower energies is well separated from the broad high-energy bump corresponding to α-particles. When increasing the detector angle the alpha peak moves towards the proton peak and finally overlaps it at backward angles. Due to the reaction kinematics the energy of the particles in laboratory coordinates depends on their emission angle. The average energy of protons and α-particles emitted from the ^{122}Te compound nuclei in the present work are about 8 MeV and 15 MeV, respectively, in the rest frame. In the laboratory frame these energies are 9.2 MeV and 16.1 MeV at 45° and 6.9 MeV and 12.2 MeV at 135°. For forward angles the kinematical effect increases the peak separation, which is important in obtaining a clean channel selection. The energy loss (dE/dX) in the tantalum absorber is greater for α-particles than for protons making the energy difference even smaller in backward angles. The double nature of proton peak at angles of 75° and 135° is due to fact that the detector is partly acting as a ΔE detector. Multiple hits in the same detector also disturbs the clean channel selection. Events where $\alpha+\alpha$, p+p or α+p hit the same detector at the same time are incremented to high energy part of the spectra. This multiple hit probability increases with decreasing granularity.

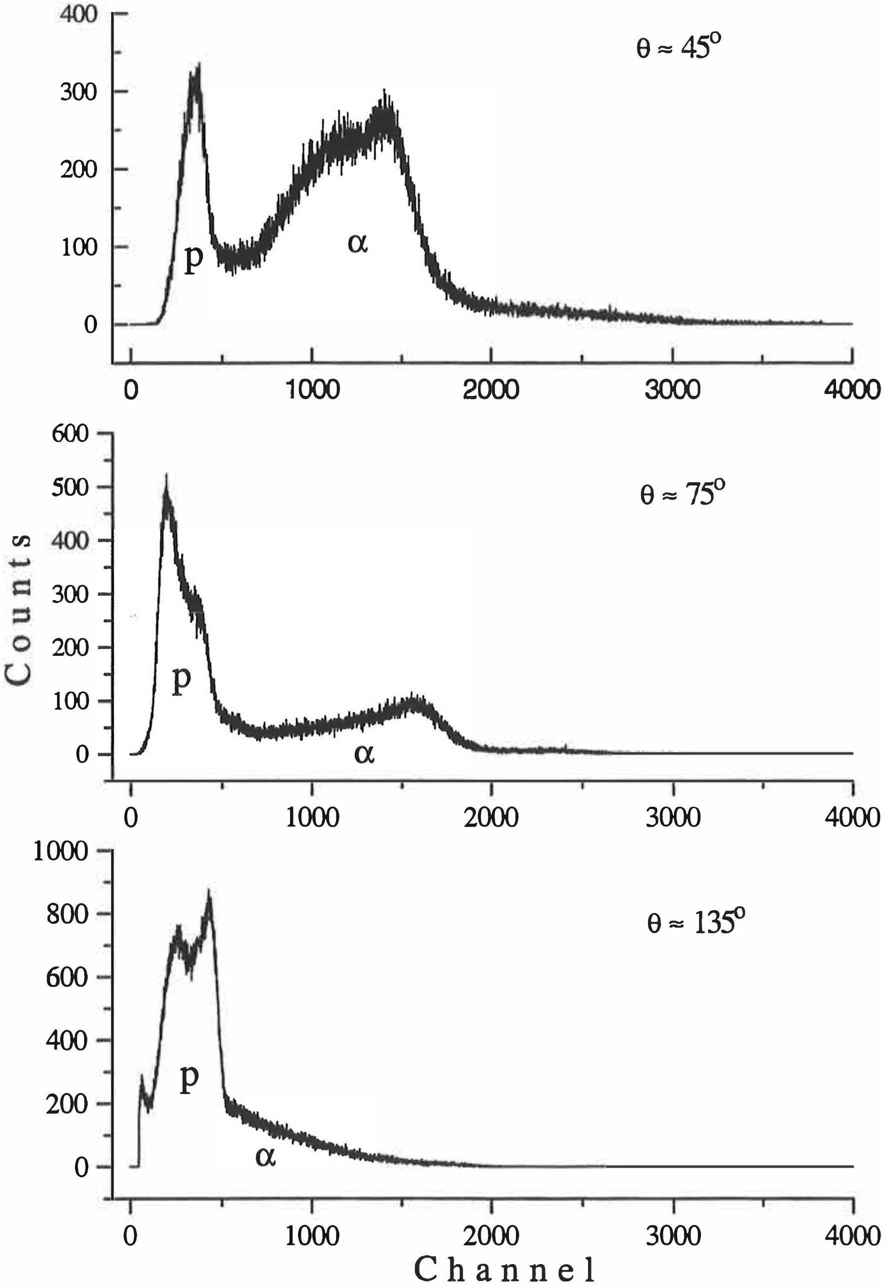

Figure 17. Spectra of evaporated protons and α-particles from the ^{18}O + ^{104}Ru reactions detected with PIN-diode detector at angles of 45°, 75° and 135° with respect to the beam axis.

3.4 Electronics

3.4.1 TESSA3 electronics

Standard NIM and CAMAC electronics was used to process the signals from the detectors. The aim of a coincidence experiment with a modern γ-ray array is to collect events where γ-rays are detected by different detectors within a few tens of nanoseconds. In order to generate an event the detector signals are processed to an applicable form using NIM electronics. The energy signal from the Ge detector preamplifier is amplified in a spectroscopic linear amplifier (AMP) and then digitalized in an analogue-to-digital converter (ADC) before fed into the data acquisition system. The main purpose of the linear amplifier is to preserve the energy information i.e. the amplitude of the preamplifier pulse. For the timing information the preamplifier pulse is first amplified and shaped in a fast timing-filter amplifier (TFA) so that the rise time of the preamplifier signal is maintained. The analogue timing signal from the TFA is fed to a constant fraction discriminator (CFD) for obtaining a logic timing pulse ready for the coincidence unit (COIN) input. The TFA and CFD units are tuned in such a way that so called amplitude and rise-time compensation in the timing of the Ge detector pulses is obtained as best as possible. The outputs from the CFDs are vetoed by the CFD signal from the corresponding BGO shields in order to reject the γ-rays (*a* in Fig. 18) scattered from the Ge crystal to the BGO detector. The veto signal has to be present for the whole duration of the Ge signal ($w \approx 50$ns) and therefore the width of the veto gate is set as wide as 170ns. In the first multiplicity logic unit (MLU) after the Compton suppression the fast $\gamma\gamma$-coincidence condition is set. The signals are delivered from the MLU to the $\gamma\gamma$-BGO coincidence unit (*c* in Fig. 18) and to the $\gamma\gamma$-TAC unit.

The pile-up rejection system avoids uncorrelated pulses which arrive too close to each other resulting in distortion of the energy signal. The pile-up rejection is carried out in two separate steps. The busy signal (w≈20μs) from the linear amplifier, generated at the onset of each linear input pulse, is used to reject the γ-event out of two pile-up events which is about 100ns→20μs after the γ-ray (*a* in Fig. 18). In order to discard the other γ-event the timing cross-over pick-off (TCO) method using the bipolar signal from the linear amplifier is employed to reject the events ranging in time about 0ns→10μs , indicated as *b* in Fig. 18.

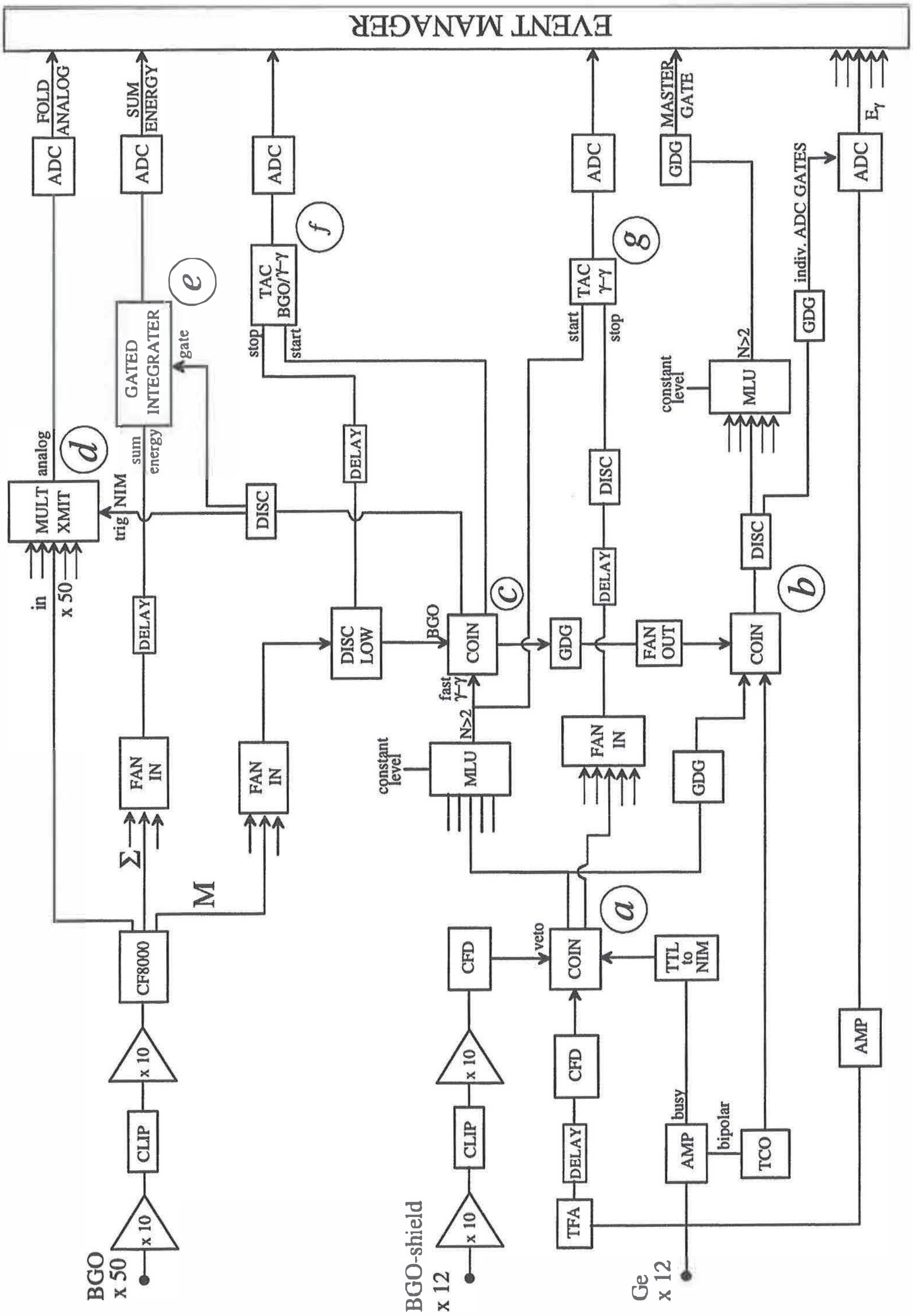

Figure 18. A block diagram of the electronics used in TESSA3 set-up.

The signals from the Ge detectors that were not rejected neither in Compton suppression nor in the pile-up rejection produce the signals for the master gate and for the individual ADC gates. An additional condition for the master gate was that the clean Ge signals must be in coincidence with the signal from the BGO-inner ball (*c* in Fig. 18).

A common time spectrum for all twelve Ge detectors were generated in TAC-units indicated as *g* in Fig. 18. A γγ-event was used to start the clock and the individual detectors to stop the clock. A γγ/BGO-inner ball time spectrum was recorded where the clock is started by a BGO-γγ coincidence event and stopped by a BGO-inner ball event (*f* in Fig. 18). The number of the BGO-inner ball detectors that fire in coincidence, also termed as fold, is obtained by the multiplicity logic unit (MULT XMIT) shown in part *d* in Fig. 18. The sum energy is created in the linear FAN IN-units by summing the individual analogue BGO-inner ball energy signals. Only the fold and sum energy signals in coincidence with the γγ-events are accepted. Sum energy information is produced in the gated integrator, indicated as *e* in Fig. 18.

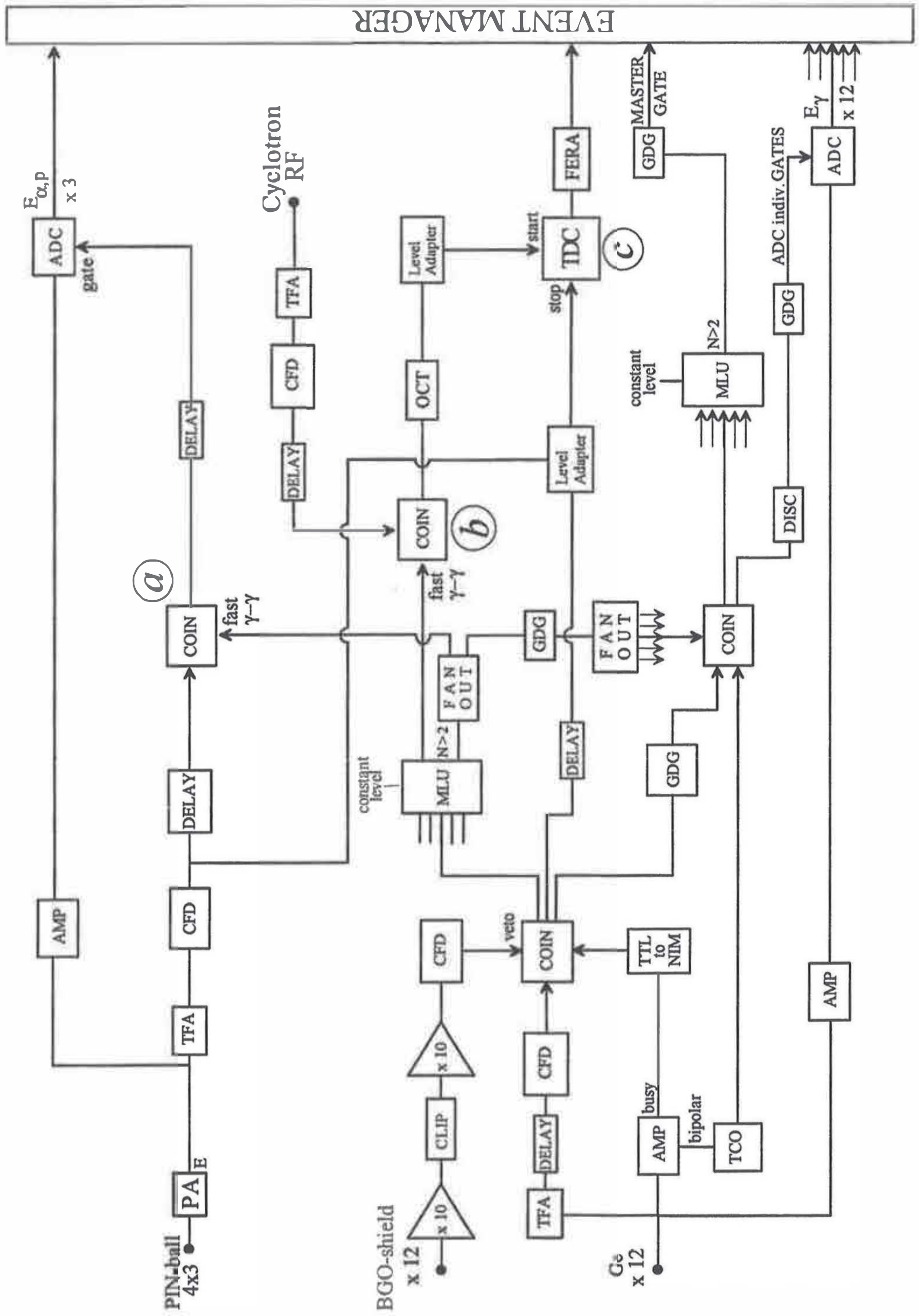

Figure 19. A block diagram of the electronics used in DORIS set-up.

3.4.2 DORIS electronics

The signal processing for the DORIS-array system is very similar to that for the TESSA3 system. Instead of the BGO-inner ball the DORIS set-up has a silicon detector array for the charged particle detection, which requires some additional electronics. The 12 PIN-diode detectors in the array are divided to three rings at detection angles of 45°, 75° and 135° with respect to the beam axis. Each ring of four detectors are coupled together in a shunt connection. The three preamplifier output signals from the PIN-diode detector rings are divided to a timing and energy signals. The energy signal is amplified in the usual manner by a spectroscopic amplifier and then fed into the ADC. The timing signal passes through the TFA and CFD units before feeding into the coincidence unit, indicated as *a* in Fig. 19. The particle-$\gamma\gamma$ coincidence condition was set as the gate for the silicon detector ADC. Time spectra are generated in the TDC unit for individual twelve Ge detectors and for the three rings of silicon charged particle detectors (*c* in Fig. 19). The start signal is the γ-γ event in coincidence with the cyclotron radio frequency (RF) signal and the stop signals are separate individual detector signals. The cyclotron RF signal related to the time of the beam pulse is a good and stable reference for the detector timing. The coincidence condition between cyclotron RF signal and the γ-γ event, indicated as *b* in Fig. 19, ensures that the particular γ-ray or α–particle is a prompt originating from the beam burst and not a random or so-called out of beam delayed event.

3.5 Liquid nitrogen filling system

An automated liquid nitrogen (LN2) filling system was constructed for the use in conjunction with the Ge-detector arrays at the JYFL accelerator laboratory. The γ-ray arrays used at JYFL consist of typically 12-25 Ge detectors with LN2 dewars to be filled 2-3 times a day, depending on the volume of the dewar. The filling system plays an essential role in maintaining the functionality of the in-beam γ-ray spectrometer and therefore reliability is the most important requirement for the system.

The filling system uses two 300 litre LN2 main dewars manually filled from the 3000 litre reservoir of the laboratory. Thermally insulated polyurethane tubes and cryogenic solenoid valves are used to deliver LN2 to the detector dewars. Each main dewar with a pressure of about 1.5 bar feeds a manifold with branches to the individual detectors. The requirement for the system controlling the solenoid valves and the filling procedure was that it should be reliable and relatively simple. These and other requirements are fulfilled by applying a programmable logic controller generally used in industrial process control. The controller is programmed to open and close the solenoid valves according to the given time parameters and the overflow information from the overflow sensors. The sensitive part of the sensor is a light emitting diode where the diode resistance dramatically changes when the diode is cooled down by the overflowing liquid nitrogen.

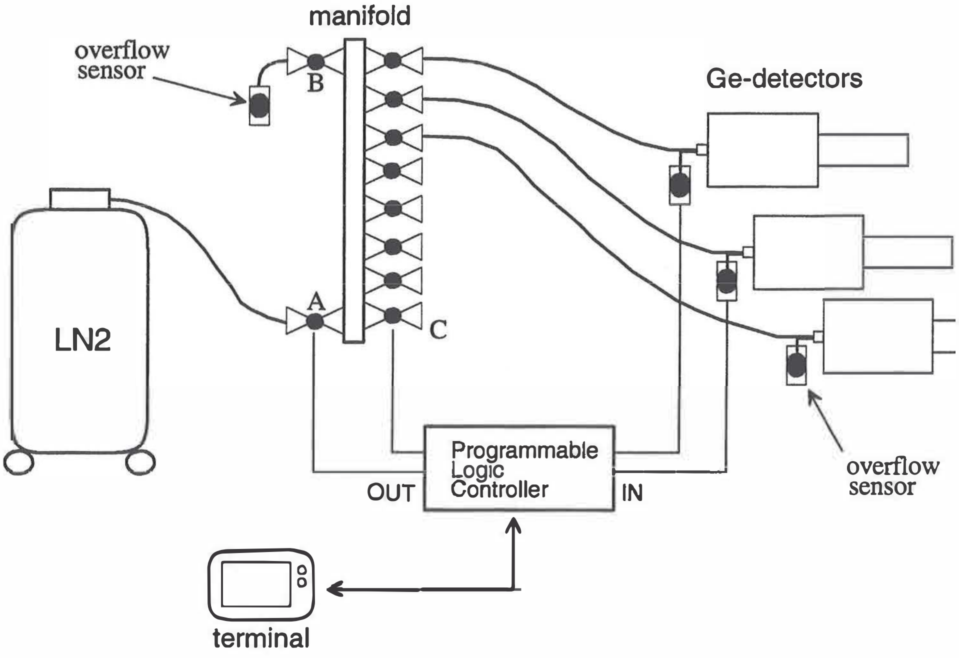

Figure 20. A schematic figure of the automated liquid nitrogen filling system.

The filling procedure starts by filling the manifold. The valve A is opened together with valve B. The nitrogen vapour flows through the manifold until the liquid nitrogen is detected by the manifold overflow sensor. The valve B is subsequently closed and the valves C to the detectors are opened, see Fig. 20. The valves C close individually when the overflow signal from the corresponding detector is received. The valve A is finally closed after the last detector dewar is filled. If the overflow signal is not observed within a given time period the corresponding valve closes and an alarm is given to the local terminal located in the cave and an email is sent to the personnel. The filling history and alarms can also be monitored from the World Wide Web. The controller is autonomous but needs a user interface for the setting of the parameters of the filling process and the monitoring of the system status. For this purpose a dedicated terminal has been connected to the controller serial port. The filling system has been used in large number of experiments at JYFL and it has turned out to be very reliable. The problems faced with the system have been mainly mechanical i.e. the limited life time of the polyurethane tubes at LN2 temperatures and ice formation in the bayonet tubes. Occasionally due to the extreme temperature conditions the properties of the temperature sensors' can change over a long period of time and need a readjustment.

3.6 Data analysis

The off-line analysis was performed using the coincidence data recorded onto the magnetic tapes. In the beginning of the experiments approximate gainmatch of the Ge detectors was done by tuning the gains of the linear amplifiers with a ^{60}Co γ-ray source. The final gain match was done off-line after the experiment by using spectra from a ^{152}Eu + ^{133}Ba mixed calibration source. In the case of thin target experiment the photons are emitted from the moving residue and so the Doppler effect was calculated. Also the recoil effect, caused by the evaporating alphas giving rise to an angular spread in the residual nuclei was taken into account by fine tuning the calibration coefficients with an internal calibration.

The efficiency of the Ge detectors to detect γ-rays is strongly energy dependent. Intensities extracted from spectra have to be corrected for detector efficiency when relative intensities of γ-transitions are needed. The photopeak area is scaled by an energy dependent factor determined from the efficiency curve obtained from a ^{152}Eu + ^{133}Ba calibration source whose intensities are accurately known.

The raw data was sorted into a two-dimensional $E_{\gamma1}$–$E_{\gamma2}$-matrix of the size of 4096×4096 channels. In the fusion-evaporation reaction work the charged particle identification was used to select the reaction channel as described in section 3.3. In the present work the data analysis and construction of the level scheme were performed using the ESCL8R software package written by D.C. Radford. [Ra95]

The angular distributions of the γ-rays were studied by obtaining information about transition multipolarities. In heavy-ion fusion-evaporation reactions, the residues are strongly forward peaking, thus the angular momentum alignment perpendicular to the beam direction is well preserved. In the DORIS array geometry, used in fusion-evaporation experiments, the detectors are in four rings at 37°, 78°,102° and 143° with respect to the beam direction. In order to extract angular distribution ratios the data were sorted into two matrices with the following angular combinations: (i) (37° or 143°) × all angles and (ii) (78° or 102°) × all angles, where first the x-axis and then the y-axis is given. By setting identical y-gates on desired γ–rays in both matrices coincidence spectra were created which were used to obtain the intensity ratio $R(E_\gamma) = I_\gamma(E_\gamma;\text{extreme angles}) / I_\gamma(E_\gamma; \approx 90°)$. This ratio is about 1.5 for stretched quadrupole and pure $\Delta I = 0$ transitions and about 0.8 for pure stretched dipole transitions. However, similar R ratios are possible for transitions of mixed multipolarity. In the case of $R < 0.8$, the transition can firmly be assigned as $\Delta I=1$, mixed M1/E2 type.

The angular distribution analysis in binary reactions is not so clear. Due to the reaction mechanism the angular distribution of the reaction partners are not so forward peaking and thus the γ-ray distribution is more obscure. In the TESSA3 array, used in the binary-reaction experiment, the Ge detectors are mounted at three different rings at 35°, 90° and 145° with respect to the beam direction. In spite of the fact that in binary reactions the angular distribution is more obscure, the angular distribution ratio analysis in the study of the Cd data was performed in a similar way as described above. The angular distribution ratios were found to be reasonable for the assignment of dipole and quadrupole transitions. The intensity ratio of coincidence γ-rays observed by the Ge detectors at extreme angles to those observed by the 90° Ge detectors was found to be 0.7 - 0.9 for dipole and 1.1 - 1.3 for quadrupole transitions.

Chapter 4

Band structures in ^{114}Cd and ^{116}Cd from heavy-ion collisions

4.1 Introduction

Ambiguities associated with the microscopic origin of low-lying collective states in even-mass Cd nuclei are still unresolved [Kus87,Ku92,Ca92,He95]. Especially the role of proton intruder configurations as well as deformation driving neutron $h^2_{11/2}$ configurations in these states is not well understood [Th93,Ju94]. These excitations are expected to reach their lowest energy in mid-neutron shell nuclei. Therefore it is important to extend systematic experimental studies of low- and moderately high-spin states to the Cd isotopes with A ≥ 114, nuclei which cannot be reached by heavy-ion induced fusion-evaporation reactions with stable beams and targets.

Recently, new experimental low-spin data [Ku92,Ap85,Za95] have rendered it possible to examine the systematics of the low-lying 0^+, 2^+ and 4^+ states from ^{106}Cd to ^{122}Cd. In ref. [Ku92] the crossing of the two lowest excited 0^+ states of different character was suggested between ^{114}Cd and ^{116}Cd. Moreover, clear evidence was found for associating one of those 0^+ states and the third excited 2^+ state in even-mass $^{106\text{-}120}$Cd nuclei with the lowest members of the 2p-4h proton intruder bands. However, it was also pointed out in ref. [Ku92] that in the vibrator picture the suggested 0^+ band head of the intruder band clearly plays the role of the two-quadrupole phonon state with an enhanced E2 transition to the 2^+_1 state.

Recent γ-ray studies of low and high-spin states in the even-mass $^{106-112}$Cd isotopes [Ku92,Th93,Ju94,Re95,Ke90,Ku90,De93] via compound-nucleus reactions have also shed new light on the intruder structures and the role of $h^2_{11/2}$ neutrons in the development of collectivity in these nuclei. However, due to the lack of available reactions, the extension of these studies to the mid-shell nucleus ^{114}Cd and further to the heavier Cd isotopes is difficult. One of the possible methods, used by Durell et al. [Du89], is to employ an efficient Ge-detector array in the detection of prompt γ-rays following fission. In this way yrast levels in even-mass $^{114-122}$Cd nuclei, in some cases up to $I = 14\hbar$, have been tentatively identified [Du89].

As discussed in section 2.2 an efficient detection of $\gamma\gamma$ coincidences from quasielastic and deep-inelastic heavy ion collisions offers another opportunity to study low- and moderately high-spin states in neutron-rich nuclei near the β-stability line. In this section results from such studies of ^{114}Cd and ^{116}Cd nuclei are presented.

4.2 Experimental methods

In the present experiments the thick-target method, discussed in section 2.3.2, was employed. A 30mg/cm^2 thick 97% enriched ^{116}Cd target was bombarded with 370 MeV ^{84}Kr ions (13% above the Coulomb barrier) delivered by the Jyväskylä K=130 cyclotron. For the $\gamma\gamma$ coincidence detection and the γ-ray multiplicity, sum-energy recording the TESSA3 array was employed as introduced in section 3.2.3. A large number of reaction products were identified in the analysis of the $\gamma\gamma$ coincidence data (Fig 3 in section 2.1). Population of yrast states up to I~10 $\hbar$ was observed in many nuclei. The transfer of neutrons from target to projectile and inelastic processes leading to the $^{112-116}$Cd nuclei were strong, while the transfer in opposite direction were very weak. Examples of gated γ-ray spectra for ^{116}Cd are shown in Fig. 21.

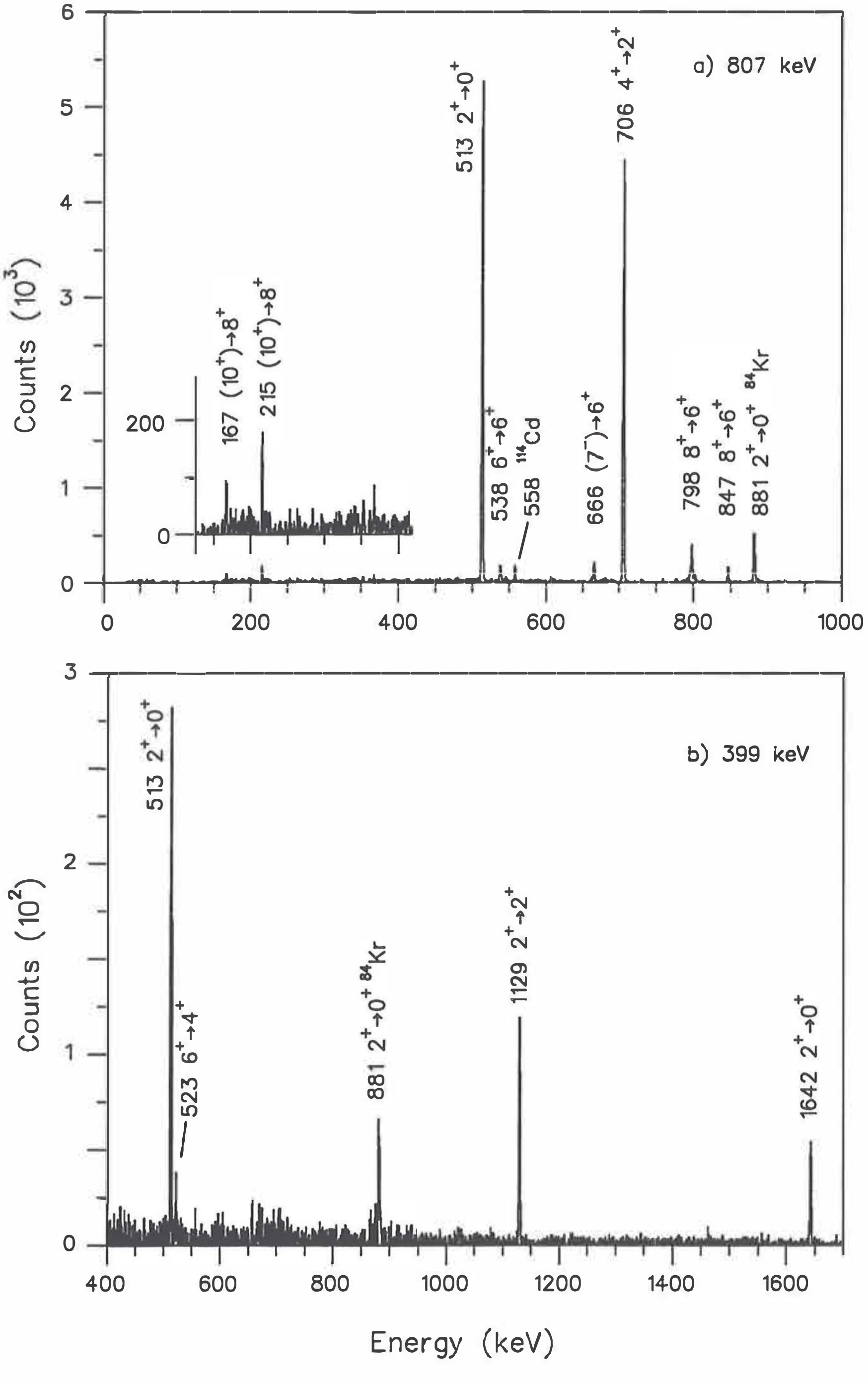

Figure 21. Gamma-gamma coincidence spectra for ^{116}Cd from ^{84}Kr + ^{116}Cd collisions: a) gated on the 807 keV $6^+\rightarrow4^+$ transition b) gated on the 399 keV $4^+\rightarrow2^+$ transition in the intruder band.

The ^{116}Cd nucleus was also investigated in the ^{86}Kr + ^{124}Sn collisions at 370 MeV bombarding energy. A ^{124}Sn target of 30 mg/cm^2 thickness was used and the experiment was performed using the DORIS array described in section 3.2.4 without the PIN-diode array for charged particle detection. This experiment was used to populate ^{116}Cd nucleus via deep-inelastic collisions. The yrast band was indeed populated up to I=16 $\hbar$. It is also remarkable that the intruder low spin states were not seen at all in this data set.

For obtaining information about transition multipolarities, we studied the possibilities of applying the γ-ray angular distribution method similar to the one we use in connection with fusion-evaporation reactions [Ju94], discussed in section 3.6. Consequently, this information was used for spin assignments.

Table 1. The γ-ray energies, intensities and $R = I_\gamma(35° \text{ or } 145°)/I_\gamma(90°)$ *angular distribution ratios for the transitions assigned to* ^{114}*Cd from the* ^{84}*Kr +* ^{116}*Cd experiment*

$E_\gamma{}^a$	I_γ	R-ratio	E_i (keV)	Assignment
236.7	1.0(2)	1.3(2)	2536	$(5^-)\rightarrow 5^-$
367.6	4.6(5)	1.6(3)	1733	$4^+\rightarrow 2^+$
403	< 0.3		2394	$6^+\rightarrow 6^+$
435.9	1.3(2)	1.5(3)	2736	$(7^-)\rightarrow 6^+$
448.5	1.9(2)	1.0(2)	1733	$4^+\rightarrow 4^+$
474.7	4.7(4)	1.16(7)	3145	$10^+\rightarrow 8^+$
546.8	2.1(3)	1.3(2)	3283	$(9^-)\rightarrow(7^-)$
558.3	294(6)	1.16(3)	558	$2^+\rightarrow 0^+$
567.9	2.5(3)	1.17(15)	3713	$12^+\rightarrow 10^+$
576.0	7.9(6)	0.97(8)	1134	$0^+\rightarrow 2^+$
661.8	1.9(4)	1.2(3)	2394	$6^+\rightarrow 4^+$
678.2	7.4(5)	1.17(8)	2670	$8^+\rightarrow 6^+$
706.4	28.9(10)	1.17(5)	1991	$6^+\rightarrow 4^+$
725.2	100	1.15(4)	1284	$4^+\rightarrow 2^+$
744.8	4.5(4)	0.86(9)	2736	$(7^-)\rightarrow 6^+$
805.9	9.1(6)	1.20(11)	1364	$2^+\rightarrow 2^+$
1110.5	2.4(3)	1.1(2)	2394	$6^+\rightarrow 4^+$
1015.2	9.0(6)	0.83(7)	2298	$5^-\rightarrow 4^+$
1173.8	5.3(4)	1.3(2)	1733	$4^+\rightarrow 2^+$
1364	6.0(6)		1364	$2^+\rightarrow 0^+$
1400	1.0(2)		1958	$3^-\rightarrow 2^+$

[a] *Accurate to 0.1 keV for most transitions. For weak transitions accurate to 0.5 keV.*

Table 2. The γ-ray energies, intensities and $R = I_\gamma(35° \text{ or } 145°)/I_\gamma(90°)$ angular distribution ratios for the transitions assigned to ^{116}Cd.

E_γ^a	I_γ^b	I_γ^c	R ratio	E_i (keV)	Assignment
166.7	0.04(1)	5.5(7)		3040	$(10^+) \rightarrow 8^+$
214.9	0.12(2)	14.5(7)	1.1(2)	3040	$(10^+) \rightarrow 8^+$
254.8	0.21(2)		1.3(1)	2503	$(5^-) \rightarrow 5^-$
262	0.010(2)			1642	$2^+ \rightarrow 0^+$
399.2	0.28(3)		1.2(2)	2042	$4^+ \rightarrow 2^+$
444	0.06(2)			2692	$(7^-) \rightarrow 5^-$
513.4	500(10)		1.18(2)	513	$2^+ \rightarrow 0^+$
523	0.09(2)			2564	$6^+ \rightarrow 4^+$
538		14.5(7)		3578	$(12^+) \rightarrow (10^+)$
538.1	0.15(3)		1.2(1)	2564	$6^+ \rightarrow 6^+$
580.3	0.16(3)		1.3(1)	2828	$(7^-) \rightarrow 5^-$
666.5	0.34(3)		1.0(1)	2692	$(7^-) \rightarrow 6^+$
668	0.07(2)			1950	$2^+ \rightarrow 0^+$
705.9	100(1)	100(4)	1.26(3)	1219	$4^+ \rightarrow 2^+$
769.1	3.0(1)		1.01(4)	1282	$0^+ \rightarrow 2^+$
798.2	0.9(1)	23(2)	1.2(1)	2824	$8^+ \rightarrow 6^+$
802		7.6(7)		4380	$(14^+) \rightarrow (12^+)$
802.6				2828	$(7^-) \rightarrow 6^+$
807.3	6.1(1)	63(3)	1.27(5)	2026	$6^+ \rightarrow 4^+$
822.7	0.35(4)		1.2(1)	2042	$4^+ \rightarrow 4^+$
846.8	0.23(2)	15(2)	1.3(1)	(2873)	$8^+ \rightarrow 6^+$
866.9	3.3(1)		1.01(4)	1380	$0^+ \rightarrow 2^+$
963		< 3.4		(5343)	$(16^+) \rightarrow (14^+)$
1024	0.2(1)			3050	$\rightarrow 6^+$
1029.4	1.30(5)		0.80(5)	2248	$5^- \rightarrow 4^+$
1129.2	1.80(4)		1.28(7)	1642	$2^+ \rightarrow 2^+$
1345.7	0.07(2)		1.4(4)	2564	$6^+ \rightarrow 4^+$
1407.9	0.54(8)		0.70(7)	1921	$3^- \rightarrow 2^+$
1438.0	0.38(4)		0.70(8)	1950	$2^+ \rightarrow 2^+$
1528.5	1.00(4)		1.3(1)	2042	$4^+ \rightarrow 2^+$
1642.6	1.2(1)			1642	$2^+ \rightarrow 0^+$

[a] *Accurate to 0.1 keV for most transitions. For weak transitions accurate to 0.5 keV.*

[b] *From the ^{84}Kr+^{116}Cd experiment*

[c] *From the ^{86}Kr+^{124}Sn experiment*

4.3 Level scheme of ^{114}Cd and ^{116}Cd

Partial level schemes established in the present work for ^{114}Cd and ^{116}Cd are shown in Figs. 22 and 23, respectively. For ^{114}Cd our multipolarity assignments confirm the spins and positive parities of the yrast levels up to the 12^+ state tentatively identified in refs. [Du89,Bl95]. Earlier, an intruder band up to the 6^+ state was identified on top of the first excited 0^+ state (0^+_2) at 1134 keV in ^{114}Cd [Ku92,Fa88,Mh84]. In the present work we also see this band but its 6^+ member was observed to lie 6 keV lower than the one tentatively identified in ref. [Fa88]. The 662 and 1110 keV transitions have angular distribution ratios typical for the stretched E2 transitions.

For the yrast band in ^{116}Cd (Fig. 23) our data confirm the earlier tentative assignments [Du89,Bl94] up to the 6^+ level while at higher spins our level scheme differs from that observed in refs. [Du89,Bl94]. As shown in Fig. 23, two close-lying 8^+ levels were found which fed from the tentatively assigned 10^+ level. The 8^+ assignments for the 2824 and 2873 keV levels are based on the angular distribution ratios for the 798 and 847 keV transitions being consistent with the stretched E2 character. Side-feeding transitions of 1024, 803, 666, 1029 and 1408 keV energy populating the yrast band were also found most likely based on $\nu h_{11/2}g_{7/2}$ configurations. The complementary data from ^{86}Kr + ^{124}Sn collisions gives additional information of the high-spin states in ^{116}Cd up to $16\hbar$. Previously unreported sequence of 538, 802 and 963 keV transitions is identified above the 10^+ state.

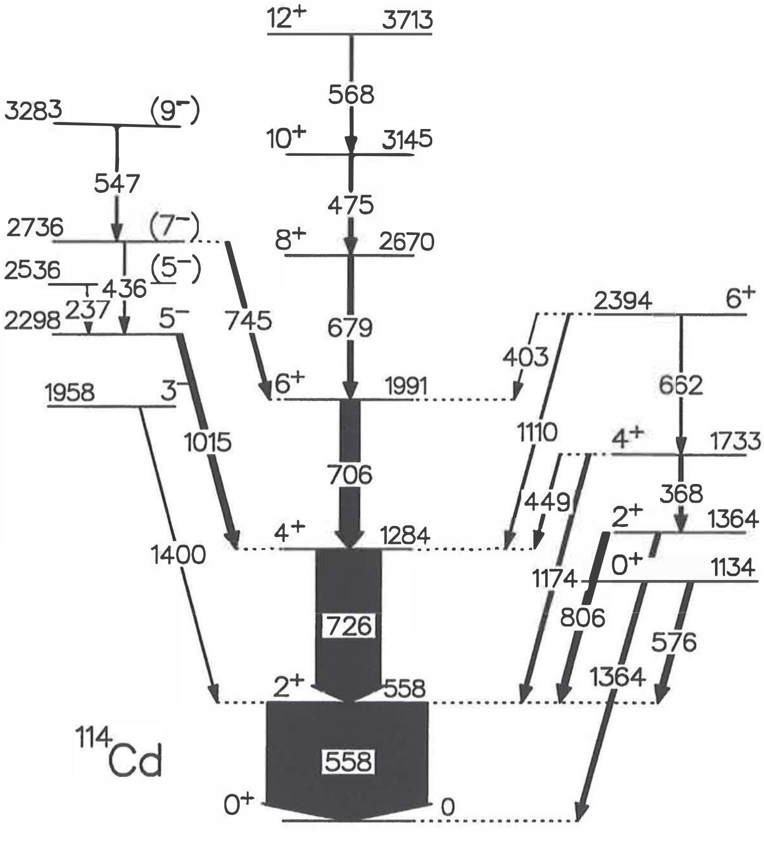

Figure 22. Partial level scheme of ^{114}Cd from the present work. The widths of the arrows are related to the coincidence intensities of the γ-ray transitions.

The 1380 keV 0^+, 1642 keV 2^+ and 2042 keV 4^+ states have been established previously [Bl94], and the present angular distribution ratios for the de-exciting transitions are consistent with those spin and parity assignments. A 523 keV transition was observed to populate the 2042 keV 6^+ state establishing a level at 2564 keV. This state decays also via the 538 and 1345 keV transitions to the yrast 2026 keV 6^+ and 1219 keV 4^+ states, respectively. The 6^+ assignment for the 2564 keV level is mainly based on the stretched E2 character of the 1345 keV transition. Thus, for the first time in ^{116}Cd, an intruder band based on the second excited 0^+ state (0^+_3) at 1380 keV has been identified up to the 6^+ member. This observation supports the idea of ref. [Ku92], where the 1380 keV 0^+_3 (rather than the first excited 1282 keV 0^+_2 state) and the 1642 keV 2^+_3 states in ^{116}Cd were suggested to be members of a possible intruder band. The 0^+_2 state in ^{116}Cd is fed from a higher lying 2^+ state as shown in Fig 23.

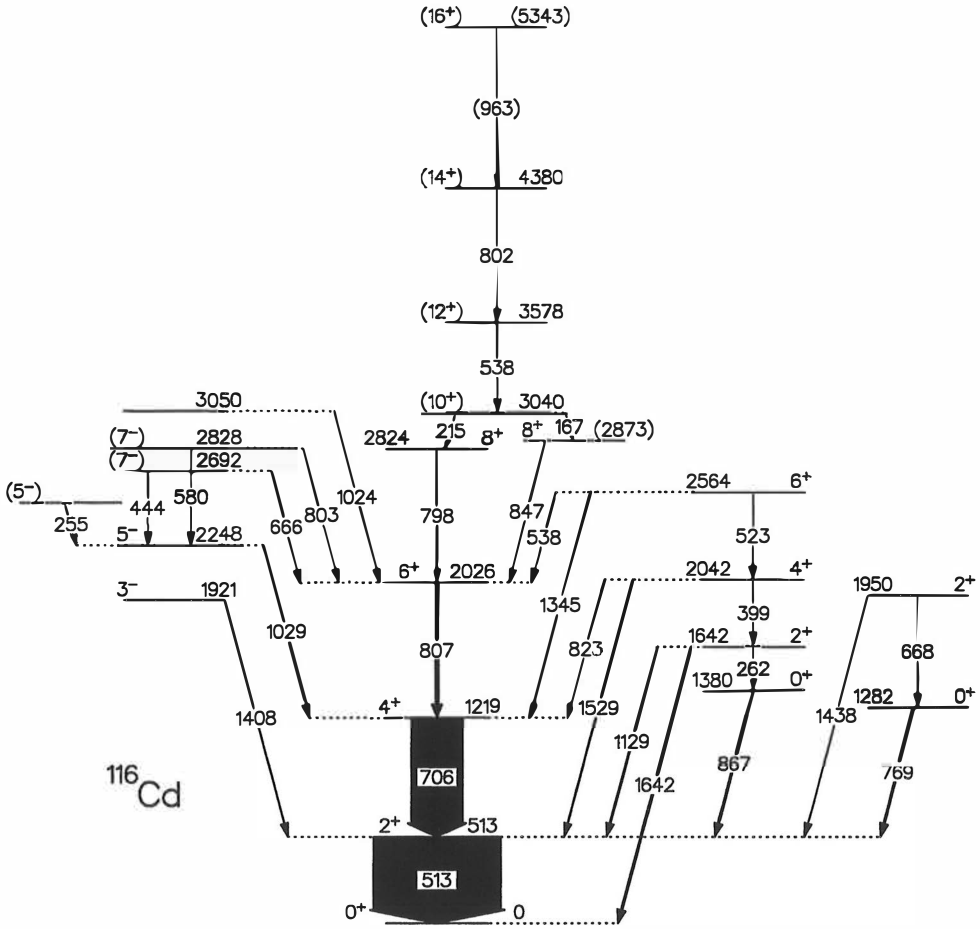

Figure 23. Partial level scheme of ^{116}Cd. The widths of the arrows are related to the coincidence intensities of the γ-ray transitions.

4.4 Level systematics for even-mass Cd isotopes

Based on the present results and other available data for the even-mass $^{106\text{-}122}$Cd isotopes [Ku92, Th93, Ju94, Ap85, Za95, Re95, Du89], the energy systematics for the yrast levels up to the 10^+ state and for the two lowest excited 0^+ states labelled as in ref. [Ku92] by 0^+_A and 0^+_B as well as for the intruder bands based on the 0^+_A states are shown in Fig. 24.

With the present results included a smooth behaviour of the yrast 10^+ states is observed. These states presumably are mainly of the neutron $h^2_{11/2}$ character [Reg95] minimizing their excitation energy at N = 70 like the first excited 2^+_1 and 4^+_1 states. The microscopic origin of this behaviour is not well-understood [Za95]. The new yrast 8^+ state in ^{116}Cd lies higher than in the neighbouring even-mass isotopes (Fig. 24). A similar but smaller kink is visible in the energy systematics of the yrast 6^+ states. These irregularities may indicate that the ground-state band is losing collectivity with increasing spin and therefore its states become more sensitive to small changes of the wave function. These changes might be due to sub-shell effects or mixing.

The new 2873 keV 8^+ state in ^{116}Cd strongly fed from the (10^+) state (Fig.23) could be a member of the neutron $h^2_{11/2}$ multiplet. A similar 8^+ state was identified in ^{110}Cd [Ju94]. The high-K proton $g^{-2}_{9/2}$ 8^+ state has an excitation energy of 3.044, 3.111 MeV and 3.187 MeV in ^{106}Cd, ^{108}Cd and ^{110}Cd [Th93,Ju94,Re95], respectively, and as a proton state it should stay at about the same energy in the heavier Cd nuclei. Therefore in ^{116}Cd it is expected to lie well above the yrast line.

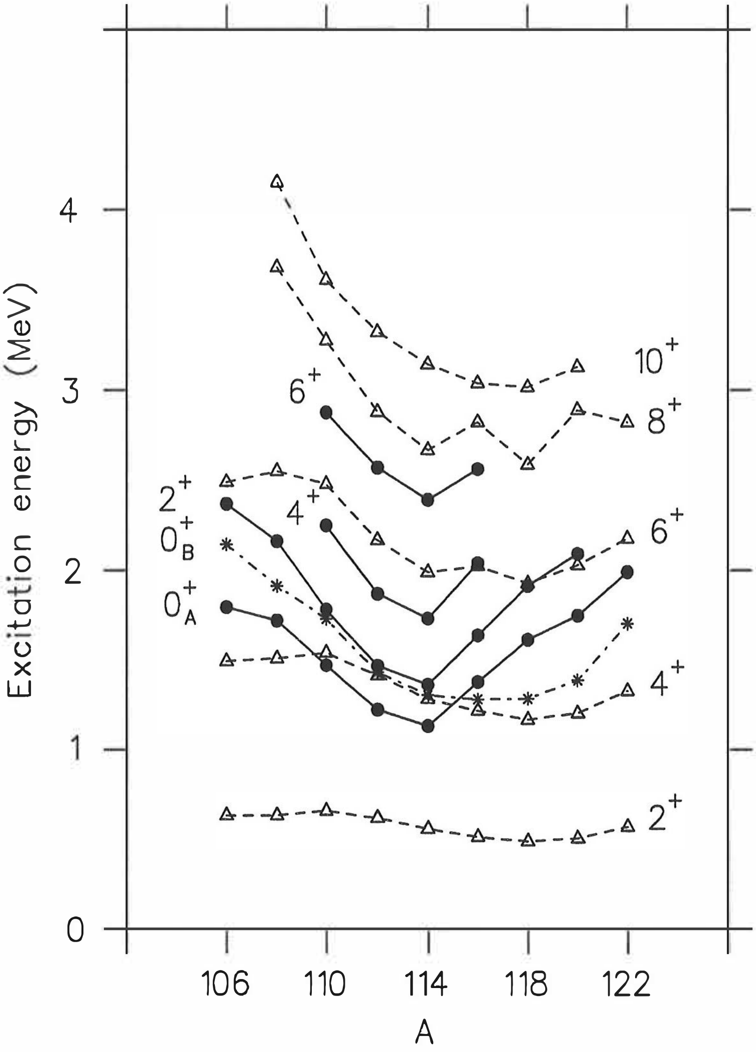

Figure 24. Systematics of yrast levels (open triangles) and intruder bands (filled circles) in even-mass Cd nuclei. Energies of the 0^+_B states are also shown.

In accordance with the intruder picture involving 2p-4h proton excitations across the Z = 50 shell gap [He87], the suggested intruder states in even-mass Cd isotopes reach their minimum excitation energy in ^{114}Cd i.e. in the middle of the neutron shell (Fig. 24). They form a V shaped pattern very similar to that observed for example for the 2p-1h intruder $g^{-1}_{9/2}$ bands in odd-mass Sb nuclei [Sh79].

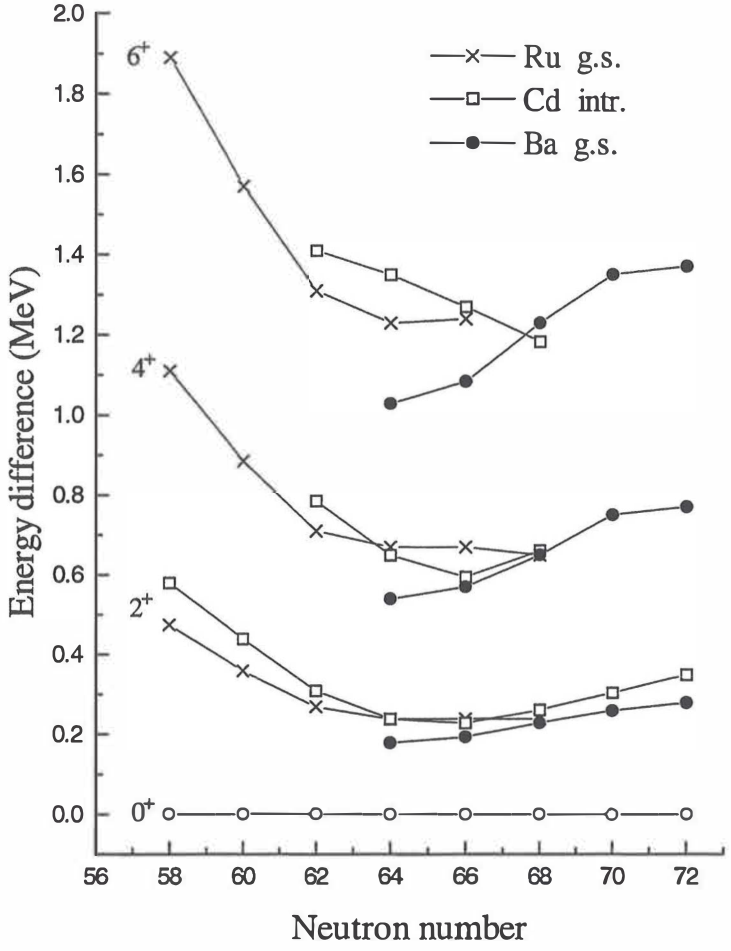

Figure 25. Proposed members of the intruder bands in even-even $^{106\text{-}120}$*Cd compared to the members of the ground-state bands of the even-even Ru and Ba isotones* [Ku92]. *The energies of the intruder* 0^+ *states in Cd isotopes are normalized to 0 MeV.*

Furthermore, in accordance with the (2p-4h) intruder analog state picture [He92], these bands in even-mass Cd nuclei have an energy pattern similar to that for the ground-state bands in the corresponding 6 valence proton Ru (0p-6h) and Ba (6p-0h) isotones (Fig. 25)

[Ku92]. The resemblance between the new intruder band based on the 0^+_3 (0^+_A) state in ^{116}Cd and the ground-state band of the ^{124}Ba isotone [Co74] is even more impressive indicating that the energies of the band members are not much affected by mixing with other states. As pointed out in ref. [Ku92], the B(E2; 0^+_3 - 2^+_1) value in ^{116}Cd is about 30 W.u. while the B(E2; 0^+_2 - 2^+_1) value is only about 1 W.u. [Ma89], revealing that the intruder 0^+_3 state (but not the 0^+_2 state) in ^{116}Cd plays also the role of a two-quadrupole phonon state in the vibrator picture. The role of mixing in even-mass Cd nuclei is still an intriguing question [Ca92,Za95]. Many of the peculiar electromagnetic properties of the low-spin states in mid-shell Cd isotopes have been well-reproduced by introducing a strong mixing of vibrational and intruder states [Kus87,He95]. However, as pointed out above and in refs. [Ku92,Ca92,Za95], there are many properties in even-mass Cd nuclei which more support the no-mixing picture. Therefore the role of proton-intruder configurations in generating collectivity of these nuclei at low spin still remains the enigma.

Chapter 5

Coexisting structures in ^{115}Sn and ^{116}Sn

5.1 Introduction

Many of the collective properties of low-lying states in midshell Sn nuclei can be reproduced by calculations involving only neutron quasi-particle excitations [Gu76,Gu78,Sa95,In92]. However, strong population of low-lying 0^+states in even-mass Sn isotopes following two-proton transfer reactions has been presented as evidence that intruder $\pi g_{9/2}^{-2} g_{7/2}^{2}$ configurations are also present in these states [Fi77]. Rotational structures up to 12^+states in ^{112}Sn, ^{114}Sn, ^{116}Sn and ^{118}Sn, based on these deformed $\pi g_{7/2}^{2} g_{9/2}^{-2}$ structures were identified by Bron et al. [Br79] via (α,2n) reactions. Large E2 and E0 rates between low-spin states of stable even-mass Sn nuclei were associated with these intruder structures [Bac81,Ju94]. In ^{112}Sn and ^{114}Sn these bands were later extended to higher spins [Ha88,Ha89]. Bands involving $h_{11/2}$ protons and exhibiting a smooth band termination phenomenon have also been identified to very high spin in light Sn isotopes [Wa93,Wa94]. In odd-mass Sn nuclei, one might expect rotational bands to arise from the coupling of an odd neutron to the intruder band of the neighbouring even-mass nucleus. Indeed, rotational bands have been established in ^{111}Sn and ^{115}Sn and interpreted in this way [LaF95,Ga95,Se97].

As the intruder mechanism in Sn nuclei is thought to be due to the interaction between the protons involved in the 2p-2h excitations across the $Z = 50$ shell gap and the neutrons occupying the $N = 50$ - 82 shell, the corresponding intruder states should minimize their energies at $N = 66$, ie. in ^{116}Sn. This nucleus was extensively studied by the Jyväskylä-

Uppsala collaboration at low spin [Ka79] but is difficult to produce in heavy-ion reactions. In the present work, the near yrast states of the nuclei ^{115}Sn and ^{116}Sn were investigated using weak ^{18}O induced fusion evaporation reaction channels where an α particle is evaporated with neutrons. In ^{116}Sn the intruder band was observed up to $I = 20\hbar$ and in ^{115}Sn four rotational bands were identified.

5.2 Experimental methods

Relatively high-spin states of ^{115}Sn and ^{116}Sn can be excited by utilizing weak fusion channels involving both neutron and alpha-particle evaporations. In the present work we used the ^{104}Ru(^{18}O,α2n) ^{116}Sn and ^{104}Ru(^{18}O,α3n) ^{115}Sn reactions. In the first experiment a 0.6 mg/cm^2 thick target on a 5mg/cm^2 gold backing was bombarded with 65 MeV ^{18}O ions from the Jyväskylä K130 cyclotron. To prevent Doppler broadening of high-energy γ–rays from short-lived high-spin states a second run with an unbacked 0.6 mg/cm^2 thick target was also carried out. In the experiments with backed and unbacked targets 590 and 400 million γ-γ coincidence events were recorded, respectively.

The dominant fusion-evaporation channels in the reactions detailed above are the pure neutron evaporation channels leading to Te nuclei. Yields for the reactions producing the ^{115}Sn and ^{116}Sn nuclei were roughly 5% and 1% of the yield for the most strongly populated nucleus (^{118}Te) in the reaction as discussed in section 2.1. In order to resolve the weak (^{18}O,αxn) channels from the dominant xn- channels, the PIN-diode array was used for charged-particle detection (see section 3.3). Gamma-rays up to the energy of about 1.9 MeV were detected by the DORIS array, described in section 3.2.4. Gamma-gamma coincidences as well as γ-γ particle coincidences were collected. By selecting only those γ-γ events that occurred in coincidence with the detection of an alpha particle, very clean γ-ray spectra were obtained for ^{115}Sn and ^{116}Sn.

The ^{115}Sn nucleus was also investigated in the ^{100}Mo(^{18}O,3n) reaction at 62 MeV bombarding energy. A ^{100}Mo target of 1 mg/cm^2 thickness on a gold backing was used and the experiment was performed in the same manner as the experiments described above. Gamma-ray energies up to approximately 4 MeV were recorded. This experiment was dedicated for a study of ^{112}Cd produced via a weak α2n evaporation channel, but it also produced ^{115}Sn nuclei. A total of 400 million γ - γ coincidence events were recorded in this experiment. Analyses of the data and construction of the level schemes were performed using the ESCL8R software package. The data from the backed-target runs were used to deduce transitions multipolarities as described in section 3.6

5.3 Experimental results

5.3.1 The level scheme of ^{116}Sn

The level scheme of ^{116}Sn built from the data obtained in the ^{104}Ru(^{18}O,α2n) experiments is shown in Fig. 26. On the left side positive parity band 1 represents the intruder band based on the deformed 2h-2p proton intruder configuration. On the right hand side are the spherical states built on neutron excitations. Energies, intensities, R ratios and ordering of the γ transitions are listed in Table 3. The level scheme of ^{116}Sn was known previously up to the 5388 keV 12^+ state [Br79,Poel80]. These observations are confirmed in the present data and level scheme was extended to higher spins.

The spectrum gated by the 680 keV $8^+ \to 6^+$ transition in the intruder band is shown in Fig. 27a. In this spectrum, a previously unreported sequence of 925, 916, 999 and 1094 keV transitions is identified above the 12^+ state. Angular distribution ratios indicate a stretched quadrupole character for the first three of these transitions. The 6313, 7229 and 8228 keV levels are therefore assigned with I^π = 14^+, 16^+ and 18^+, respectively. The multipolarity information for the topmost 1094 keV transition was not obtained because the peak is contaminated by the tail of the strong $4^+ \to 2^+$ 1097 keV peak and the peak is Doppler broadened in the backed-target data. Weak side-feeding transitions populating the intruder band were also found.

The previously known 4879 keV 11^- state [Po80] was found to be fed by a relatively intense cascade of the 1099, 235, 131, 315 and 423 keV transitions. Angular distribution ratios in the current work suggest that the 1099 keV transition is of stretched E2 type, while the other transitions show angular distribution ratios consistent with stretched dipole transitions. The 367, 447 and 738 keV cross-over transitions confirm that the 6213, 6344, 6659 and 7082 keV states are of the same, negative parity.

Due to its long lifetime [Poel80], coincidences across the yrast 10^+ state (τ =833 ns) were difficult to observe in the current work. However, in the spectra gated on the 131, 315 and 423 keV transitions, many new transitions are present, as shown in Fig. 27b for the 131 keV gate. Inspection of the spectra gated on these new transitions led to a level structure where the 1155, 1335, 1615 and 1783 keV transitions populate a level at an energy of 3546 keV, consistent with the excitation energy of the yrast 10^+ state. All the states in the level structure linked by the 115, 520 and 717 keV transitions to the negative-parity states and feeding into the 3546 keV level are assigned as having positive parity.

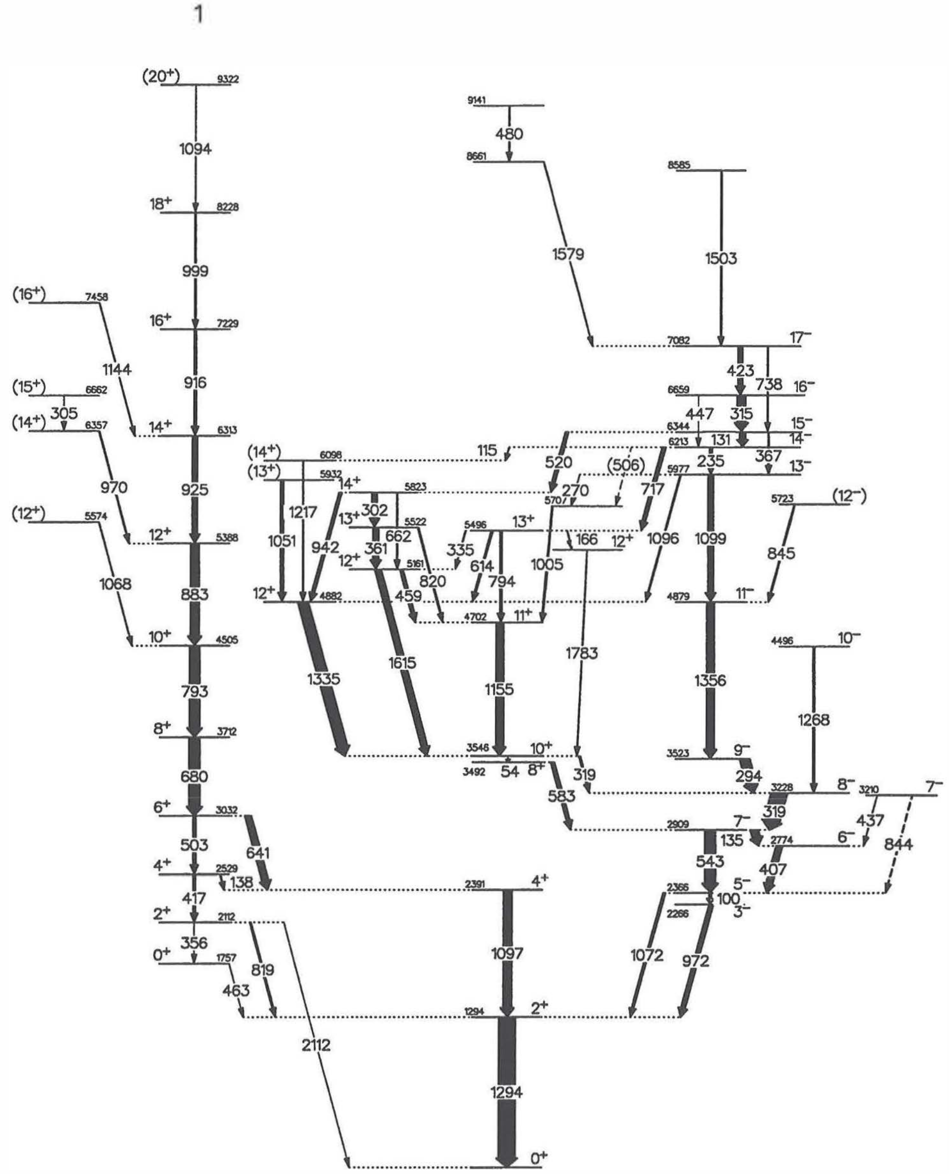

Figure 26. The level scheme of ^{116}Sn from the present work. The transitions and level energies are given in keV. The widths of the arrows are related to the coincidence intensities of the γ-ray transitions as obtained from the ^{104}Ru(^{18}O,α2n) reaction at 65 MeV bombarding energy within a coincidence time window of about 100ns. For completeness, the 2112 keV $2^+ \rightarrow 0^+$ transition is also shown, although it is outside of the energy range in the present experiment.

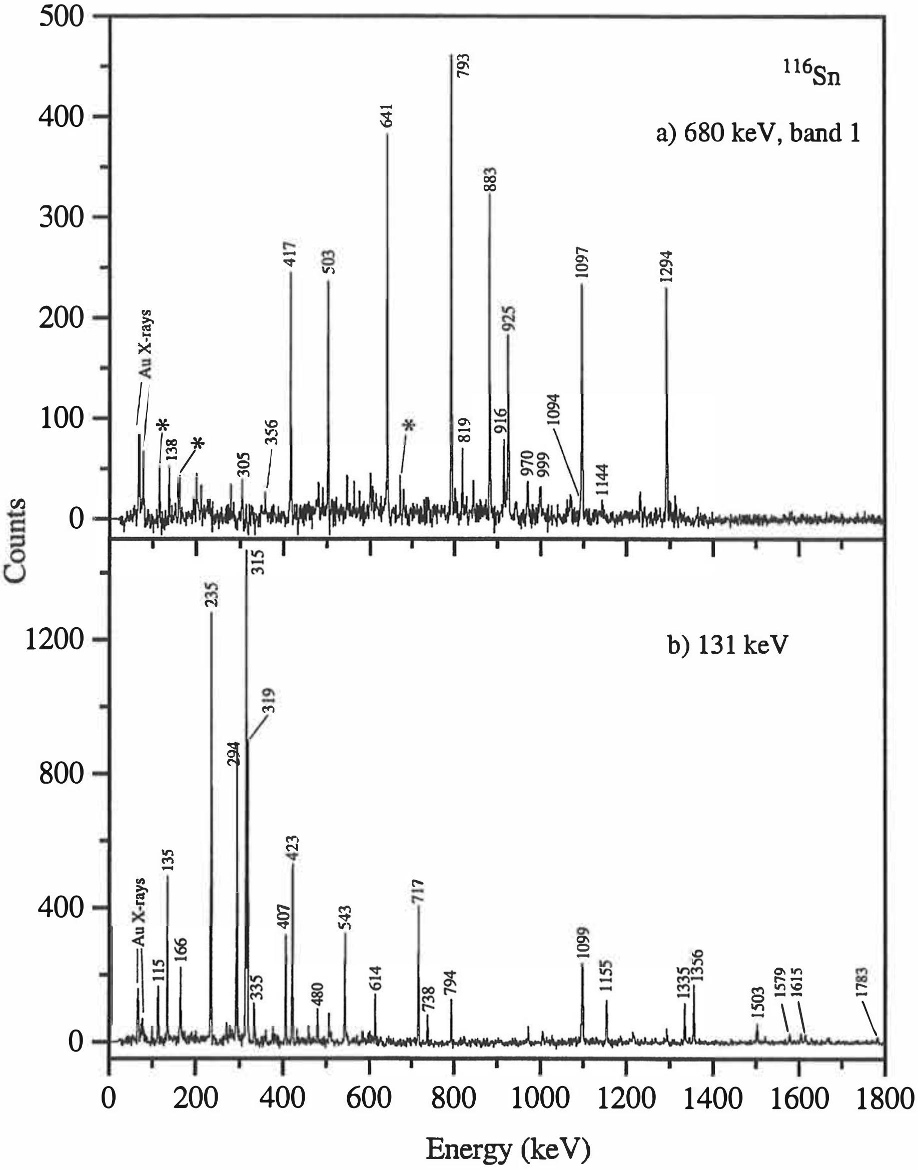

Figure 27. γ-γ coincidence spectra for ^{116}Sn following the ^{104}Ru(^{18}O,α2n) reaction at 65 MeV bombarding energy. The spectra are extracted from the α-gated matrix with the γ gates set on the a) 680 keV and b) 131 keV transitions. Transitions marked by an asterix belong to ^{118}Sb.

Table 3. Summary of results for ^{116}Sn.

E_γ(keV)	I_γ	R ratio	E_i(keV)	I_i	I_f
54 (9)	<0.1		3546	10^+	8^+
99.9(1)	2.9(2)	0.94(12)	2366	5^-	3^-
114.9(1)	1.1(1)		6213	14^-	14^+
131.1(1)	15.6(5)	0.79(7)	6344	15^-	14^-
135.4(1)	19.0(7)	0.77(5)	2909	7^-	6^-
138.2(4)	1.4(2)		2529	4^+	4^+
166.1(1)	1.9(1)	0.7(2)	5496	13^+	12^+
270.3(2)	0.5(9)		5977	13^-	$ $
235.4(1)	9.3(3)	0.81(5)	6213	14^-	13^-
294.5(1)	28.8(10)	0.88(2)	3523	9^-	8^-
301.5(1)	15.2(6)	0.80(8)	5823	14^+	13^+
305.1(1)	1.0(1)		6662	(15^+)	(14^+)
315.4(1)	26.1(9)	0.91(9)	6659	16^-	15^-
318.8(1)	4.8(3)		3546	10^+	8^-
319.1(1)	45(2)	0.87(2)	3228	8^-	7^-
334.7(1)	2.2(2)	1.0(3)	5496	13^+	12^+
355.6(4)	0.5(2)		2112	2^+	0^+
360.9(1)	17.6(9)	0.94(10)	5522	13^+	12^+
366.6(1)	3.9(2)		6344	15^-	13^-
407.3(1)	19(2)	0.82(6)	2774	6^-	5^-
416.9(1)	12.8(8)		2529	4^+	2^+
422.6(1)	15.0(5)	0.87(6)	7082	17^-	16^-
437.2(3)	0.9(2)		3210	7^-	6^-
447 (1)	0.5(1)		6659	16^-	14^-
459.3(1)	10.4(9)	1.20(10)	5161	12^+	11^+
463 (1)	<0.1		1757	0^+	2^+
480.2(1)	2.0(1)		9141		
502.8(1)	10.7(4)		3032	6^+	4^+
505.6(3)	0.3(1)		6213	14^-	
520.3(1	10.3(4)	0.79(9)	6344	15^-	14^+
542.8(1)	30.8(12)	0.97(15)	2909	7^-	5^-
583.2(1)	11.4(6)		3492	8^+	7^-
613.8(1)	5.1(3)	1.26(12)	5496	13^+	12^+
641.2(4)	22.7(9)	1.31(7)	3032	6^+	4^+
662.4(2)	2.9(4)	1.4(3)	5823	14^+	12^+
679.6(3)	31.1(12)	1.29(7)	3712	8^+	6^+
717.0(1)	10.5(4)	0.69(7)	6213	14^-	13^+
738.1(1)	2.5(3)		7082	17^-	15^-
793.4(1)	29.2(11)	1.26(7)	4505	10^+	8^+
794.0(1)	7.0(6)	1.40(6)	5496	13^+	11^+
818.8(1)	5.9(11)		2112	2^+	2^+
820.4(1)	4.0(4)	1.14(20)	5522	13^+	11^+
844 (2)	1.9(14)		3210	7^-	5^-
844.6(1)	3.6(3)	1.2(3)	5723	(12^-)	11^-

Table 3. continued

E_γ(keV)	I_γ	R ratio	E_i(keV)	I_i	I_f
882.8(4)	25.5(9)	1.42(8)	5388	12^+	10^+
915.8(1)	7.1(4)	1.2(2)	7229	16^+	14^+
925.4(1)	15.3(6)	1.26(11)	6313	14^+	12^+
941.6(1)	8.7(5)	1.3(2)	5823	14^+	12^+
970.0(1)	2.6(3)		6357	(14^+)	12^+
972.5(1)	12.9(14)	0.7(2)	2266	3^-	2^+
998.7(1)	3.5(3)	1.3(2)	8228	18^+	16^+
1005.3(2)	4.0(8)		5707		11^+
1050.7(2)	10.3(11)		5923	(13^+)	12^+
1068.4(3)	1.2(3)		5574	(12^+)	10^+
1072.2(2)	6.8(6)		2366	5^-	2^+
1094.0(10)	1.0(5)		9322	(20^+)	18^+
1095.9(2)	3.2(3)		5977	13^-	12^+
1097.3(1)	25(2)	1.53(9)	2391	4^+	2^+
1098.9(1)	17.0(7)	1.44(3)	5977	13^-	11^-
1143.9(2)	1.4(2)		7458	(16^+)	14^+
1154.9(1)	23.2(12)	1.1(14)	4702	11^+	10^+
1217.1(2)	2.4(7)		6098	14^+	12^+
1267.7(1)	4.8(4)		4496	10^-	8^-
1293.8(1)	48(3)	1.49(9)	1294	0^+	2^+
1335.2(1)	30(2)	1.2(2)	4882	12^+	10^+
1356.1(1)	23.7(10)	1.46(3)	4879	11^-	9^-
1503.4(1)	3.2(3)	1.0(2)	8584		17^-
1579.0(2)	1.4(2)		8661		17^-
1614.7(1)	19.2(9)	1.26(15)	5161	12^+	10^+
1783.5(2)	2.0(10)		5330	12^+	10^+
2112.4(2)	7(2)		2112	2^+	0^+

5.3.2 The level scheme of ^{115}Sn

The results for ^{115}Sn as obtained from the present work are summarised in table 4 and Fig. 28. The main part of the level scheme emanates from the ^{104}Ru(^{18}O,α3n) reaction which provided very clean data due to α gating. The complementary ^{100}Mo(^{18}O,3n) data gives additional support in the assignment of bands to ^{115}Sn. Also, high-spin states were more strongly populated in this reaction.

Previously, isomeric $7/2^+$ and $11/2^-$ states in ^{115}Sn were known at 613 and 713 keV, respectively [ToI]. Following light ion induced reactions, excited states have been observed up to $I = 27/2$ [Has79,Ma75,Vis91]. Very recently, a rotational band was reported by Sears et al. [Se97]. Hashimoto et al. assigned positive parity for the 3509, 3666, 3839 and 4272 keV yrast states based on angular distribution and conversion coefficient data. The angular distribution ratios in the current work are consistent with these assignments.

In addition to the intense 506 keV transition, weaker transitions of 124, 251 and 290 keV energy were observed to de-excite the 3509 keV $21/2^+$ state. The 3385 keV level, fed by the 124 keV transition, decays via levels at 2685 and 1945 keV to the yrast $11/2^-$ and $15/2^-$ states, as observed in ref. [Vis91]. The 124 and 700 keV transitions are of $\Delta I = 1$ type, whereas the 739 keV transition has an R ratio consistent with stretched quadrupole character. This suggests spin values 13/2, 17/2 and 19/2 for the 1945, 2685 and 3385 keV states, respectively. The 1945 and 2685 keV states are assigned negative parity based on the R ratios for the 1232, 660 and 319 keV transitions. The 3219 keV state we assign with $I^\pi = 17/2^+$ on the basis of the stretched quadrupole and dipole type of the 290 and 1194 keV transitions, respectively. A level at 3959 keV was reported in ref. [Vis91]. The R ratio for the 450 keV transition depopulating this state is that of a $\Delta I = 1$ dipole transition suggesting either $I = 19/2$ or $I = 23/2$ for this level.

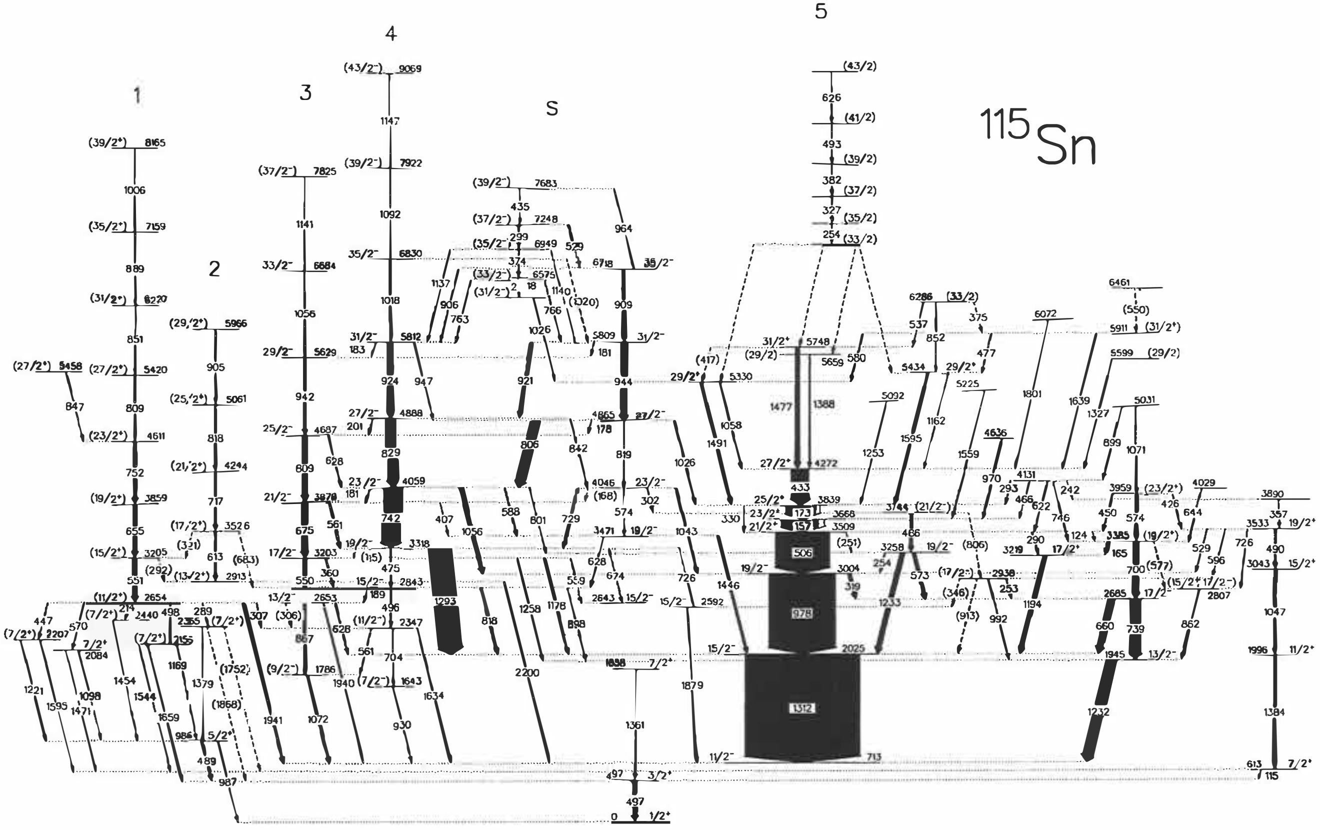

Figure 28. The level scheme of ^{115}Sn from the present work. The transitions and level energies are given in keV. The widths of the arrows are related to the coincidence intensities of the γ-ray transitions as obtained from the ^{104}Ru(^{18}O,α3n) reaction at 65 MeV bombarding energy within a coincidence time window of about 100ns.

Table 4. Summary of results for ^{115}*Sn.*

E_γ(keV)	I_γ^a	R ratio	Multip.	E_i(keV)	I_i	I_f
115.2(2)	<0.2			3318	$19/2^-$	$17/2^-$
115.4(1)	2.6(2)		E2	613	$7/2^+$	$3/2^+$
124.1(1)	1.6(1)	0.84(15)	M1	3509	$21/2^+$	$(19/2^+)$
156.8(1)	157(5)	0.76(1)	M1	3666	$23/2^+$	$21/2^+$
165.4(1)	5.0(3)	0.75(13)	M1	3385	$(19/2^+)$	$17/2^+$
167.9(4)	0.35(12)			4046	$23/2^-$	$21/2^-$
173.0(1)	129(4)	0.80(1)	M1	3839	$25/2^+$	$23/2^+$
177.6(2)	0.72(10)			4865	$27/2^-$	$25/2^-$
180.7(3)	0.30(9)			5809	$31/2^-$	$29/2^-$
181.0(1)	2.7(3)	0.90(14)		4059	$23/2^-$	$21/2^-$
183.3(3)	0.38(8)			5812	$31/2^-$	$29/2^-$
189.3(2)	1.1(3)			2843	$15/2^-$	$13/2^-$
201.3(1)	1.7(2)			4888	$27/2^-$	$25/2^-$
213.7(1)	0.8(2)			2654	$(11/2^+)$	$(7/2^+)$
218.4(1)	1.9(1)	0.8(2)	M1	6575	$(33/2^-)$	$(31/2^-)$
242.0(2)	0.7(2)			4141		
251.4(3)	1.0(3)			3509	$21/2^+$	$19/2^-$
253.1(3)	2.1(6)			2938	$(17/2^-)$	$17/2^-$
254.0(5)	1.2(2)	0.6(3)				
254.5(1)	1.9(3)		M1	3258	$19/2^-$	$19/2^-$
288.7(1)	0.9(2)			2654	$(11/2^+)$	$(7/2^+)$
289.7(1)	5.9(3)	1.34(13)	E2	3509	$21/2^+$	$17/2^+$
292.0(2)	0.5(2)			3205	$(15/2^+)$	$(13/2^+)$
292.5(1)	1.5(2)			4131		$25/2^+$
299.1(1)	2.8(2)	0.84(10)	M1	7248	$(37/2^-)$	$(35/2^-)$
301.9(1)	4.4(3)	1.0(2)		4046	$23/2^-$	$(21/2^-)$
306.0(4)	0.8(2)			2653	$13/2^-$	$(11/2^-)$
306.5(2)	1.8(2)	0.70(19)		2654	$(11/2^+)$	$(11/2^-)$
318.5(1)	13.3(5)	1.20(6)	M1	3004	$19/2^-$	$17/2^-$
321.2(3)	0.4(2)			3526	$(17/2^+)$	$(15/2^+)$
326.8(2)	2.4(3)	0.58(10)				
329.7(1)	3.0(3)	1.3(2)	E2	3839	$25/2^+$	$21/2^+$
346.1(2)	1.0(5)			2938	$(17/2^-)$	$15/2^-$
357.2(2)	2.2(3)			3890		$19/2^+$
360.4(1)	5.9(4)	0.87(12)		3203	$17/2^-$	$15/2^-$
374.0(1)	5.4(3)	1.2(2)	M1	6949	$(35/2^-)$	$(33/2^-)$
375.2(2)	0.7(1)		E1	6286	(33/2)	$(31/2^+)$
382.3(2)	2.3(3)	0.7(2)				
407.3(5)	1.0(3)			3878	$21/2^-$	$19/2^-$
417.4(4)	0.9(3)			5748	$31/2^+$	$29/2^+$
426.5(2)	3.1(2)			3959	$(23/2^+)$	$19/2^+$

Table 4. continued

E_γ(keV)	$I_\gamma{}^a$	R ratio	Multip.	E_i(keV)	I_i	I_f
432.6(1)	74(2)	1.09(2)	M1	4272	$27/2^+$	$25/2^+$
435.0(1)	1.8(2)	1.05(20)	M1	7683	$(39/2^-)$	$(37/2^-)$
446.8(2)	2.1(2)			2654	$(11/2^+)$	$(7/2^+)$
450.3(1)	4.9(4)	0.59(16)	M1	3959	$(23/2^+)$	$21/2^-$
465.8(3)	1.0(2)			4131		$23/2^+$
475.4(1)	5.0(3)		E2	3318	$19/2^-$	$15/2^-$
476.9(2)	2.1(2)			5911	$(31/2^+)$	$29/2^+$
486.1(1)	11.0(7)	1.2(3)	M1	3744	$(21/2^-)$	$19/2^-$
489.1(1)	8.8(5)	0.95(10)		986	$5/2^+$	$3/2^+$
490.0(1)	8.2(8)	1.5(2)		3533	$19/2^+$	$15/2^+$
493.1(3)	1.5(2)	1.0(2)				
496.1(2)	4.6(5)	1.4(2)		2843	$15/2^-$	$(11/2^-)$
497.3(1)	5.9(5)	1.11(10)	M1	497	$3/2^+$	$1/2^+$
498.3(3)	2.3(2)	1.5(3)		2654	$(11/2^+)$	$(7/2^+)$
505.6(1)	230(7)	0.83(1)	E1	3509	$21/2^+$	$19/2^-$
529.1(2)	3.5(5)			3533	$19/2^+$	$19/2^-$
529.3(1)	6.3(4)	1.4(2)		7248	$(37/2^-)$	$(35/2^-)$
537.7(1)	1.6(2)		E1	6286	(33/2)	$31/2^+$
549.8(2)	2.4(3)			6461		$(31/2^+)$
550.1(1)	15.1(4)	1.38(13)		3203	$17/2^-$	$13/2^-$
550.9(1)	18.0(4)	1.33(12)		3205	$(15/2^+)$	$(11/2^+)$
559.4(3)	1.7(3)	2.2(3)		3203	$17/2^-$	$15/2^-$
560.6(1)	7.9(7)	0.8(2)	M1	3878	$21/2^-$	$19/2^-$
561.1(3)	1.6(4)	0.9(3)		2347	$(11/2^-)$	$(9/2^-)$
570.0(3)	1.5(2)			2654	$(11/2^+)$	$(9/2^+)$
573.3(1)	13.5(10)	0.9(2)	M1	3258	$19/2^-$	$17/2^-$
574.3(1)	10.8(7)	1.20(12)	E2	3959	$(23/2^+)$	$(19/2^+)$
574.4(4)	1.3(4)		E2	4046	$23/2^-$	$19/2^-$
576.6(5)	1.8(5)			3533	$(19/2^+)$	$(15/2^+,17/2^-)$
580.1(2)	2.2(2)	1.5(3)		5911	$(31/2^+)$	$29/2^+$
588.2(1)	5.2(4)		E2	4059	$23/2^-$	$19/2^-$
595.5(3)	2.3(4)			3533	$19/2^+$	$(17/2^-)$
613.4(1)	6.4(9)	1.3(3)		3526	$(17/2^+)$	$(13/2^+)$
622.2(3)	3.4(4)			4131		$21/2^+$
626.0(5)	0.7(2)					
627.7(2)	4.5(4)	<0.8		4687	$25/2^-$	$23/2^-$
628.2(2)	5.8(5)	1.2(3)		2653	$13/2^-$	$15/2^-$
628.5(1)	4.1(4)		E2	3471	$19/2^-$	$15/2^-$
644.3(1)	4.0(4)		M1	4029		$(19/2^+)$
654.5(1)	16.1(4)	1.45(10)		3859	$(19/2^+)$	$(15/2^+)$
660.0(1)	27.9(14)	1.4(2)	M1	2685	$17/2^-$	$15/2^-$

Table 4. continued

E_γ(keV)	I_γ^a	R ratio	Multip.	E_i(keV)	I_i	I_f
674.4(2)	3.0(5)			3318	$19/2^-$	$15/2^-$
675.4(1)	24.6(11)	1.50(12)		3878	$21/2^-$	$17/2^-$
682.9(2)	1.3(3)			3526	$(17/2^+)$	$15/2^-$
700.1(1)	24.6(12)	0.92(14)		3385	$(19/2^+)$	$17/2^-$
704.0(2)	1.3(3)			2347	$(11/2^-)$	$(7/2^-)$
716.7(1)	7.2(8)	1.3(2)		4244	$(21/2^+)$	$(17/2^+)$
726.1(3)	2.9(3)			3533	$19/2^+$	$(15/2^+,17/2^-)$
726.0(5)	2.0(5)			3318	$19/2^-$	$15/2^-$
728.7(1)	9.5(8)	1.4(2)	E2	4046	$23/2^-$	$19/2^-$
739.4(1)	45(2)	1.43(10)	E2	2685	$17/2^-$	$13/2^-$
741.6(1)	79(3)	1.44(10)	E2	4059	$23/2^-$	$19/2^-$
746.0(2)	3.8(4)			4131		$19/2^+$
751.9(1)	13.8(5)	1.40(11)		4611	$(23/2^+)$	$(19/2^+)$
762.8(3)	0.7(2)		M1	6575	$(33/2^-)$	$31/2^-$
765.5(1)	3.8(3)		M1	6575	$(33/2^-)$	$31/2^-$
801.4(2)	3.7(4)			4059	$23/2^-$	$19/2^-$
805.8(1)	40(2)	1.42(10)	E2	4865	$27/2^-$	$23/2^-$
806.4(4)	1.5(3)			3744	$(21/2^-)$	$(17/2^-)$
808.6(1)	6.2(4)	1.4(2)		5420	$(27/2^+)$	$(23/2^+)$
808.7(1)	21.0(10)	1.32(14)	E2	4687	$25/2^-$	$21/2^-$
817.8(1)	14.3(14)	1.5(3)	M1	2843	$15/2^-$	$15/2^-$
818.0(1)	6.3(5)	1.5(3)		5061	$(25/2^+)$	$(21/2^+)$
818.6(3)	2.2(5)		E2	4865	$27/2^-$	$23/2^-$
828.9(1)	44(2)	1.27(9)	E2	4888	$27/2^-$	$23/2^-$
842.2(2)	4.6(5)		E2	4888	$27/2^-$	$23/2^-$
847.1(2)	2.0(3)	1.4(3)		5458	$(27/2^+)$	$(23/2^+)$
850.7(2)	2.8(2)	1.4(2)		6270	$(31/2^+)$	$(27/2^+)$
852.2(2)	2.1(3)		E2	6286	(33/2)	$29/2^+$
862.4(2)	8.6(10)			2807	$(15/2^+,17/2^-)$	$13/2^-$
867.4(1)	10.8(11)	1.4(3)		2653	$13/2^-$	$(9/2^-)$
888.6(3)	1.3(2)			7159	$(35/2^+)$	$(31/2^+)$
897.7(3)	3.1(5)			2843	$15/2^-$	$13/2^-$
986.5(3)	2.0(6)			986	$5/2^+$	$1/2^+$
992.2(2)	4.9(9)			2938	$(17/2^-)$	$13/2^-$
1006(1)	0.6(2)			8165	$(39/2^+)$	$(35/2^+)$
1017.8(1)	8.0(6)	1.4(3)	E2	6830	$35/2^-$	$31/2^-$
1020.3(4)	1.7(6)			6830	$35/2^-$	$31/2^-$
1026.4(1)	0.8(4)		E1	6356	$(31/2^-)$	$29/2^+$
1026.4(1)	6.3(5)		E1	4865	$27/2^-$	$25/2^+$
1043.4(2)	8.0(9)	1.6(5)	E2	4046	$23/2^-$	$19/2^-$
1046.6(2)	10.6(10)	1.5(2)		3043	$15/2^+$	$11/2^+$
1055.7(2)	3.2(4)			6684	$33/2^-$	$29/2^-$
1055.9(1)	17.3(9)	1.6(2)	E2	4059	$23/2^-$	$19/2^-$

Table 4. continued

E_γ(keV)	I_γ^a	R ratio	Multip.	E_i(keV)	I_i	I_f
1058.3(1)	4.8(3)	1.0(2)	M1	5330	$29/2^+$	$27/2^+$
1071.4(2)	3.6(4)			5031		$(23/2^+)$
1072.2(1)	10.0(10)	1.3(2)		1786	$(9/2^-)$	$11/2^-$
1092.0(2)	2.6(3)		E2	7922	$(39/2^-)$	$35/2^-$
1097.5(4)	0.7(3)			2084	$(9/2^+)$	$5/2^+$
1136.5(6)	0.8(2)		E2	6949	$(35/2^-)$	$31/2^-$
1140(1)	0.2(2)		E2	6949	$(35/2^-)$	$31/2^-$
1141(1)	0.3(2)			7825	$(37/2^-)$	$33/2^-$
1147(1)	0.3(2)			9069	$(43/2^-)$	$(39/2^-)$
1161.8(3)	1.2(2)		M1	5434	$29/2^+$	$27/2^+$
1169.4(5)	0.7(2)			2156	$(7/2^+)$	$5/2^+$
1178.3(1)	8.3(9)	0.85(14)		3203	$17/2^-$	$15/2^-$
1194.5(1)	18(2)	0.8(2)	E1	3219	$17/2^+$	$15/2^-$
1221.1(2)	1.6(4)			2207	$(7/2^+)$	$5/2^+$
1232.2(1)	46(2)	0.91(12)	M1	1945	$13/2^-$	$11/2^-$
1233.2(1)	20.0(2)	1.3(2)	E2	3258	$19/2^-$	$15/2^-$
1253.4(2)	3.3(3)			5092		$25/2^+$
1257.8(2)	3.2(4)			3203	$17/2^-$	$13/2^-$
1293.2(1)	100(5)	1.51(4)	E2	3318	$19/2^-$	$15/2^-$
1311.7(1)	490(4)	1.49(2)	E2	2025	$15/2^-$	$11/2^-$
1327.5(1)	3.7(3)	1.0(2)	M1	5599	(29/2)	$27/2^+$
1360.6(2)	2.4(4)			1858	$7/2^+$	$3/2^+$
1379.0(4)	0.7(2)			2365	$(7/2^+)$	$5/2^+$
1383.8(1)	11.6(11)	1.4(2)		1996	$11/2^+$	$7/2^+$
1387.6(1)	3.6(3)	0.9(2)	M1	5659	(29/2)	$27/2^+$
1446.8(2)	8.7(11)	1.5(2)	E2	3471	$19/2^-$	$15/2^-$
1454.0(3)	0.6(2)			2440	$(7/2^+)$	$5/2^+$
1471(1)	0.5(2)			2084	$(9/2^+)$	$7/2^+$
1476.7(1)	17.0(7)	1.45(6)	E2	5748	$31/2^+$	$27/2^+$
1491.5(1)	11.0(5)	1.29(6)	E2	5330	$29/2^+$	$25/2^+$
1543.7(3)	0.5(2)			2156	$(7/2^+)$	$7/2^+$
1559.1(2)	3.2(3)	1.1(3)	E2	5225		$23/2^+$
1595.0(1)	10.7(5)	1.34(6)	E2	5434	$29/2^+$	$25/2^+$
1595.3(6)	0.5(2)			2207	$(7/2^+)$	$7/2^+$
1634.0(2)	3.6(4)	1.1(2)		2347	$(11/2^-)$	$11/2^-$
1639.4(1)	2.7(2)	1.7(2)	E2	5911	$(31/2^+)$	$27/2^+$
1659.1(2)	1.0(3)			2156	$(7/2^+)$	$3/2^+$
1752(1)	0.3(2)			2365	$(7/2^+)$	$7/2^+$
1801.3(4)	1.4(2)			6072		$27/2^+$
1868(1)	0.3(2)			2365	$(7/2^+)$	$3/2^+$
1940.0(2)	5(1)			2653	$13/2^-$	$11/2^-$
1940.9(2)	7(1)	1.2(2)		2654	$(11/2^+)$	$11/2^-$
2200(1)	3(1)			2913	$(13/2^+)$	$11/2^-$

^{a} *Intensities from the* ^{104}*Ru(*^{18}*O,*α*3n) reaction at 65 MeV.*

The higher spin value is much more likely on the basis of feeding arguments. The 3959 keV state is also depopulated via the 426, 490, 1047 and 1384 keV cascade transitions to the 613 keV isomeric state. The three latter transitions have R ratios typical of the stretched E2 transitions. The assignment of $I = 23/2$ for the 3959 keV state results in $\Delta I = 2$ character for the 426 keV transition, and consequently positive parity for this state. Therefore, the 3385 keV $I = 19/2$ state, fed by the 574 keV E2 transition from the 3959 keV state, has positive parity. The peak observed at 1232 keV in the total projection spectrum is determined to be a doublet, since a 1233 keV transition is observed in coincidence with the 1312 keV yrast transition. Also, the observation of a 801 keV transition depopulating the 4059 keV $23/2^-$ state establishes a level at 3258 keV and fixes its spin and parity to $19/2^-$. This state is also connected by transitions to the 2685, 3004 and 3509 keV levels. For the 3744 keV level identified in this work, definite spin and parity assignment could not be made. States at 2592 and 2807 keV were also identified in the previous study [Vis91] with a tentative $I^\pi = 15/2^-$ assignment for the former state. The 726 keV branch from the 3318 keV $19/2^-$ state confirms this assignment.

Several states feeding the yrast $23/2^+$, $25/2^+$ and $27/2^+$ states with transitions having energies exceeding 1 MeV were identified. Since many of these transitions are of stretched quadrupole type, they are depopulating positive parity states.

To the left of the low-spin yrast sequence, five groups of levels are shown, where states are connected by E2 transitions. An intense E2 transition of 1293 keV energy was observed to populate the yrast $15/2^-$ state, establishing a $19/2^-$ state at 3318 keV. On top of this state, a regular sequence of states connected by E2 transitions (band 4) was established up to the $(43/2^-)$ state, thereby confirming the recent observation in Ref.[Se97]. A coincidence spectrum gated on the 742 keV transition feeding the 3318 keV state is presented in Fig. 29a, showing the transitions placed in band 4, except the uppermost transition which is only seen in the thin-target data. There are also several other intense transitions present in this spectrum. These transitions are mostly due to a sequence of states labelled S in Fig. 28. This group of levels starts from a level at 2843 keV and extends up to a $(39/2^-)$ state at 7683 keV. The angular distribution ratios for the intense 729, 806, 909, 921 and 944 keV transitions indicate that they have a stretched quadrupole character. Links with band 4 and the yrast states determine the spin and parity of the 2843, 3471 and 4046 keV levels to $15/2^-$, $19/2^-$ and $23/2^-$, respectively.

Another regular band, band 3, consisting of six transitions, is built on the 2653 keV $13/2^-$ state. In Fig. 29b a spectrum gated on the 675 keV transition is presented and clearly shows the transitions in band 3. This negative parity band is connected by dipole transitions to band 4 as well as to the yrast $11/2^-$ and $15/2^-$ states and by the 1258 keV $\Delta I = 2$ transition to the 1945 keV $13/2^-$ state.

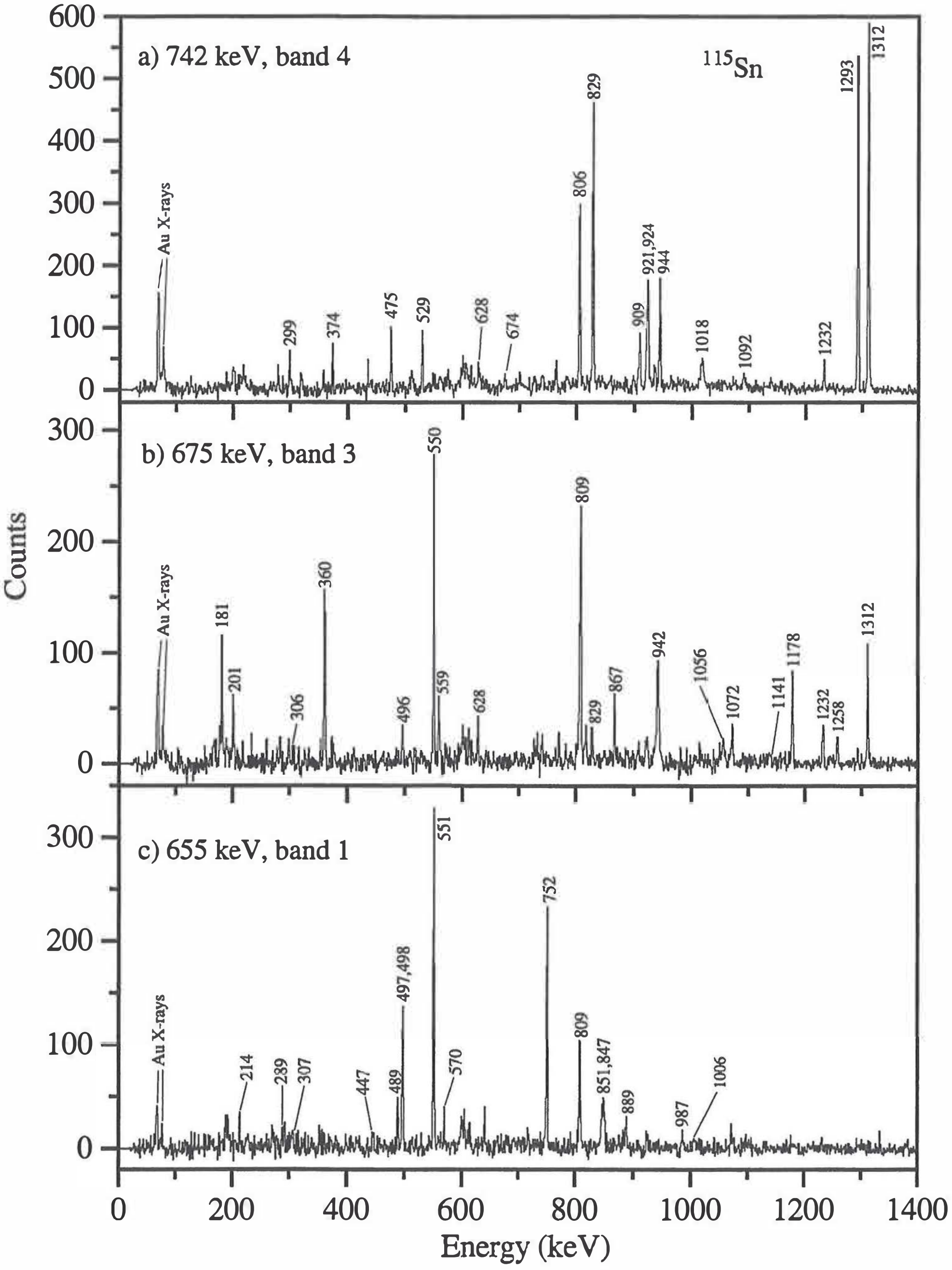

Figure 29. Sample γ-γ coincidence spectra for ^{115}Sn following the ^{104}Ru(^{18}O,α3n) reaction at 65 MeV bombarding energy. The spectra are extracted from the α-gated matrix with the γ gates set on the a) 742 keV, b) 675 keV and c) 655 keV transition.

A γ-ray cascade of 551, 655, 752, 809, 851, 889 and 1006 keV transitions was observed in both the ^{18}O + ^{104}Ru and ^{18}O + ^{100}Mo experiments. In the former reaction this cascade is seen in coincidence with α particles, while in the latter experiment it is populated via a xn channel. This indicated that this relatively strongly populated rotational band belongs to ^{115}Sn, although as it is seen in Fig. 29c, it is not in coincidence with any known intense transition in this nucleus. However, rather weak 497 and 489 keV transitions are present in this spectrum. These transitions between the low-lying low-spin states have previously been observed following light-ion induced reactions [ToI]. A careful investigation of the data revealed that the intensity from this band flows down to the ground state via a group of states between 2084 and 2440 keV, which had also been observed in various light-ion reactions, ref. [ToI] and references therein. Note, that the 2654 keV and 3205 keV states in band 1 are very close in energy to two lowest states in band 3. From the coincidence relations it is clear that we observe two near degenerate states at both of these energies.

It is difficult to make spin/parity assignments for band 1 due to the doublet character of the 551 and 1941 keV transitions, and due to the weakness of the other depopulating transitions. The 2654 keV state in band 1 we tentatively assign with $I^{\pi}= 11/2^{+}$ based on the decay properties and feeding arguments. An R ratio of 1.2(2) was obtained for the 1940/1941 keV doublet from the spectra gated on the 550 and 551 keV transitions, as well as from the total projections. This is consistent with the $11/2^{+}$ assignment for the 2654 keV state.

A γ-ray cascade consisting of the 613, 717, 818 and 905 keV transitions was also observed in both of our experiments. They were seen in coincidence with the α particles in the ^{18}O + ^{104}Ru experiment, whereas in the ^{18}O + ^{100}Mo experiment they are not in coincidence with charged particles, which most likely indicates that this cascade belongs to ^{115}Sn. A 2200 keV γ-ray was observed in coincidence with these transitions. Furthermore, weak 292 and 321 keV transitions may connect this cascade to band 1, as well as a 683 keV transition to the 2843 keV ($15/2^{-}$) state. This fixes the lowest state of band 2 to lie at 2913 keV.

Finally, both backed target data sets show evidence for a γ-ray cascade, band 5, consisting of five transitions. The 327, 382 and 493 keV transitions have R ratios typical for $\Delta I = 1$ dipole transitions, while the 254 and 626 keV transitions are too weak to measure the R ratio. The observed five transitions may form the beginning of a dipole band. This band is de-excited by unobserved transitions to the 5330, 5434, 5659 and 5748 keV levels. Based on the decay pattern and feeding arguments, we estimate that the band head spin is ≈ 33/2.

5.4 Discussion

The observed level structures in ^{115}Sn and ^{116}Sn can be divided into two groups, rotational bands and spherical states. These groups will be discussed separately below. Section 5.4.1 is concerned with the deformed structures, discussing the properties of the observed bands. In section 5.4.2 the spherical states are discussed.

5.4.1 Properties of the observed bands

Configuration assignments and alignments

Our experiments on ^{115}Sn and ^{116}Sn have provided new evidence for deformed structures in these nuclei. The alignment behaviour of the observed bands, revealed by plotting the aligned angular momentum as a function of rotational frequency, is shown in Fig. 30. The reference we have used to describe the energy of the rotating core is given by the Harris parameters of $J_0 = 15\hbar^2/\text{MeV}$ and $J_1 = 25\hbar^4/\text{MeV}^3$, which are adopted from the neighbouring *I* and Xe nuclei [Tor94,Tor97].

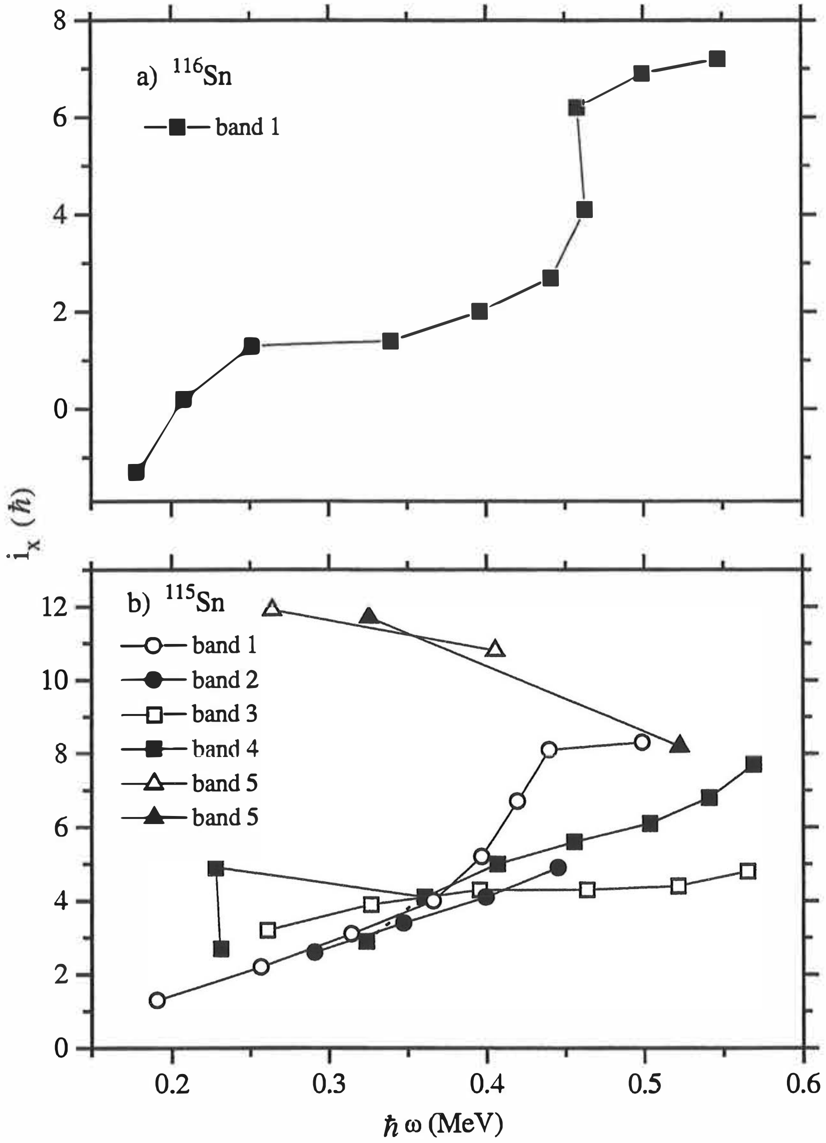

Figure 30. Aligned angular momenta for the rotational bands in ^{115}Sn and ^{116}Sn. A reference configuration with parameters $J_0 = 15\hbar^2/MeV$ and $J_1 = 25\hbar^4/MeV^3$ has been subtracted.

As observed in ref.[Ka79] the intruder structures at low spin are mixed with the normal spherical structures and therefore the intruder band in ^{116}Sn is not as well-developed at low energies as it is at higher spin, where it does not show any connection to the normal states.

In the alignment plot of Fig. 30a, this mixing manifests itself as an irregularity at low rotational frequencies. The strength of the 641 keV transition from the 6^+ state of the intruder band to the yrast 4^+ state may be taken as an evidence for substantial mixing of the two lowest 4^+ states. The 0^+ band head of the intruder band is also mixed with another 0^+ state, as discussed in ref [Ka79]. The mixing of vibrational and deformed states will be further discussed below.

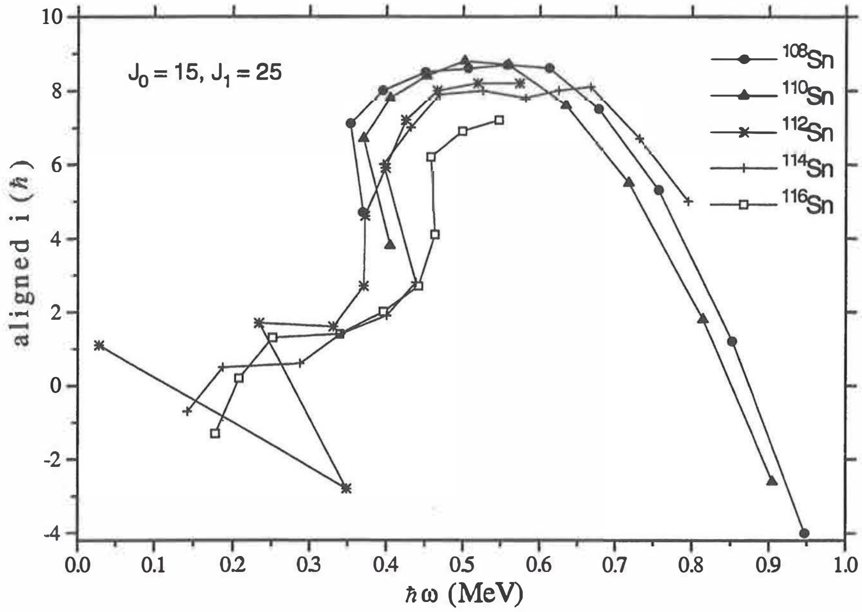

Figure 31. Aligned angular momenta of the intruder bands for even Sn isotopes. A reference configuration with Harris parameters $J_0 = 15\hbar^2/MeV$ and $J_1 = 25\hbar^4/MeV^3$ has been subtracted.

In Fig. 31 alignment behaviour of the intruder bands in even Sn nuclei is presented. In the lighter Sn nuclei the low spin members have not been observed. This is likely to be due to the higher excitation energy causing a strong mixing of intruder band states with other states at lower spins. A gain of about $5\hbar$ in the alignment of the intruder band in ^{116}Sn takes place at $\hbar\omega = 0.46$ MeV. The first alignment in this mass region is expected to be due to the $h_{11/2}$ neutrons. In ^{114}Sn and ^{112}Sn the alignment is observed at the frequency of 0.41 MeV and 0.37 MeV, respectively [Ha89]. This increase in the neutron alignment frequency when approaching $N = 66$ can be associated, at least partly, with shell effects and increased collectivity at the neutron midshell. At higher rotational frequencies a soft band termination takes place. As the band proceeds to termination the nuclear shape gradually shifts from a collective prolate to a noncollective oblate shape.

An interesting problem in light Sn isotopes is the nature of the 10^+ states fed in the decay of the collective bands. In ^{112}Sn two 10^+ and 12^+ levels are fed in the decay of the collective band [Ha88]. The lower one of the 10^+ states is identified with the neutron $\nu h^2_{11/2}$ 10^+ state observed in all of the heavier Sn isotopes. In ^{110}Sn only one 10^+ state is observed to be fed from the 12^+ member of the collective band. On the basis of de-excitation properties of this 10^+ state, Viggers et al. [Vi87] identify it with the neutron $h^2_{11/2}$ configuration. Furthermore, they conclude that in addition to $h_{11/2}$ neutrons no proton 2p-2h excitations are needed to generate this band in ^{110}Sn. The observed feeding of the 10^+ states reveals that these states are mixed. More information about the role of $h_{11/2}$ neutrons might be obtained from Fig. 32, where energy systematics of the observed collective bands together with the first excited 2^+ states are presented. An interesting change in the excitation energy behaviour of the intruder bands is observed with the decreasing neutron number. In light isotopes the energy pattern seems to follow the energy of the suggested $\nu h^2_{11/2}$ 10^+ states. This energy trend may indicate that $h_{11/2}$ neutrons play an important role in generating the collective band of light Sn nuclei, giving some support to the suggestion of Viggars et al. [Vi87].

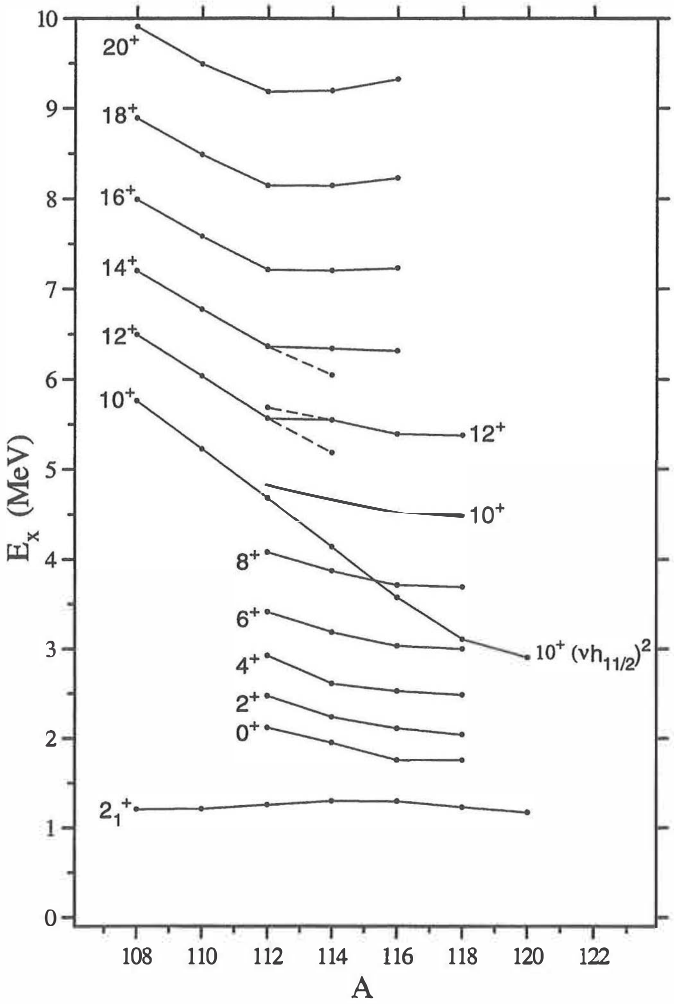

Figure 32. Energy systematics of the observed collective bands in even Sn nuclei. The energies of the 2_1^+ states and the neutron $h_{11/2}^2$ 10^+ states are also shown.

At a deformation of $\beta_2 \approx 0.2$, expected for the proton 2p-2h intruder configuration, the Fermi surface for $N = 65$ lies close to the $\Omega = 5/2$ states originating from the spherical $d_{5/2}$, $g_{7/2}$ and $h_{11/2}$ states. Bands 3 and 4 in ^{115}Sn, being negative parity, can be assigned to the unfavoured and favoured signatures of the neutron $h_{11/2}$ configuration. It is worth noticing that bands 3 and 4 are connected by dipole transitions up to $I = 31/2$. The extracted alignments in Fig. 30b support the neutron $h_{11/2}$ assignment. Band 4 strongly feeds the yrast $15/2^-$ state via the 1293 keV E2 transition, similar to ^{114}Sn, where a strong 1315 keV transition de-excites the 4^+ intruder band state to the yrast 2^+ state.

Below the $19/2^-$ member in band 4, the identification of states as band members is less clear since E2 branches are observed to the 2643, 2843 and 2592 keV $15/2^-$ states. Similarly, the first two of these states are fed from the $17/2^-$ state of band 3, which is the unfavoured signature partner of band 4. Based on B(E2) arguments, the 2843 keV level is assigned as a member of band 4. The $15/2^-$ and $19/2^-$ states of band 4 thus appear to be mixed with the other near-lying states. The 2347 keV ($11/2^-$) state could be the band head of band 4, but it may also belong to the $h_{11/2} \otimes 2^+$ multiplet. Also at higher spins, members of band 4 mix with other states. The $23/2^-$, $27/2^-$ and $31/2^-$ states in the level structure S lie only 3 - 23 keV apart from the members of band 4 having the same spin value. The mixing of these states with the members of band 4 is revealed by the observation of many linking transitions. However, band 4 is not much disturbed by this mixing since the interaction energies must be very small as indicated by the small level energy separations, see below for the interpretation of those states.

Band 3 in ^{115}Sn is not disturbed by mixing like band 4 near the band head and in the alignment plot of Fig. 30b it shows a rather constant alignment for a wide frequency range. The favoured signature of the neutron $h_{11/2}$ configuration, on the other hand, shows a small gradual alignment gain at $\hbar\omega \approx 0.4$ MeV. There is some evidence for alignment gains in both bands above the frequency of $\hbar\omega = 0.5$ MeV. A recent lifetime measurement [Lob97] using the (α,2n) reaction yields transition rates of 109.7(36.6) and < 55 W.u for the 675 keV (band 3) and 742 keV (band 4) transitions, respectively, suggesting that band 3 might be more collective than band 4.

The properties of bands 1 and 2 are best accounted for by the neutron $g_{7/2}$ configuration. Both the initial alignment and the absence of signature splitting, as well as the weakness of the, interconnecting dipole transitions point to this direction. In band 1, a gain in the alignment is observed at $\hbar\omega \approx 0.42$ MeV. This gain is presumably due to the $h_{11/2}$ neutrons, which are expected to be responsible for the first alignment in this mass region. The alignment takes place somewhat earlier than in the intruder band in ^{116}Sn, whereas the alignment gains are similar.

Bands characterized by intense dipole transitions have been observed in Sb, Te, I and Xe nuclei [Tor94,Tor97,LaF97,Ju98]. Common to these bands is that their configurations involve a proton 1p-1h excitation where a hole is on the upsloping proton $g_{9/2}$ orbital and the particle on one of the downsloping orbitals above the $Z = 50$ gap. A rotational band, with its 5^- band head at 4047 keV excitation energy and built on the $\pi g_{9/2}^{-1} h_{11/2}$ configuration, has been observed in ^{114}Sn [Sch92]. The corresponding band is not observed in ^{116}Sn, but the excitation energies of the stretched spin $\pi g_{9/2}^{-1} g_{7/2}$ and $\pi g_{9/2}^{-1} h_{11/2}$ states in ^{116}Sn are known from light-ion transfer reactions to be ≈ 4 MeV and ≈ 5.5 MeV [We86]. The observed small transfer strengths are consistent with the idea that these proton states are deformed. The strongly coupled band, band 5, in ^{115}Sn may be due to coupling of one or three quasineutrons with either one of these proton 1p-1h states.

The alignment curve for band 5 is included in Fig. 30. The extracted aligned angular momentum is large (assuming $I = 33/2$ for the lowest state in the band) and therefore the configuration must involve both $h_{11/2}$ protons and neutrons. The configuration $\pi g_{9/2}^{-1} h_{11/2} \nu h_{11/2}$ can roughly account for the observed aligned angular momentum. However, the configuration assignment must wait for the definite spin and parity determinations.

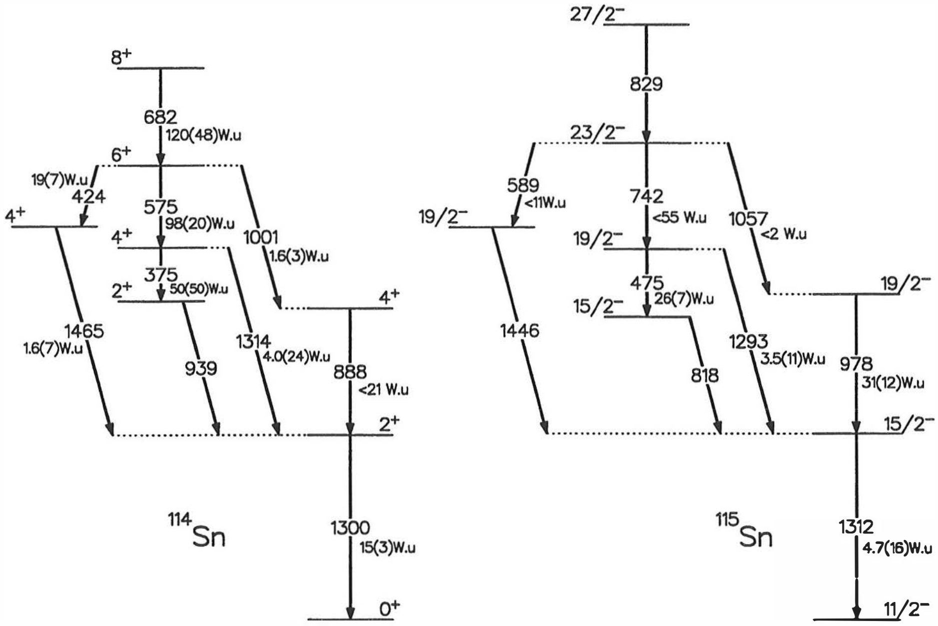

Figure 33. Comparison of ^{115}Sn and ^{114}Sn. The B(E2) values are from refs. [Lob97, Vi91]

The low spin decay properties of ^{114}Sn and ^{115}Sn are compared in Fig. 33. Both the decay patterns and the energies of transitions connecting deformed and spherical states are surprisingly similar, indicating that the $h_{11/2}$ neutron acts mainly as a spectator and hence, does not contribute much to the low-spin excitations. The situation changes with increasing angular momentum.

Comparison with neighbouring nuclei

According to the simple intruder picture, bands with the same boson number should be similar [He92]. Therefore, it is interesting to compare the 2p-2h bands with 4p bands, i.e. compare the intruder bands in Sn nuclei with band structures in the Xe isotones. In Fig. 34, a comparison is made in terms of experimental routhians for the odd-mass nuclei and in terms of moment of inertia J_2 for the even-mass nuclei. In ^{115}Sn and ^{119}Xe, we not only observe the same bands, but also relative energy spacings are almost identical. In the even-mass Sn and Xe nuclei the moment of inertia is quite the same apart from the band crossing region. These observations clearly suggest that deformation is similar in the rotational bands in Sn and Xe nuclei.

One should also note that the band crossings in ^{118}Xe and ^{120}Xe have a different origin than in the Sn nuclei. In these Xe nuclei, the proton Fermi surface has moved closer to the proton $h_{11/2}$ orbital, and therefore the first band crossing in the ground-state band involves both the proton and neutron $h_{11/2}^2$ alignments [Tor94], while the band crossing in ^{114}Sn and ^{116}Sn is due to the $h_{11/2}$ neutrons. In ^{118}Xe and ^{120}Xe positive parity bands assigned with the neutron $h_{11/2}^2$ configuration have been identified [Tor94]. These bands cross the ground-state band at $\hbar\omega \approx 0.42$ MeV, which is close to the crossing frequencies in the Sn isotones.

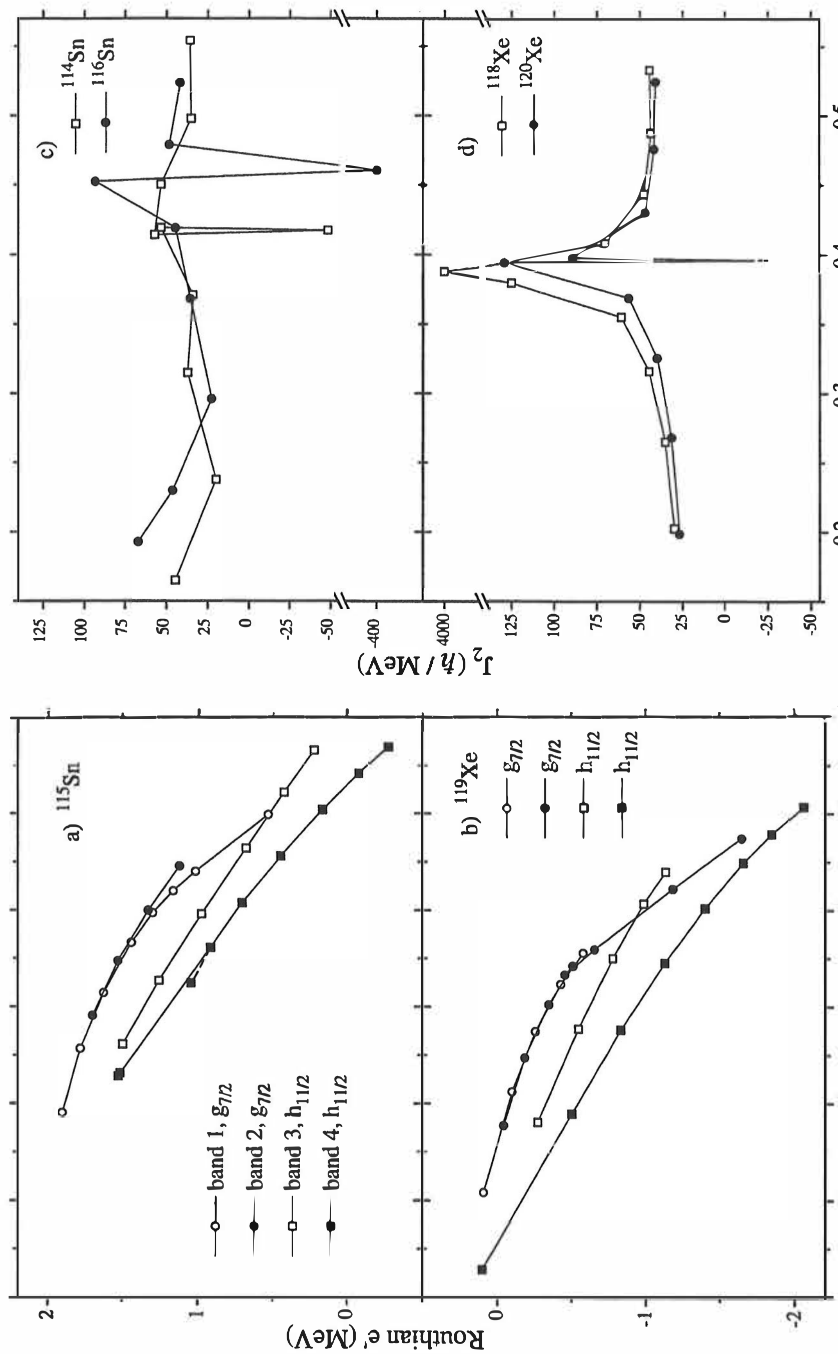

Figure 34. Routhians for the rotational bands in a) ^{115}Sn, b) ^{119}Xe [Ja89] , c) ^{116}Sn and d) ^{120}Xe [Tor94] . A reference configuration with parameters $J_0 = 15\hbar^2/MeV$ and $J_1 = 25\hbar^4/MeV^3$ has been subtracted. In a) and b) open and closed symbols correspond to the $\alpha = 1/2$ and $\alpha = -1/2$ signatures, respectively.

However, there are small differences in the signature splittings and alignment gains. Particularly, the signature splitting between the two signatures of the neutron $h_{11/2}$ configuration is smaller in ^{115}Sn than in ^{119}Xe. In the cranked shell model calculations performed at $\beta_2 \approx 0.23$, this energy splitting decreases when quadrupole deformation increases or the γ deformation goes from negative values to $\gamma = 0°$. Thus, the observed difference in the signature splitting can be interpreted as being due to a change in the deformation.

Quenching of the intruder-to-yrast $4^+ \to 2^+$ transition

The large relative B(E2) for the 641 keV $6^+ \to 4^+$ transition in ^{116}Sn most likely indicates a substantial mixing of the two lowest 4^+ states. The transition from the 4^+ state of the intruder band to the yrast 2^+ state in ^{116}Sn was too weak to be observed in the present experiment. In earlier experiments, its B(E2) has been determined to be less than 0.003 W.u. [Ka79]. On the contrary, the corresponding transition in ^{114}Sn is much faster with B(E2) = 4.0(24) W.u. [Lob97]. This has been interpreted as an indication of a change in the mixing of the 4^+ states [Br79].

In order to get some insight into the mixing of the low-spin yrast and intruder band states, we have performed calculations where the 2^+ and 4^+ states were allowed to mix. The calculations were done both for ^{116}Sn and ^{114}Sn to see, if the mixing of these states can account for the observed differences in the B(E2) values. In both nuclei, the mixing amplitudes for the yrast and intruder band 4^+ states were obtained from the ratio of the B(E2) values for the $6^+ \to 4^+$ transitions. Values of 0.78 and 0.63, and 0.92 and 0.13 were derived for ^{116}Sn and ^{114}Sn, respectively. The interaction energies are 68 keV and 53 keV, respectively. The mixing of the 2^+ states in ^{116}Sn was calculated by requiring that the $4^+ \to 2^+$ transition is totally quenched due to different signs of the two terms in the transition matrix element. A value of B(E2) = 120 W.u. was used for the unmixed intruder band $4^+ \to 2^+$ transition, whereas the B(E2) value for the same transition between vibrational yrast states was varied around the value of about 25 W.u. expected for a pure harmonic vibrator. The values of the mixing amplitudes of the 2^+ states, as well as the interaction energies, depend on the B(E2) values between unmixed states. The interaction energy increases smoothly from about 180 keV to 310 keV when the assumed B(E2) value for the yrast $4^+ \rightarrow 2^+$ transition goes from 10 W.u to 40 W.u. In the calculation of the mixing of the 2^+ states in ^{114}Sn, the interaction energy was assumed to be the same as in ^{116}Sn.

The calculated mixing amplitudes of the 2^+ states and the B(E2) values for the $4^+ \rightarrow 2^+$ transitions are collected in Tables 5 and 6. As indicated by Table 6, the mixing calculation described above is able to account for the difference between ^{114}Sn and ^{116}Sn in the B(E2) value for the intruder-to-yrast $4^+ \rightarrow 2^+$ transition. However, due to the large error bars for the experimental values, it is difficult say which one of the assumed B(E2) values for the unperturbed yrast $4^+ \rightarrow 2^+$ transition is most appropriate. The lower interaction energy between the 4^+ states than between the 2^+ states may indicate, that the yrast 4^+ state is less of collective vibrational character.

Table 5.

Mixing amplitudes of the yrast and intruder band 2^+ states assuming 10, 20, 30 or 40 w.u rate for the unmixed yrast $4^+ \rightarrow 2^+$ transition. For the unmixed $4^+ \rightarrow 2^+$ transition in the intruder band a B(E2) of 120 W.u. was adopted, see text for the details.

Nucleus	10 W.u	20 W.u	30 W.u	40 W.u
^{116}Sn	0.974, 0.227	0.957, 0.290	0.928, 0.371	0.906, 0.423
^{114}Sn	0.981, 0.195	0.972, 0.235	0.954, 0.314	0.933, 0.360

Table 6.
B(E2) values (in W.u.) for $4^+ \rightarrow 2^+$ transitions between mixed yrast and intruder-band states, see text and Table 5 for the details. The rightmost column gives the experimental values [Ka79,Lob97,Vi91,Kai72]. Subscripts i and y denote for intruder and yrast, respectively.

Transition	10 W.u	20 W.u	30 W.u	40 W.u	exper.
^{116}Sn $4^+_i \rightarrow 2^+_i$	77	78	85	89	>17
^{116}Sn $4^+_y \rightarrow 2^+_y$	16	29	42	54	8(19)
^{116}Sn $4^+_y \rightarrow 2^+_i$	38	32	22	17	90(45)
^{114}Sn $4^+_i \rightarrow 2^+_y$	2.8	4.5	7.6	9.3	4.0(24)
^{114}Sn $4^+_y \rightarrow 2^+_y$	11	22	31	40	<21

5.4.2 Spherical states in ^{115}Sn and ^{116}Sn

The irregular parts of the level schemes of ^{115}Sn and ^{116}Sn consist of neutron-quasiparticle and collective core excitations. The low-lying 5^-, 7^-, 9^- and 10^+ states in even-mass Sn nuclei are interpreted to arise from the shell-model $h_{11/2}s_{1/2}$, $h_{11/2}d_{3/2}$, $h_{11/2}g_{7/2}$ and $h^2_{11/2}$ configurations, respectively. Other states can be obtained by using these known 2-quasiparticle states and 1-quasiparticle states in ^{115}Sn as building blocks.

The level energy spacings above the 9^- state in ^{116}Sn are similar to those of the collective $2^+{}_1$ and $4^+{}_1$ states and therefore we associate the 11^- and 13^- states with the maximally aligned $h_{11/2}g_{7/2} \otimes 2^+$ and $h_{11/2}g_{7/2} \otimes 4^+$ configurations. The configurations $h^3_{11/2}s_{1/2}$, $h^3_{11/2}d_{3/2}$ and $h^3_{11/2}g_{7/2}$ yield states with $I_{\max} = 14$, 15 and 17, respectively, presumably corresponding to the negative parity states observed at 6213, 6344 and 7082 keV in ^{116}Sn. The positive parity $I > 10$ states observed in the irregular part of the ^{116}Sn level scheme may emanate from the coupling of the $h^2_{11/2}$ 10^+ state with the collective yrast 2^+ and 4^+ states, or from pure shell-model neutron configurations of the type $h^2_{11/2}s_{1/2}d_{3/2}$, $h^2_{11/2}d^2_{3/2}$, $h^2_{11/2}s_{1/2}g_{7/2}$ and $h^2_{11/2}d_{3/2}g_{7/2}$. The neutron $h^4_{11/2}$ and $h^2_{11/2}g^2_{7/2}$ configurations are expected to give positive parity states with $I_{\max} = 16$ at about 7 MeV of excitation energy. These states were not observed in the present experiments.

The Microscopic quasiparticle-phonon model calculations for ^{115}Sn

One can try to interpret spherical states of the ^{115}Sn nucleus by the use of semimicroscopic or microscopic approaches. The quasiparticle-phonon coupling scheme is a convenient way of exploiting the information of even-even nuclei in studying nuclear-structure effects in odd-mass nuclei. This scheme makes use of the property of the BCS quasiparticles being the elementary excitations of an odd-mass nucleus and assumes that by coupling them to few lowest-energy (collective) excitations of the even-even reference nucleus one is able to describe, at least qualitatively, the spectroscopy of odd-mass nuclei. The microscopic quasiparticle-phonon model (MQPM) is introduced in Refs. [Toi95,Suh98].

The MQPM treats the structure of the odd-A nuclei in the following four steps. First, the neighbouring even-even nucleus, or nuclei (in this case ^{114}Sn) can be used to study the properties of the chosen mass region and to fix the possible free parameters of the model hamiltonian. In the present case we have used an adjusted Woods-Saxon potential (see e.g. Ref. [Toi95]) as the mean-field part. The proton and neutron pairing channels of the Bonn-A G-matrix are scaled by the use of semiempirical pairing gaps [Suh88]. Second, the pairing part of the problem is treated in the BCS approximation. As the third step, the two basic excitations, QRPA phonons and BCS quasiparticles, are coupled to form a wave function basis for a realistic treatment of the odd-A nucleus. As the last step, the residual hamiltonian, containing the interaction of the odd nucleon with the reference nucleus, is diagonalized in this non-orthogonal and over-complete basis, see Ref. [Suh98] for details.

In the present calculation, the single-particle basis includes both for protons and neutrons, all the orbitals between the particle numbers 28 and 82. For three-quasiparticle states in ^{115}Sn, we have used 2 - 8 lowest $I^{\pi} = 2^+, 3^-, 4^+, 5^-, 6^+, 7^-, 8^+, 9^-$ and 10^+ QRPA phonons. The phonon energies agree quite well with the level scheme of ^{114}Sn, except for the 7^- and 9^- phonons which are calculated to lie about 300 keV above the observed states.

A comparison of experimental and calculated spherical states in ^{115}Sn is displayed in Fig. 35. In this figure, only yrast states are shown. Above the one-quasiparticle states, the calculated level scheme shows states where a quasiparticle is coupled to the 2^+ and 4^+ phonons. At higher spins, there are usually at least two components of similar size in the wave function of 3-quasiparticle states, one with positive parity phonon, and one with negative parity phonon. Particularly for the positive parity, the calculated states tend to lie higher in energy than the observed states. For the high-spin states in Fig. 35 this is, at least partly, due to the too high energy of the 7^- and 9^- phonons.

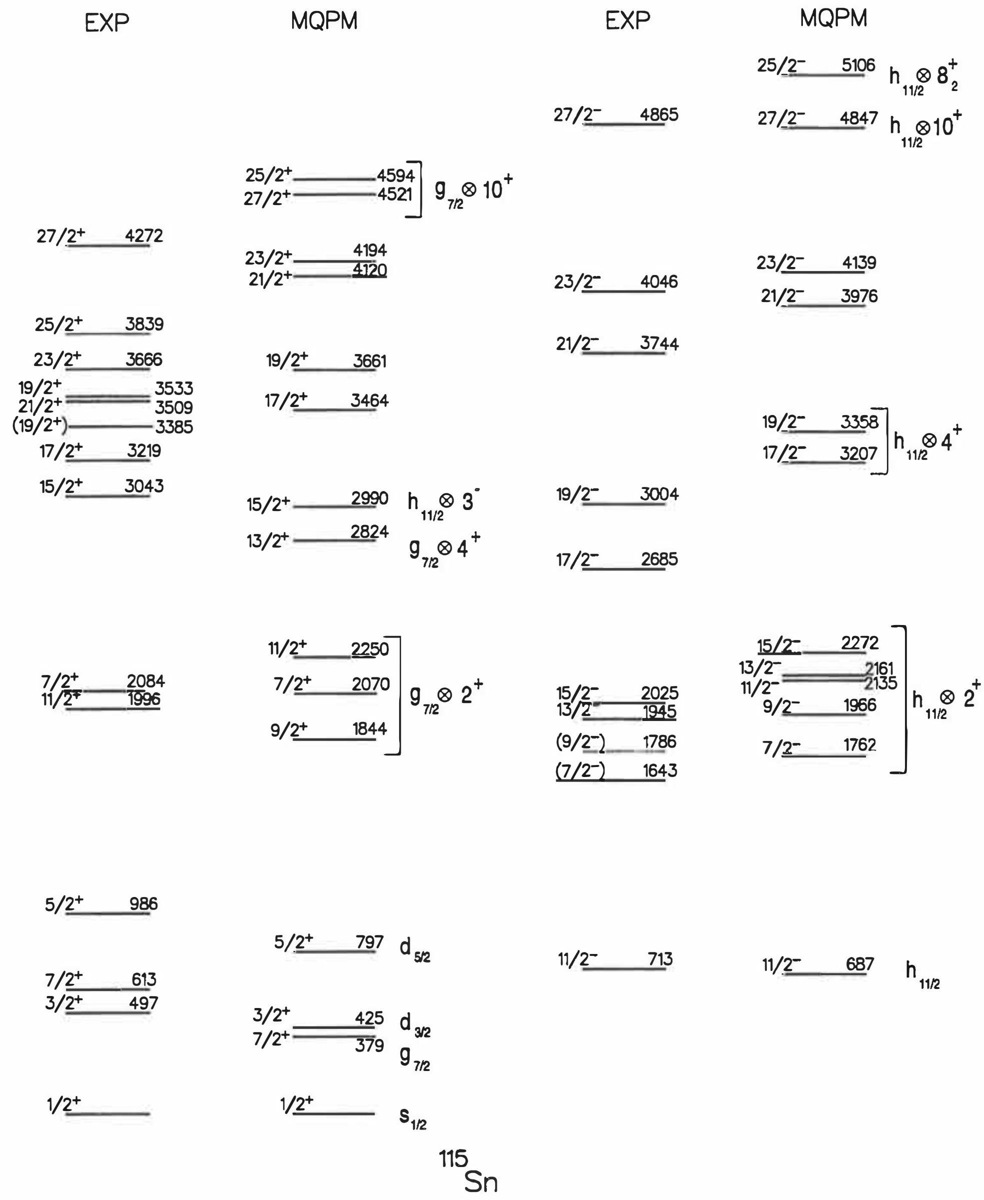

Figure 35. Comparison of experimental and calculated energies for spherical states in ^{115}Sn. A dominant configuration from the MQPM calculation, if any, is indicated.

The strongly populated yrast states in ^{115}Sn originate from the $h_{11/2}$ orbital coupled to the 0^+, 2^+ and 4^+ states in ^{114}Sn. In the $h_{11/2} \otimes 2^+$ multiplet we observe the $(9/2^-)$, $13/2^-$ and $15/2^-$ members at 1786, 1945 and 2025 keV, respectively. The 1643 keV state is most likely $7/2^-$, since the 930 keV transition to the 713 keV $11/2^-$ state is of E2 type [Ma75]. Thus we have identified all the other members of the $h_{11/2} \otimes 2^+$ multiplet, but the $11/2^-$ state. One might interpret the 2347 keV $(11/2^-)$ state as belonging to this multiplet. As pointed out earlier, this state may as well be the band head of band 4. The MQPM calculation reproduces both the centroid and the splitting of the $h_{11/2} \otimes 2^+$ multiplet rather well. The 2685 keV $17/2^-$ and 3004 keV $19/2^-$ states we interpret as the members of the $h_{11/2} \otimes 4^+$ multiplet. The energies of the lowest $21/2^-$, $23/2^-$ and $27/2^-$ states are nicely reproduced by the MQPM calculation. The lowest calculated $9/2^+$ and $11/2^+$ states arise from the $g_{7/2} \otimes 2^+$ multiplet. The $19/2^+$ state of $h^2_{11/2}s_{1/2}$ parentage in the heavier odd-mass Sn nuclei is isomeric due to M2/E3 decay to the $15/2^-$ state [Hash79,Ma94]. In ^{115}Sn this state is calculated to lie above the yrast $17/2^-$ and $19/2^-$ states. The 3385 keV $(19/2^+)$ state is a candidate for this configuration.

The states above the $27/2^-$ $\nu h^3_{11/2}$ and $27/2^+$ $\nu h^2_{11/2}g_{7/2}$ states may be due to coupling of these states with the low-lying phonon states. The maximum-spin state from the $\nu h^3_{11/2} \otimes 6^+$ configuration is that with $I_{\max} = 39/2$ which may correspond to the 7683 keV $(39/2^-)$ state. Regarding to the excitation energy and the decay pattern, the 5748 keV $31/2^+$ state could be a member of the $\nu h^2_{11/2}g_{7/2} \otimes 2^+$ multiplet.

Chapter 6

Summary

The present work demonstrates that arrays of modern Compton suppressed Ge detectors with moderately high detection efficiency for γ-rays, equipped with ancillary detectors enable a reaction channel selection and thus make spectroscopic studies of relatively neutron-rich nuclei lying near the β-stability line possible.

It has been shown that binary reactions with heavy ions offer a possibility for γ-ray studies of low- and intermediate-spin states in neutron-rich $Z = 50$ nuclei near the β-stability line. The ^{84}Kr + ^{116}Cd heavy ion collisions were used to study the ^{114}Cd and ^{116}Cd nuclei. The experiment was performed by using the K130 cyclotron at JYFL and the TESSA3 Ge-detector array, comprising 12 Compton suppressed Ge detectors and a multiplicity filter consisting of 50 BGO elements. Yrast levels up to (12^+) and (10^+) states have been observed in ^{114}Cd and ^{116}Cd, respectively. Four lowest members of the intruder bands based on the 0_2^+ state in ^{114}Cd and on the second excited 0_3^+ state in ^{116}Cd have been identified confirming the energy behaviour of the intruder states proposed in Ref. [Ku92]. These new data essentially add to the unique systematics of low-lying collective states in even-even Cd isotopes confirming the distinct behaviour of the intruder states.

Weak fusion-evaporation channels have been utilized to study the ^{115}Sn and the ^{116}Sn nuclei lying in the middle of the valley of stability. A compact DORIS array consisting of 12 Ge detectors was constructed for the γ-ray detection. For the selection of weak α-particle channels a PIN-diode charged-particle detector array was constructed. The $\gamma\gamma$-coincidence data with a proper gate on the PIN diode alpha spectrum resulted in very clean γ-ray spectra for the ^{115}Sn and the ^{116}Sn nuclei. In both of these nuclei, level schemes involving irregular sequences of spherical states, as well as rotational bands, were constructed up to spin I =20. The spherical states are interpreted to arise from pure neutron configurations, while the deformed, intruder bands obviously involve proton 2p-2h excitations across the Z = 50 shell gap. In the deformed band in ^{116}Sn an increase in the alignment takes place at $\hbar\omega = 0.46$ MeV. In ^{115}Sn the four observed rotational bands can be explained by coupling an odd neutron to the intruder structure in the neighbouring even-mass Sn nucleus. Many of the spherical states can be explained by the coupling of the valence neutrons to the low-lying yrast states in ^{114}Sn or ^{116}Sn. The MQPM calculations performed for ^{115}Sn are able to reproduce spherical yrast states up to I = 27/2 for both parities.

References

[Ap85] A. Aprahamian, Ph.D. thesis, Clark University, 1985

[Bac81] A. Bäcklin, N.G. Jonsson, R. Julin, J. Kantele, M. Luontama, A. Passoja and T. Poikolainen, Nucl. Phys. **A351** (1981) 490.

[Bl94] J. Blachot and G. Marguier, Nucl. Data Sheets 73 (1994) 81.

[Bl95] J. Blachot and G. Marguier, Nucl. Data Sheets 75 (1995) 739.

[Br79] J. Bron, W.H.A. Hesselink, A. van Poelgeest, J.J.A. Zalmstra, M.J. Uitzinger, H. Verheul, K. Heyde, M. Waroquier, H. Vincx and P. van Isacker, Nucl. Phys. **A318** (1979) 335.

[Br90] R. Broda, M.A. Quader, P.J. Daly, R.V.F. Janssens, T.L. Khoo, W.C. Ma and M.W. Drigert, Phys. Lett. **B251** (1990) 245.

[Ca92] R. F. Casten, J. Jolie, H.G. Borner, D.S. Brenner, N.V. Zamfir, W-T. Chou, and A. Aprahamian, Phys. Lett. **B297** (1992) 19.

[Co74] J. Conrad, R. Repnow, E. Grosse, H. Homeyer, E. Jaeschke and J.P. Wurm, Nucl. Phys. **A234** (1974) 157.

[Co97] J.F. Cocks, P.A. Butler, K.J. Cann, P.T. Greenlees, G.T. Jones, S. Asztalos, P. Bhattacharyya, R. Broda, R.M. Clark, M.A. Deleplanque, R.M. Diamond, P. Fallon, B. Fornal, P.M. Jones, R. Julin, T. Lauritsen, I.Y. Lee, A.O. Macchiavelli, R.W. MacLeod, J.F. Smith, F.S. Stephens and C.T. Zhang, Phys. Rev. Letters **78** (1997) 2920.

[De93] M. Deleze, S. Drissi, J. Jolie, J. Kern and J.P. Vorlet, Nucl. Phys. **A554** (1993) 1.

[Du89] J. L. Durell, Proc. Int. Conf. on the Spectroscopy of Heavy Nuclei, Crete, 1989, p. 304 (1990)

[Fa88] C. Fahlander, A. Backlin, L. Hasselgren, A. Kavka, V. Mittal, L.E. Svensson, B. Varnestig, D. Cline, B. Kotlinski, H. Grein, E. Grosse, R. Kulessa, C. Michel, W. Spreng, H.J. Wollersheim and J. Stachel, Nucl. Phys. **A485** (1988) 327.

[Fi77] H.W. Fielding, R.E. Anderson, C.D. Zafiratos, D.A. Lind, F.E. Cecil, H.H. Wieman and W.P. Alford, Nucl. Phys. **A281** (1977) 389.

[Ga95] G. Gangopadhyay, A.K. Singh, D. Banerjee, R. Bhattacharya, R.K. Bhowmik, S. Muralithar, G. Rodrigues, R.P. Singh, A. Goswami, S. Bhattacharya, B. Dasmahapatra, S. Sen, Z. Phys. **A351** (1995) 1.

[Gu76] W.F. van Gunsteren and K. Allaart, Z. Phys. **A276** (1976) 1.

[Gu78] W.F. van Gunsteren, K. Allaart and P. Hofstra, Z. Phys. **A288** (1978) 49.

[Ha88] H. Harada, T. Murakami, K. Yoshida, J. Kasagi, T. Inamura and T. Kubo, Phys. Lett. **B207** (1988) 17.

[Ha89] H. Harada, M. Sugawara, H. Kusakari, H. Shinohara, Y. Ono, K. Furuno, T. Hosoda, M. Adachi, S. Matsuki and K. Kawamura, Phys. Rev. **C39** (1989) 132.

[Has79] O. Hashimoto, Y. Shita, G. Ch. Madueme, N. Yoshikawa, M. Sakai and S. Ohya, Nucl. Phys. **A318** (1979) 145.

[He87] K. Heyde, J. Jolie, J. Moreau, J. Ryckebusch, M. Waroquier, P. van Duppen, M. Huyse and J.L. Wood, Nucl. Phys. **A466** (1987) 189.

[He92] K. Heyde, C. De Koster, J. Jolie and J.L. Wood, Phys. Rev. **C46** (1992) 541.

[He95] K. Heyde, J. Jolie, H. Lehmann, C. De Coster and J.L. Wood, Nucl. Phys. **A586** (1995) 1.

[Hel96] K. Helariutta, T. Enqvist, P.M. Jones, R. Julin , S. Juutinen, P. Jämsen, H. Kankaanpää, P. Kuusiniemi, M. Leino, M. Muikku, M. Piiparinen, A. Savelius, W.H. Trzaska, S. Törmänen, J. Uusitalo, R.G. Allat, P.A. Butler, P.T. Greenlees, and R.D. Page, Phys. Rev. **C54** (1996) 6.

[In92] A. Insolia, N. Sandulescu, J. Blomqvist and R.J. Liotta, Nucl. Phys. **A550** (1992) 34.

[Ja89] V.P. Janzen, M.P. Carpenter, L.L. Riedinger, W. Schmitz, D.G. Popescu, J.A. Cameron, J.K. Johansson, D.D. Rajnauth, J.C. Waddington, G. Kajrys, S. Monaro and S. Pilotte, Phys. Rev. **C39** (1989) 2050.

[Ju94] S. Juutinen, R. Julin, M. Piiparinen, P. Ahonen, B. Cederwall, C. Fahlander, A. Lampinen, T. Lonnroth, A. Maj, S. Mitarai, D. Muller, J. Nyberg, P. Simecek, M. Sugawara, I. Thorslund, S. Tormanen, A. Virtanen, R. Wyss, Nucl. Phys. **A573** (1994) 306.

[Ju96] S. Juutinen, R. Julin, P. Jones, A. Lampinen, G. Lhersonneau, E. Mäkelä, M. Piiparinen, A. Savelius and S. Törmänen, Physics Letters **B386** (1996) 80.

[Ju98] S. Juutinen, A. Savelius, K. Helariutta, P. Jones, R. Julin, P. Jämsen, H. Kankaanpää, M. Muikku, M. Piiparinen, S. Törmänen and P.T. Greenlees, to be published.

[Jul94] R. Julin, Phys. Scripta **T56** (1995) 151.

[Ka79] J. Kantele, R. Julin, M. Luontama, A. Passoja, T. Poikolainen, A. Bäcklin and N.-G. Johnsson, Z. Phys. **A289** (1979) 157.

[Kai72] D.K. Kaipov, Y.G. Kosyak, L.N. Smirin, Y.K. Shubnyi, Izv. Akad. Nauk KazSSR, Ser. Fiz.-Mat. No. 2 (1972) 64.

[Ke90] J. Kern, A. Bruder, S. Drissi, V.A. Ionescu, D. Kusnezov, Nucl. Phys. **A512** (1990) 1.

[Ku90] J. Kumpulainen, Ph.D. thesis, University of Jyväskylä, 1990

[Ku92] J. Kumpulainen, R. Julin, J. Kantele, A. Passoja, W.H. Trzaska, E. Verho, J. Vaaramaki, D. Cutoiu and M. Ivascu, Phys. Rev. **C45** (1992) 640.

[Kur92] T. Kuroyanagi, S. Mitarai, S. Suematsu, B.J. Min, H. Tomura, J. Mukai, T. Maeda, R. Nakatani, G. Sletten, J. Nyberg, D. Jerrestam, Nucl. Instr. and Meth. **A316** (1992) 289.

[Kus87] D. Kusnezov, A. Bruder, V. Ionescu, J. Kern, M. Rast, K. Heyde, P.Van Isacker, J. Moreau, M. Waroquier and R.A. Meyer Helv. Phys. Acta **60** (1987) 456.

[LaF95] D.R. LaFosse, D.B. Fossan, J.R. Hughes, Y. Liang, P. Vaska, M. Waring, J.-y. Zhang, R.M. Clark, R. Wadsworth, S.A. Forbes and E.S. Paul, Phys. Rev. **C51** (1995) R2876.

[LaF97] D.R. LaFosse, D.B. Fossan, J.R. Hughes, Y. Liang, H. Schnare, P. Vaska, M.P. Waring and J.-y. Zhang, Phys. Rev. **C56** (1997) 760.

[Le95] M. Leino et. al., Nucl. Instr. and Meth. **B99** (1995) 653.

[Lob97] Yu.N. Lobach, L. Käubler, R. Schwengner and A.A Pasternak, to be submitted to Z. Phys. A.

[Ma75] G. Ch. Madueme, L. Westerberg, L. O. Edvardson and M. Migahed, Phys. Scripta **12** (1975) 189.

[Ma89] H. Mach, M. Moszynski, R.F. Casten, R.L. Gill, D.S. Brenner, J.A. Winger, W. Krips, C. Wesselborg, M. Buscher, F.K. Wohn, A. Aprahamian, D. Alburger, A. Gelberg and A. Piotrowski, Phys. Rev. Lett. **63** (1989) 143.

[Ma94] R.H. Mayer, D.T. Nisius, I.G. Bearden, P. Bhattacharyya, L. Richter, M. Sterrazza, Z.W. Grabowski, P.J. Daly, R. Broda, B. Fornal, I. Ahmad, M.P. Carpenter, R.G. Henry, R.V.F. Janssens, T.L. Khoo, T. Lauritsen, Y. Liang and J. Blomqvist, Phys. Lett. **B336** (1994) 308.

[Mh84] A. Mheemeed, K. Schreckenbach, G. Barreau, H.R. Faust, H.G. Borner, R.Brissot, P. Hungerford, H.H. Schmidt, H.J. Scheerer, T. Von Egidy, K. Heyde, J.L. Wood, P. Van Isacker, M. Waroquier, G. Wenes, M.L. Stelts, Nucl. Phys. **A412** (1984) 113.

[No85] P.J Nolan and D.W. Gifford, Nucl. Instr. and Meth. **A236** (1985) 95.

[No86] P.J Nolan, Proc. Int. Nuclear Physics Conf., Harrogate (IOP Publ., Bristol, 1986) Inst. Phys. Conf. Ser. no. 86, p. 155

[Pa95] E.S. Paul, P.J. Woods, T. Davinson, R.D. Page, P.J. Sellin, C.W. Beausang, R.M. Clark, R.A. Cunningham, S.A. Forbes, D.B. Fossan, A. Gizon, J. Gizon, K. Hauschild, I.M. Hibbert, A.N. James, D.R. LaFosse, I. Lazarus, H. Schnare, J. Simpson, R. Wadsworth and M.P. Waring, Phys. Rev. **C51** (1995) 78.

[Po80] A. van Poelgeest, J. Bron, W.H.A. Hesselink, K. Allaart, J.J.A. Zalmstra, M.J. Uitzinger and H. Verheul, Nucl. Phys. **A346** (1980) 70.

[Pü77] F. Pühlhofer, Nucl. Phys. **A280** (1977)267.

[Ra95] D. C. Radford, Nucl. Instr. and Meth. **A361** (1995)297 and 306

[Re95] P. H. Regan, A.E. Stuchbery, G.D. Dracoulis, A.P. Byrne, G.J. Lane, T. Kibedi, D.C. Radford, A. Galindo-Uribarri, V.P. Janzen, D. Ward, S.M. Mullins, G. Hackman, J.H. DeGraaf, M. Cromaz and S. Pilotte, Nucl. Phys. **A586** (1995) 351.

[Reg95] P. H. Regan, A. E. Stuchbery and S. S. Andessen, Nucl. Phys. **A591** (1995) 533.

[Sa95] N. Sandulescu, J. Blomqvist and R.J. Liotta, Nucl. Phys. **A582** (1995) 257.

[Sa96] D.G. Sarantites, P.-F. Hua, M. Devlin. L.G. Sobotka, J. Elson, J.T. Hood, D.R. LaFosse, J.E. Sarantites and M.R. Maier, Nucl. Instr. and Meth. **A381** (1996) 418.

[Sch91] M. Schimmer, R. Wirowski, S. Albers, G. Böhm, A. Dewald, A. Gelberg and P. von Brentano, Z. Phys. **A338** (1991) 117.

[Sch92] M. Schimmer, S. Albers, A. Dewald, A Gelberg, R. Wirowski and P. von Brentano, Nucl. Phys. **A539** (1992) 527.

[Se97] J.M. Sears, D.B. Fossan, S.E. Gundel, I. Thorslund and K. Starosta, Phys. Rev. **C55** (1997) 1096.

[Sh79] R. E. Shroy, A.K. Gaigalas, G. Schatz, D.B. Fossan, Phys. Rev. **C19** (1979) 1324.

[Suh88] J. Suhonen, T. Taigel and A. Faessler, Nucl. Phys. **A486** (1988) 91.

[Suh98] J. Suhonen, J. Toivanen, A. Holt, T. Engeland, E. Osnes and M. Hjorth-Jensen, Nucl. Phys. **A628** (1998) 41.

[Th93] I. Thorslund, C. Fahlander, J. Nyberg, S. Juutinen, R. Julin, M. Piiparinen, R. Wyss, A. Lampinen, T. Lönnroth, D. Muller, S. Törmanen and A. Virtanen, Nucl. Phys **A564** (1993) 285.

[ToI] Table of Isotopes, 8th edition, ed. R.B Firestone, V.S. Shirley, C.M. Baglin, S.Y.F. Chu and J. Zipkin (Wiley, New York, 1996).

[Toi95] J. Toivanen and J. Suhonen, J. Phys. G21 (1995) 1491; Phys. Rev. **C57** (1998) 1237.

[Tor94] S. Törmänen, S. Juutinen, R. Julin, B. Cederwall, A. Johnson, R. Wyss, P. Ahonen, B. Fant, M. Matsuzaki, J. Nyberg, M. Piiparinen, S. Mitarai, J. Mukai and A. Virtanen, Nucl. Phys. **A572** (1994) 417.

[Tor97] S. Törmänen, S. Juutinen, R. Julin, A. Lampinen, E. Mäkelä, M.J. Piiparinen, A. Savelius, A. Virtanen, Ch. Droste, W. Karczmarczyk, T. Morek, J. Srebrny, K. Starosta and G.B. Hagemann, Nucl. Phys. **A613** (1997) 282.

[Tw86] P.J. Twin, B.M. Nyako, A.H. Nelson, J. Simpson, M.A. Bentley, H.W. Cranmer-Gordon, P.D Forsyth, D. Howe, A.R. Mokhtar, J.D. Morrison, J.F. Sharpey-Schafer, G. Sletten, Phys. Rev. Lett. **57** (1986) 811.

[Vi87] D.A. Viggars, H.W. Taylor, B. Singh and J.C. Waddington, Phys. Rev. **C36** (1987) 1006.

[Vi91] I.N. Vishnevski, G.B. Grygin, Yu.N. Lobach, V.E. Mitroshin, A.A. Pasternak and V.V. Trishin, Ukr. Phys. Journ. **36** (1991) 1132.

[Vis91] I. N. Vishnevskii, Yu. N. Lobach and V. V. Trishin, Izv. Akad. Nauk SSSR. Ser. Fiz. **55** (1991) 2176.

[Wa93] R. Wadsworth, H.R. Andrews, R.M. Clark, D.B. Fossan, A. Galindo-Uribarri, J.R. Hughes, V.P. Janzen, D.R. LaFosse, S.M. Mullins, E.S. Paul, D.C. Radford, H. Schnare, P. Vaska, D. Ward, J.N. Wilson and R. Wyss, Nucl. Phys. **A559** (1993) 461.

[Wa94] R. Wadsworth, H.R. Andrews, C.W. Beausang, R.M. Clark, J. DeGraaf, D.B. Fossan, A. Galindo--Uribarri, I.M. Hibbert, K. Hauschild, J.R. Hughes, V.P. Janzen, D.R. LaFosse, S.M. Mullins, E.S. Paul, L. Persson, S. Pilotte, D.C. Radford, H. Schnare, P. Vaska, D. Ward, J.N. Wilson and I. Ragnarsson, Phys. Rev. **C50** (1994) 483.

[We86] S.Y. van der Werf, N. Blasi, M.N. Harakeh, G. Wenes, A.D. Bacher, G.T. Emery, C.W. Glover, W.P. Jones, H.J. Karwowski, H.Nann, C.Olmer, P. den Heijer, C.W. de Jager, H. de Vries, J. Ryckebusch, M. Waroquier, Phys. Lett. **166B** (1986) 372.

[Za95] N. V. Zamfir, R.L. Gill, D.S. Brenner, R.F. Casten and A. Wolf, Phys. Rev. **C51** (1995) 98.